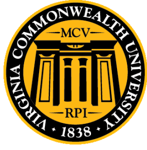

Virginia Commonwealth University
VCU Scholars Compass

Theses and Dissertations | Graduate School

2022

Low Loss Plasmon-Assisted Integrated Photonics

Dhruv Fomra
Virginia Commonwealth University

Follow this and additional works at: https://scholarscompass.vcu.edu/etd

Part of the Nanotechnology Fabrication Commons

© The Author

Downloaded from

https://scholarscompass.vcu.edu/etd/7181

This Dissertation is brought to you for free and open access by the Graduate School at VCU Scholars Compass. It has been accepted for inclusion in Theses and Dissertations by an authorized administrator of VCU Scholars Compass. For more information, please contact libcompass@vcu.edu.

Low Loss Plasmon-Assisted Integrated Photonics

A Dissertation submitted in partial fulfillment of the requirements for the degree of Doctor of Philosophy at Virginia Commonwealth University

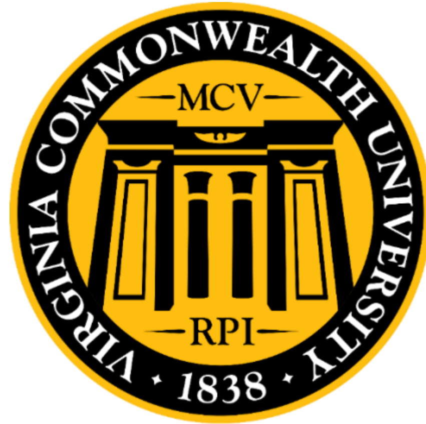

By

Dhruv Fomra

SRM University, B.Tech. 2017

Virginia Commonwealth University, 2017 - Present

Director: Dr. Nathaniel Kinsey, Associate Professor, Electrical and Computer Engineering

Richmond, Virginia

August, 2021

ACKNOWLEDGMENTS

I would like to express my heartfelt gratitude to my family, friends, and advisors for their support and guidance during my PhD studies. To my parents, sister, uncle, aunt and grandmom, thank you for your unwavering love and encouragement. Your sacrifices have not gone unnoticed and have been a driving force behind my success. To my friends, thank you for being a constant source of support and for providing a listening ear during the challenging times. Your presence in my life has made all the difference. To my advisors, at VCU (Dr. Kinsey, Dr. Avrutin, Dr. Özgür) and at NIST (Dr. Lezec, Dr. Agrawal), thank you for your expertise, guidance, and patience. Your valuable insights have been instrumental in shaping my research and have helped me grow not only as a researcher, but also as an individual. I would also like to thank my teammates for their willingness to brainstorm new ideas and for their constructive criticism. Your positive attitude and collaborative spirit have been a driving force behind our success. Your feedback has helped me grow and has pushed me to strive for excellence. I am grateful to have had the opportunity to work with such a talented and dedicated team. Thank you for everything. I would also like to extend a special thank you to my fiancé, Nirat, for all the love and support, especially through 2022, which has been nothing short of challenging. Your belief in me has kept me going even when I felt like giving up. And last, but not the least, to the funding agencies:

- Air Force Office of Scientific Research (FA9550-1-18-0151); Defense Advanced Research
- Virginia CCI
- National Science Foundation (#1808928)
- Virginia Microelectronics Consortium

TABLE OF CONTENTS

ABSTRACT 13
1. Introduction 16
2. Background 24
2.1. Lorentz Oscillator Model 24
2.2. Drude Model 27
2.3. Characterization of Thin Films of Metal 29
2.4. Plasmonics 33
2.5. Epsilon Near Zero Media 37
2.6. Prior Works and Challenges 41
2.7. Performance Metrics 43
3. Nanophotonic Devices 45
3.1. Plasmon-Assisted Design Approach 45
3.2. All-Oxide Plasmon Assisted EO Modulator (Tier 2 Speed) 49
3.3. Polymer based EO Modulator (Tier 2 Speed) 57
3.4. NOEM Dynamic Polarization Rotator (Tier 1 Speed) 59
3.5. NOEM Dynamic Switch (Tier 1 Speed) 64
3.6. Conclusion 68
4. Device fabrication of all-oxide modulator 71
4.1. All Oxide EO Modulator – Material Deposition 71
4.1.1. Aluminum Zinc Oxide 71
4.1.2. Near IR Losses in Aluminum Zinc Oxide 83
4.1.3. Indium Tin Oxide 86
4.2. Vertical slot design 89
4.3. All Oxide EO Modulator – Device Fabrication 95
4.4. Other Devices – Proposed Fabrication Routes 97
4.5. Characterization 99
5. Conclusion and Future Work 102
5.1. Future Work 106
REFERENCES 108

6. Publications 122
6.1. Journal 122
6.2. Patents and Book Chapters 123
6.3. Major Conference Submissions 123
6.4. Vita 125

LIST OF TABLES

Table 1: Summary table of the performance metrics of the 4 devices simulated in this thesis. . 103

LIST OF FIGURES

Figure 1: The number of synapses found in various species and compared to the state-of-the-art neural networks. The Gshard MoE already has any many synapses as a mouse [5]. 18

Figure 2: Schematic of the two parts of a network packet. Tier 1 devices operate only on the header, whereas Tier 2 devices operate on every byte of the payload. 20

Figure 3: (a) Examples of a fiber coupled optical switch from ThorLabs, (b) Example of a fiber coupled EO modulator from Aerodiode. Each of these devices about ~5 cm in length. 21

Figure 4: A rendering of a photonic integrated circuit. This semiconductor chip has both electrical and optical elements on it. As an example, electrical signals are encoded onto the optical input with the help of routers, switches, modulators, and polarization controllers. 23

Figure 5: Frequency depende~~n~~ce of the real and imaginary parts of the complex dielectric constant (ε_1 and ε_2 respectively, left panel) and of the refractive index of a typical dipole oscillator material (n and κ respectively, right panel), at frequencies ω close to a resonance ω_0 [8]. 27

Figure 6: Wavelength dependence of the real (left) and imaginary (right) parts the of complex relative permittivity of a typical material of dielectric response given by the Drude model, with free carrier density N (legend insets) as a parameter. The crossover point shifts to shorter wavelengths as N increases. Blue shaded area denotes the epsilon-near-zero region. [Graphs plotted using the Drude model in Matlab.] 28

Figure 7: Schematic of spectroscopic ellipsometry. Here, a light source with wavelength λ is configured to produce an arbitrary polarization state (E_i) by a variable polarizer. The incident beam is then used to interrogate the sample at an angle θ. The polarization state of the reflected, beam (E_o) is altered by the interaction with the sample. After passing through an analyzer which allows the polarization state of the reflected beam to be measured at two perpendicular states, the complex s and p reflection coefficients of the sample can be determined [9]. 30

Figure 8: Comparison of data balance for a) transparent film, b) semi-absorbing film, and c) thin absorbing film. For transparent and semi-absorbing films, the ellipsometry measurement are sufficient to allow for unique retrieval of the refractive index and thickness. However, for absorbing films, the ellipsometry measurements alone are insufficient to allow for a unique retrieval of the optical properties and thickness, and additional information should be added to improve the confidence of the result [9]. 32

Figure 9: a) Geometry of a dielectric and metallic slab to sustain SPP propagation along the interface; b) Frequency vs. wavevector ~~E-K~~ diagram of the SPP mode and the metal dielectric interface when the dielectric is air and silica, respectively [17]. 36

Figure 10: Vertical (y) component of the electric field for a mode propagating in a silicon waveguide on glass a) cladded by air, b) cladded with air and a thin layer of ENZ material. The thin ENZ layer results in a strong confinement of the electric field. 38

Figure 11: Complex permittivity (left) and complex refractive index (right) components given by a typical Drude model [34]. 39

Figure 12: a) Ultra-fast (few ps) response time of an AZO film under optical tuning [42]; b) Change in local permittivity of an AZO film under electrical biasing where the AZO forms the anode of a capacitor structure of AZO/ HfO_2/ Si. x axis denotes the position in the AZO film normal to the planar interface with HfO_2 (located at x=15 nm [Calculated using COMSOL Multiphysics and Matlab] 40

Figure 13: a) and b) are examples of a plasmonic metasurface design which although offer large changes in index, suffer from broad resonances [42]. 42

Figure 14: Plot of compute/area vs insertion loss for several photonic and plasmonic devices in literature. In the quest to increase the available compute/ area, these devices have simultaneously led to an increase in insertion loss. The goal is to achieve a vertical not diagonal transition. The gap which we want to fill is represented by the grey shaded region. 46

Figure 15: Schematic of the plasmon-assisted design principle. Using a "knob", the input signal is routed to either the lossy plasmonic section, or the low-loss photonic section, dependent on the desired on or off state of the device. 47

Figure 16: Comparison of plots of insertion loss vs. active plasmonic loss for the all-plasmonic Mach-Zehnder interferometer modulator of ref. [57] and the plasmon-assisted ring resonator modulator of ref. [30], respectively. Losses in the plasmon assisted design can be reduced by more than 6 dB, primarily due to the loss bypassing mechanism in the passive state. 49

Figure 17: Examples of EO modulators in literature fabricated using ENZ materials. Notice the metal layer in the active region in both these devices. The metallic layer excited a hybrid mode which causes an increase in IL due to ohmic losses [37,58]. 50

Figure 18: (a) A schematic of the slot waveguide electro-optic modulator. The inset shows the zoomed in version of the active region, (b) Example of plasmon-assisted design approach, (c) Representative image of devices explored in literature. 51

Figure 19: Schematic of the proposed slot waveguide configuration, illustrating how the effective index of the two silicon waveguides combined with an TCO-filled slot in the middle is larger than that of the surrounding air. Subsequently, the E-field is localized in the low index oxide medium due to the continuity of the D-field. 52

Figure 20: (a-b) Electron and hole concentration within ITO and p-type Si as a function of gate voltage. The bulk hole carrier concentration within p-type Si is $1x10^{18}$ cm^{-3} (c-d) Real and imaginary part of permittivity within ITO as a function of gate voltage and position within the ITO layer. Simulations done using a COMSOL FEM solver. 53

Figure 21: (a) ER (dB/µm) (black) and IL for 6dB modulation (red) for a slot modulator. The slot width is 40 nm, (b) ER (dB/µm) and IL (dB/µm) for single slot configuration as a function of slot width. A smaller slot width is more favorable to obtaining a low IL and high ER. The rail width is fixed and equal to 200 nm 55

Figure 22: Schematic of the hybrid EO modulator design. The inset on the left shows the on- and off-states of the device. In the off state, the light bypasses the HPP ring due to destructive interference, while under a bias, the index of the EO polymer increases due to the Pockel's effect and the light couples into the plasmonic section where it is absorbed. b) Plot of the transmission

spectra in the off-state versus on-state (black curve) which illustrates the strong modulation depth and low insertion loss of the device 57

Figure 23: a) Propagation lengths of Al-Si hybrid waveguides with various low-index materials, b) Example of sacrificial under etch of TiN on Si using MgO in extremely dilute phosphoric acid 60

Figure 24: Effective mode index of TE, TM and Hybrid (HPP) mode of hybrid air-gap waveguide (gap size: 30 nm and 80 nm) plotted as a function of the width of the Si waveguide. 62

Figure 25: a) Schematic of the proposed dynamic polarization rotator, which includes a Si waveguide with a suspended Al cantilever and stopper layers to limit pull-in. b), c) and d) Normalized electric field mode profiles for a 30 nm and an 80 nm gap and various distances along the structure. When the gap is 30 nm, the mode adiabatically transfers from TE (horizontal) to a HPP (vertical) mode. In the case of an 80 nm gap, the two modes are sufficiently mis-matched to preclude efficient coupling within the device length 63

Figure 26: a) Schematic of the proposed hybrid "Plasmon-Assisted" dynamic NOEM switch, consisting of an Al ring suspended over a silicon ring, which is coupled to two bus waveguides. Inset on the left depicts the operation of the switch in the on- and off-state where switching is achieved through a shift in resonance induced by electro-static deflection of the Al ring. b) Transmission spectra at the through port, obtained from 3D simulations of a single bus waveguide coupled to a hybrid ring resonator with a 70, 60, 50 and 40 nm gap; a FWHM between 0.9 to 1.2 nm is obtained. With a 20 nm deflection, shown by the dashed lines in the figure, the resonance wavelength shifts by 13 times the FWHM, providing high contrast switching 66

Figure 27: Schematic of the pulse sequence in the modified ALD process. 'M' alternating pulses of H2O and Diethyl Zinc (DEZ) are followed by a doping cycle of H_2O, DEZ, and Trimethyl Aluminum (TMA). The frequency of the doping cycle determines the carrier concentration and 'N' number of super-cycles determine the thickness [68] 73

Figure 28: Schematic of modifications made to the doping the cycle, as the ALD process moves from the conventional to the modified regime. The dashed grey line in the pulse train schematic denotes the density of active surface sites. The conventional doping cycle includes H_2O and TMA pulses under surface saturation conditions leading to a very high Al incorporation. Step 1: introducing a DEZ pulse in between H_2O and TMA pulses leads to a mixture of Zn and Al radicals in the doping layer, thus reducing Al incorporation compared to the original doping cycle. Step 2: further reducing the TMA pulse duration limits the amount of TMA supplied, thus further reducing Al incorporation. Step 3: lastly, higher substrate temperature reduces the density of active sites (number of hydroxyl groups), thus reducing Al and Zn incorporation in each cycle. Ultimately, the reduction in the Al incorporation per cycle enables a more frequent occurrence of the doping cycle, thus producing more even and effective doping of the ZnO film [68] 74

Figure 29: (a) Plot of resistivity versus Al dosing percentage at different TMA pulse durations, of AZO deposited on a sapphire substrate at a substrate temperature of 250°C. With reduced pulse duration, the optimum dosing percentage shifts to higher values due to the reduced Al incorporation in each dosing cycle. (b) A plot of growth rate versus deposition temperature. The reduction in growth rate occurs because of the evaporation of the H2O at elevated temperatures that reduces the number of active sites available with which Zn or Al radicals may bond [68] .. 76

Figure 30: (a) Resistivity, (b) Carrier concentration and (c) Hall (solid squares) and Optical (Open Squares) mobility of ~ 45nm thick Al:ZnO films deposited on a sapphire substrate, at 20% Al dosing, as a function of deposition temperature. The drop in resistivity is largely attributed to the increase in the Hall mobility of these films, as the carrier concentration shows only a small change. (d) Optical mobility of Al:ZnO films deposited on silicon substrates under the same conditions [68] 79

Figure 31: (a) Carrier concentration and (b) Hall mobility as a function of Al dosing percentage for ~45 nm thick films deposited on a sapphire substrate at 350°C, (c) and (d) Color map of the real part of permittivity, for films grown on sapphire and silicon substrates, plotted versus wavelength and Al dosing which shows the static tunability of optical properties of ~45 nm films on sapphire and Si grown under the optimized conditions of TS =350°C, 7.5 ms TMA pulse duration (with orifice) and H2O/ DEZ/ TMA dosing sequence. The symbol and the solid connecting lines denote the ENZ wavelengths of these films. The two highlighted regions mark the O and C bands of telecommunication [68] 81

Figure 32: (a) real and imaginary part of permittivity for ~100nm thick films deposited on sapphire and silicon substrates at 350°C, with crossover wavelengths at 1330 and 1370 nm, respectively. (b) the imaginary permittivity of heavily doped (Al and Ga) ZnO films at the crossover wavelength. Moving to the modified ALD technique enhances doping efficiency thus enabling Al:ZnO films with reduced losses and crossover wavelengths as low as 1330 nm. This enables the use of these films in integrated photonic devices, as the near-zero index properties are now accessible across most of the technologically relevant bands. The blue arrow and the shaded region on the plot denote the range of losses (ε" < 2) in which ENZ films exhibit NZI effects, such as slow light and wavelength expansion [23], emphasizing the need for low loss ENZ films. The red circle (~100nm film on sapphire), the red square (~100nm film on silicon), and the red triangle (45 nm film on sapphire) represent the Al:ZnO films grown under the optimized conditions [68]. Optical properties are estimated from Hall effect data using the Drude model, using a hyperbolic effective mass dispersion for ZnO for references that only reported electrical properties [52,52,55-57]... 82

Figure 33: (a) Real and imaginary parts of permittivity for ~100nm thick films deposited on sapphire and silicon substrates at 350°C, with crossover wavelengths at 1330 and 1370 nm, respectively. 84

Figure 34: The imaginary permittivity, indicative of the loss in the films, is plotted as a function of wavelength (from 240 nm to 30,000 nm), for a set of AZO films deposited on silicon with ALD dosing percentage varying from 2% to 20%. Counter-intuitively, the loss in the lowest dosed films is higher than the loss in the higher dosed films. 85

Figure 35: The curve indicated by 1 is the Drude contribution, while the features indicted by 2 are the phononic contributions. The feature indicated by 3, can only be fit using Gaussian oscillators, which are usually indicative of absorption caused by either interband transitions, impurities or defects 86

Figure 36: Real part of permittivity of a 50 nm thick ITO film deposited on a fused silica substrate using the 4Wave cluster sputter deposition tool. 87

Figure 37: Imaginary part of permittivity of a 50 nm thick ITO film deposited on a fused silica substrate using the 4Wave cluster sputter deposition tool. 88

Figure 38: Electrical properties of a 50 nm thick ITO film deposited on a fused silica substrate using the 4Wave cluster sputter deposition tool and measured using the Hall Effect 88

Figure 39: Scanning electron micrograph of focused-ion-beam (FIB) cross-sectional image of sputter-deposition test structure. Structure consists of 125-nm-thick ITO (light gray) sputter-deposited onto a Si grating (dark grey) with line width = 300 nm, trench width = 50 to 1500 nm, and grating depth = 200 nm. The narrowest structures exhibit a non-conformal coating of ITO. The backfilled material in the slot and overcoated material above the grating is Pt (medium gray), which was deposited during the FIB process to assist with the cross-sectioning process. 89

Figure 40: Proposed vertical alternative to the horizontal slot design. The advantages of the vertical slot are multifold. i). Better control over critical slot dimensions, ii). Smooth interfaces at the slot, iii). Potential for depositing ITO and Al_2O_3 without breaking vacuum. 90

Figure 41: Simulated E-field profiles of the active region at 0V and 5V bias. Simulations performed using an FEM solver, COMSOL. At a bias of 0V, the incoming frequency experiences an all-dielectric structure. With the E-field polarized normal to the substrate, it is confined in the low index region (ITO and Oxide). On application of a 5V bias, a 1 nm region at the interface of ITO/ Oxide now exhibits a permittivity close to 0. The E-field now get confined into this narrow region, as shown in the inset, on right. The graph further demonstrates the drastically enhanced E-field. This thin region also exhibits higher losses due to increased electron-electron scattering, thus, in effect, attenuating the input signal drastically. 91

Figure 42: (a). Effective mode index of a vertical slot waveguide as a function of the thickness of the top a-Si and the width of the waveguide (WG). The black line highlights the ~1.77 index selected for device design, (b). The mode indices of a rib waveguide as a function of the width and their corresponding mode profiles 92

Figure 43: (a) Mode overlap percentage between the vertical slot waveguide and the various modes of the rib waveguide. (b) The insertion loss of the active area for a 9 dB modulation depth as a function of the thickness of the a-Si layer and the width of the waveguide 93

Figure 44: (a) Comparison of the loss of a sputtered ITO film measured using an ellipsometer (dashed line) and the modeled loss based on the values obtained from the Hall effect measurement (solid line). (b) The optical mobility needed to reach the loss measured using the ellipsometer. 94

Figure 45: Schematic of the fabrication process, with non-critical alignment steps 96

Figure 46: SEM images before and after planarization of the waveguides 96

Figure 47: False-color SEM image of the all-oxide EO modulator fabricated on a 4" Si wafer. This is an example of a possible fabrication route to realize the device on a SOI wafer 97

Figure 48: Schematic of the proposed devices, with a single critical alignment step of aligning the Al ring to the Silicon ring 99

Figure 49: Schematic of the experimental setup used to measure the DC, low frequency, and high frequency response of the devices. EDFA's and RF Amplifiers will be used as required to maintain sufficient signal to noise ratio. 100

Figure 50: Picture of the constructed test bench which will be used from passive, DC and high frequency measurements of the proposed devices 101

Figure 51: Plot of compute/area vs insertion loss for several photonic and plasmonic devices in literature. In the quest to increase the available compute/ area, these devices had led to an increase in insertion loss. However, the all-oxide modulator (red circle) and the hybrid polymer EO modulator (red star), with their innovative plasmon-assisted design principle, can introduce a vertical transition in the graph, (b) conceptual schematic of miniaturization of PIC circuits. ... 104

Figure 52: A rendering of a plasmonic PIC. The size disparity between the electrical and optical components have been reduced. Furthermore, by using plasmon-assisted design principles, these devices have overcome the loss limitation, traditionally associated with plasmonic devices. Circuits such as these have important implications for the aerospace and telecommunication, industry as discussed in the introduction. 105

ABSTRACT

The field of photonics has seen rapid advancements in recent years, leading to the development of innovative optical technologies that have greatly improved our daily lives. For instance, the use of optical fibers has revolutionized long-distance communication, allowing for the transmission of vast amounts of data at high speeds. In the medical field, optical imaging techniques have enabled doctors to non-invasively diagnose and treat a wide range of diseases. Photonic integrated circuits (PICs), semiconductor chips with both photonic and electronic elements, have the potential to take these advancements even further. By integrating high-speed optical devices onto a compact chip, PICs can bridge the size disparity between electronics and photonics, paving the way for the development of ultra-fast, low-power optical communication and computing systems. Beyond telecommunication, PICs have a wide range of applications, including autonomous driving, healthcare, optical sensing, quantum computers and networks.

However, realization and wide adoption of PICs across the various fields faces a key challenge. Traditional photonic active devices utilize dielectric (e.g. glass) or semiconducting materials (e.g. silicon) and are typically quite large, on the scale of 100's of um, while electronic devices are several orders of magnitude smaller (0.01 um). This has led to integration challenges when combining electronics and photonics on a single platform.

Plasmonics, a technology which confines light to the interface of metals and dielectrics, has a potential to address challenges. In particular, it has been shown to led to smaller devices (~10 um or less), enabling higher density optical circuits and devices on-chip. However, the technology is limited by quite extraordinarily high off-state transmission, wherein ~10% of an input signal makes it out of the device. This is simply too high to be practical and has restricted plasmonic technologies from impacting PIC technology.

This thesis seeks to address this size disparity, while maintaining high speeds (100's of GHz), low losses (< 1dB) and high energy efficiency (~ 100 fJ/bit), through the concept of plasmon-assisted devices.

The plasmon-assisted design philosophy is based on engaging and disengaging the lossy plasmonic component based on when active modulation is needed. This can be thought of as turning a "knob" to route light into the lossy plasmonic element, when low transmission is desired or route light into a dielectric element, when high transmission is needed. In the work presented here, we illustrate two methods to achieve this functionality, 1) by utilizing unique materials with epsilon-near-zero properties that can be switched been low loss-dielectric state, or a high loss metallic state, 2) by utilizing resonant structures such as ring resonators that use the interference of light waves to change the pathway light takes, either through a low-loss waveguide or a lossy plasmonic ring.,.

Using the plasmon-assisted design philosophy, I explore 4 integrated photonic devices: an all-oxide modulator, a hybrid polymer-based modulator, a nano-opto-electro-mechanical (NOEM) based dynamic polarization rotator, and a NOEM based router. Furthermore, the all-oxide modulator, due to its ready availability of materials and broadband nature, is fabricated as a proof-of-concept fabrication sequence.

As will be shown, the use of the plasmon-assisted approach generates proposed devices that have the potential to exhibit record performance**, significantly elevating the capabilities of integrated photonic devices while greatly reducing the size disparity**. For example, the all-oxide modulator can exhibit resistive-capacitive (RC) limited speeds of up to 333 GHz with a sub 0.2 dB insertion loss (IL), while the hybrid polymer-based modulator can exhibit RC limited speeds of 700 GHz but with narrow linewidth. The NOEM based devices can operate with record low energy

consumption, down to a few 100 aJ/bit. In addition, this record-breaking performance can be achieved with device that are less than 40 um^2 in size.

Together, these devices achieve leading performance in a small platform, while critically addressing the loss issue that has so far plagued plasmonic technologies. Moreover, by realizing not just one, but a suite of key devices that are compact, high performing and low loss, this work enables the realization of a fully functional device platform that can be employed in future PICs and facilitate rapid advancements in telecommunications.

1. INTRODUCTION

Over the past several decades, the world has steadily undergone a digital transformation, a trend that is only set to accelerate over the next few decades. This transformation has been fueled in large part through the development of the internet. Today the internet is central to the functioning of key sectors affecting our lives such as financial markets, healthcare systems, telecommunications infrastructure supporting the work-from-home trends, entertainment, and much more [1]. Yet, this success is not without its challenges. In just two years, it is predicted that more than 4.8 zettabytes will pass through global networks every year, a value that is more than the entire sum of information transmitted between 1984 and 2016. This exponential growth is bolstered by the continued penetration of internet connectivity across the globe as well as by several technologies becoming standard, including 5G wireless networks (more than 10× current speeds), ultrafast WiFi-6 networks and hotspots (10 Gbps), artificial intelligence development within the technology sector, ultra-high-definition, and ultra-dense internet of things with applications ranging from smart health to smart cities [2]. Moreover, the type of traffic is changing, where by 2022 it is predicted that nearly half of all the connections will be between machines, and enormous amounts of data, upwards several petabytes, will routinely flow within a given data center to support artificial intelligence [3,4].

Integrated photonics, a rapidly emerging field in photonics, is playing a crucial role in supporting this exponential growth of the internet and other related applications such as sensing, communication and more recently, computing. One of the most widely used components of an integrated photonics circuit is an optical interconnect. These devices facilitate conversion between

electrical and optical signals and are commonly used in data centers. However more recently, optical interconnects have found use in high performance semiconductor chips that support artificial intelligence (AI) and machine learning (ML) applications [5]. This field has seen extraordinary momentum over the last decade, so much so that OpenAI, an AI research and deployment company, noted that since 2012, "the amount of compute used in the largest AI training runs has been doubling every 3.4 months" [5]. This staggering growth has been sustained by continuous development of large neural networks, with over a trillion nodes, that improve both accuracy and generality, from companies such as Nvidia, Microsoft and Google. Up until 2019, the biggest model was the Transformer with 465 million parameters, equivalent to the number of synapses of an insect less intelligent than a honeybee (Fig. 1). By mid-2020, the Gshard MoE was the largest natural language processing (NLP) model with over a trillion parameters, equivalent to the number of synapses of a mouse. From this point, the jump to human-level translation capabilities are just a few orders of magnitude and potentially a few years away. However, the path to human-level AI and beyond, is not clear. All that is known is that the jump requires an increase of at least 3 orders of magnitude in the number of model parameters, along with a corresponding increase in computational throughput (by adding nodes and increasing speed of each node) [5]. This is challenging to achieve using existing technologies, as they rely on copper cables, which serve as interconnects on a chip. However, data transfer rates using copper cables is usually limited to about 300 Mbps, and this limitation is often referred to as the copper bandwidth bottleneck. The limitation in speed stems from the fact that these cables need to be charged and discharged to transmit data. Moreover, closely spaced cables also lead to parasitic capacitances,

which further limits the speed (RC). On the other hand, optical pulses through waveguides can theoretically support THz bandwidth.

Thus, to support an increase in number of model parameters and nodes, potentially up to a 1000x increase, the copper bandwidth bottleneck needs to be overcome, which is where optical interconnects are set to play an integral role.

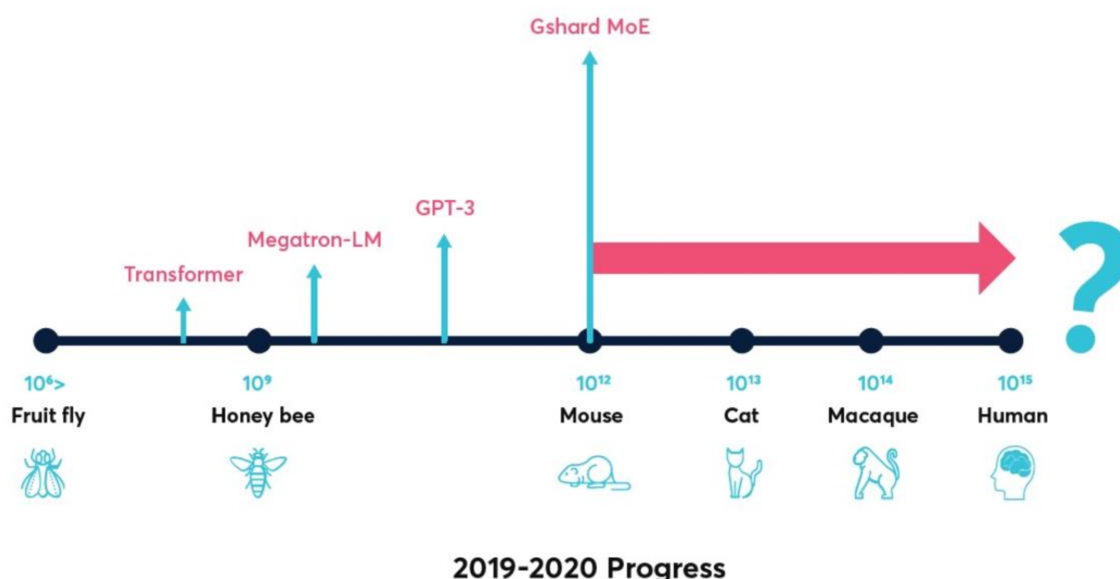

Figure 1: The number of synapses found in various species and compared to the state-of-the-art neural networks. The Gshard MoE already has any many synapses as a mouse [5].

The movement towards optical interconnects to overcome this limitation is already underway [5–7], and is becoming a new standard in the construction of large-scale networks. While successful, the use of optical data transmission necessitates the conversion of electrical data in traditional electronics (e.g., computers, sensors) into optical signals. The device which performs this operation is called an Electro-optic (EO) modulator, which accepts electrical signals as an input (i.e., data from a computer) to alter the properties of a light (e.g. amplitude or phase).

Beyond the key role EO modulators play in data centers they are also essential in areas such as aerospace and defense. These include the rapidly rising bandwidth demands, while maintaining size, weight and power compatibility and avoiding electromagnetic interference**[s]** as aircraft~~s~~, spaceships and other vehicles become increasingly complex with several electronic sensors, actuators and computer systems are added for increased autonomy. EO modulators further enable greater design freedom, as they can allow systems to be logically connected, but physically distributed. For example, a beam former is controlled by sensors and processors, which are functionally and logically connected, however need not be physically co-located. To enable greater design freedom, EO modulators can enable these to be physically decoupled, such that sensors and processors can fit within different size, power, and weight constraints [6]. Lastly, the mechanical and thermal robustness of I/O interconnects, which most industry-leading designs lack, is quintessential for defense applications. To support these trends and mission critical applications, EO modulators need to witness rapid improvement from the current industry-leading designs.

> ***To illustrate the importance of advances in this sector, I note that the market for EO modulators, even excluding semiconductor chips for AI and ML applications, is expected to balloon into a $44 Billion industry, at representing a compound annual growth rate of 7% from now through 2026 [8].***

While EO modulators are perhaps the most critical component in the translation of electrical signals into optical signals, they are but one component required to effectively transfer information across a network reliably. In particular, additional devices are required including signal routers (which sort and direct traffic on a network to its desired location), multiplexers (which enable multiple data streams to be sent in parallel), polarization controllers (which facilitate the ability to

interact with optical devices such as couplers), and optical isolators (which minimize potentially damaging feedback into lasers or other devices). These devices can be broadly divided into two categories based on their speed of operation, Tier 1 and Tier 2.

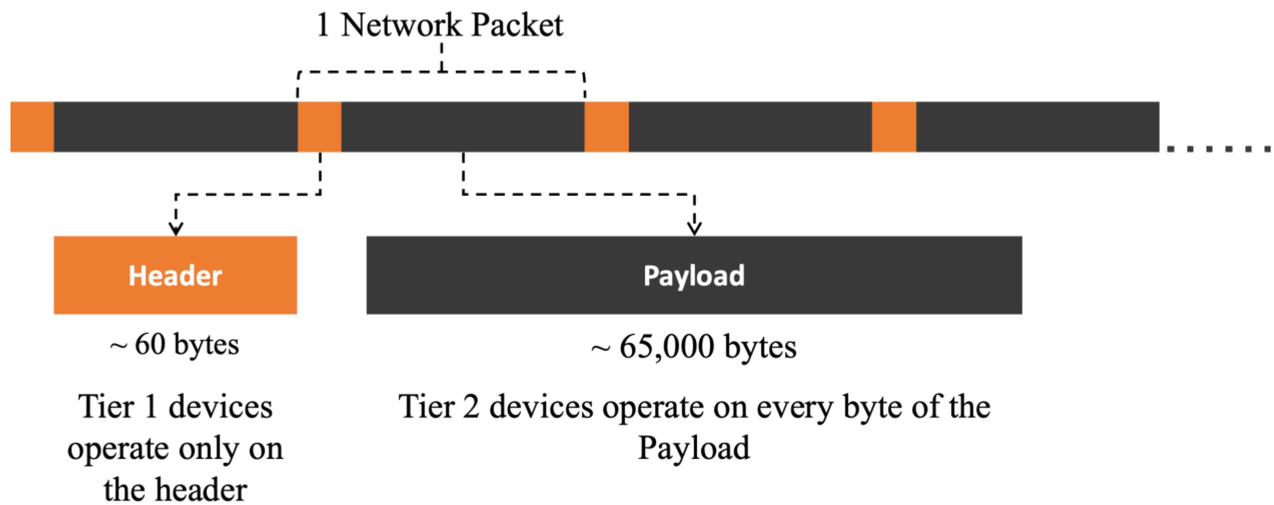

Figure 2: Schematic of the two parts of a network packet. Tier 1 devices operate only on the header, whereas Tier 2 devices operate on every byte of the payload.

To examine the difference between Tier 1 and Tier 2 devices, we consider the structure of a typical information packet sent across the internet (Fig. 2). It typically contains two main parts: a header and a payload. The header, typically about ~60 bytes in size, is a section of the packet that contains information about the packet, such as the source and destination addresses, the packet type, and other metadata. The payload, up to ~65,000 bytes, is the actual data that is being transmitted in the packet. This could be a message, a file, or any other type of data. The header and payload are both important for ensuring that the packet is delivered to the correct destination and that the data is properly interpreted by the receiving device. As this network packet enters passes through an optical network, routers and switches read only the header and route the payload to its respective

port. On the other hand, modulators which lie further down the line, operate on every bit of the payload. This translates to devices such as routers, operating at speeds of MHz (Tier 1 speed), while the modulators and detectors operate at several GHz (Tier 2 speed).

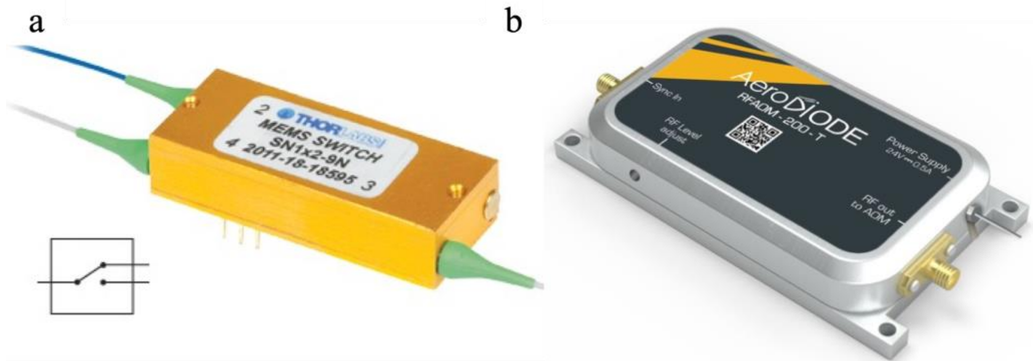

Figure 3: (a) Examples of a fiber coupled optical switch from ThorLabs, (b) Example of a fiber coupled EO modulator from Aerodiode. Each of these devices about ~5 cm in length.

Currently, many of these components are large physically separate devices that are connected via fiber optic cables, see Figure 3. While quite effective, these devices incur limitations in size, power, and cost, particularly in applications where space is a premium such as in aircraft or in data centers. As a result, significant efforts are underway to realize photonic integrated circuits (PICs) which seek to combine multiple optical devices on a single chip and co-integrate this with electronics for control [9,10]. The promise of the PIC is to radically increase the density and complexity of optical circuits, while reducing the cost and energy consumption.

While significant progress has been made [9], the realization and wide adoption of PICs across the various fields faces a key challenge. Traditional photonic active devices utilize dielectric (e.g., glass) or semiconducting materials (e.g. silicon) and are typically quite large, on the scale of 100’s of um, while electronic devices are several orders of magnitude smaller (0.01 um). This has led to integration challenges when combining electronics and photonics on a single platform.

Plasmonics, a technology which confines light to the interface of metals and dielectrics, has a potential to address challenges [11–13]. In particular, it has been shown to led to smaller devices (~10 um or less), enabling higher density optical circuits and devices on-chip. However, the technology is limited by quite extraordinarily high off-state transmission, wherein ~10% of an input signal makes it out of the device. This is simply too high to be practical and has restricted plasmonic technologies from impacting PIC technology.

In this thesis, I seek to address this challenge through a plasmon-assisted design philosophy, wherein the lossy plasmonic (i.e., metallic) element is selectively engaged or disengaged as needed. This can be thought of as turning a "knob" to route light into the lossy plasmonic element, when low transmission is desired or route light into a dielectric element, when high transmission is needed. In the work presented here, we illustrate two methods to achieve this functionality, 1) by utilizing unique materials with epsilon-near-zero properties that can be switched been low loss-dielectric state, or a high loss metallic state, 2) by utilizing resonant structures such as ring resonators that use the interference of light waves to change the pathway light takes, either through a low-loss waveguide or a lossy plasmonic ring.

In this thesis, I use this approach to explore four critical Tier 1 and Tier 2 plasmon-assisted components of PICs:

- Tier 1 Speed:
    a. Polarization controller
    b. Optical router
- Tier 2 Speed:
    a. Near-zero-index based EO modulator
    b. Polymer based EO modulator

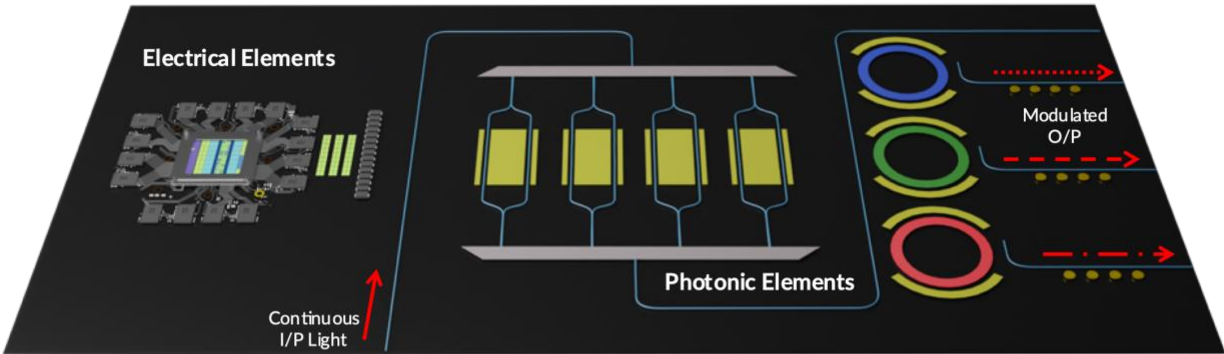

Figure 4: A rendering of a photonic integrated circuit. This semiconductor chip has both electrical and optical elements on it. As an example, electrical signals are encoded onto the optical input with the help of routers, switches, modulators, and polarization controllers.

As a result, by realizing not just one, but a suite of key devices that are compact, high performing and low loss, this work overcomes prior limitations of photonic and plasmonic technologies and enables the realization of a fully functional device platform that can be employed in future PICs (Figure 4). This advance facilitates can thus readily enable the improved co-integration of electronics and photonics on-chip and generate fundamental new capabilities in defense, data science, and telecommunication applications.

2. BACKGROUND

The optical response of materials is described by the complex refractive index, which is dispersive in nature. Depending on the type of material, such as absorbing or transparent, the complex refractive index is modelled using several models. Some of the empirical formulae are Cauchy's equation and Sellmeier's Equation often used to model transparent regions. On the other hand, more physical models such as Drude, Lorentz, P-Semi, Tauc-Lorentz and similar are used to model band edge absorption, inter-band transitions, defect related absorption or the free electron response of the material. For the materials discussed in this thesis, the Drude and the Lorentz models have been widely used and the following section describes them in further detail.

2.1. Lorentz Oscillator Model

The bound electronic response is described by the Lorentz oscillator model. The interaction between electromagnetic field and an atom with a single resonant frequency ω_0 can be modeled as a damped harmonic oscillator [14]. The damping term accounts for the energy loss by collisional processes taking place within the medium.

The equation of motion is:

$$m_0 \frac{d^2x}{dt^2} + m_0\gamma \frac{dx}{dt} + m_0\omega_0^2 x = -qE \qquad 1$$

where γ is the damping rate, q is the charge of an electron, E is the electric field of the incident light, m_0 is the mass of the electron, ω_0 is the resonant frequency and x is the electron displacement. The first term represents the acceleration, the second term represents the damping

due to collisions, the third term is the restoring force while the fourth term (right hand side) is the driving force. In the presumed case of time-harmonic excitation, the electric field is given by:

$$E(t) = E_0 Cos(\omega t + \phi) = Re\{E_0 e^{-i(\omega t + \phi)}\} \tag{2}$$

Due to a small phase lag between the time of electromagnetic energy being absorbed and the re-emitting by the oscillator, the displacement is given by:

$$X(t) = X_0 Re\{e^{-i(\omega t + \phi')}\} \tag{3}$$

Allowing E_0 and X_0 to be complex, simplifies the equation Eqs. 1 and 2 to:

$$E(t) = \tilde{E}_0 e^{-i\omega t}; X(t) = \tilde{X}_0 e^{-i\omega t} \tag{4}$$

Plugging these values into the equation of motion, Eq. 1

$$-m_0 \omega^2 \tilde{X}_0 e^{-i\omega t} - i m_0 \gamma \tilde{X}_0 e^{-i\omega t} + m_0 \omega_0^2 \tilde{X}_0 e^{-i\omega t} = -q \tilde{E}_0 e^{-i\omega t} \tag{5}$$

Solving for $\tilde{X}_0$,

$$\tilde{X}_0 [-m_0 \omega^2 - i m_0 \gamma \omega + m_0 \omega_0^2] = -q \tilde{E}_0 \tag{6}$$

$$\tilde{X}_0 = \frac{-q \tilde{E}_0 / m_0 x}{\omega_0^2 - i\omega\gamma - \omega^2} \tag{7}$$

Here, $\tilde{X}_0$ is the displacement of the atom from equilibrium, which produces a time varying dipole moment $p(t)$. This is the contribution of a single atom. If there are N atoms per unit volume, the resonant polarization contribution, P_{res}, is then given by:

$$P_{res} = Np(t) = -Nq\tilde{X}_0 = \frac{Nq^2}{m_0} \frac{1}{\omega_0^2 - i\omega\gamma - \omega^2} \tilde{E}_0 \tag{8}$$

Now, from complex form of Maxwell's equations,

$$\vec{D} = \varepsilon_0 \vec{E} + \left(\vec{P}_{background} + \vec{P}_{res}\right) = \varepsilon_0 \vec{E}(1 + \chi) + \vec{P}_{res} \tag{9}$$

Where D is the electric displacement, ε_0 is the dielectric constant of free space, $P_{background}$ is the background polarization, and χ is the dielectric susceptibility. In an isotropic media,

$$\vec{D} = \varepsilon_0 \varepsilon_r \vec{E} \qquad 10$$

where ε_r is defined as the relative dielectric permittivity. From equations 9 and 10,

$$\varepsilon_0 \varepsilon_r \vec{E} = \varepsilon_0 \vec{E}(1 + \chi) + \vec{P}_{res} \qquad 11$$

Inserting Eq. 9 into Eq. 11

$$\varepsilon_0 \varepsilon_r \vec{E} = \varepsilon_0 \vec{E}(1 + \chi) + \frac{Nq^2}{m_0} \frac{1}{\omega_0^2 - i\omega\gamma - \omega^2} \vec{E} \qquad 12$$

leads to

$$\varepsilon_r = (1 + \chi) + \frac{Nq^2}{\varepsilon_0 m_0} \frac{1}{\omega_0^2 - i\omega\gamma - \omega^2} \qquad 13$$

In Eq. 13, $1 + \chi$ accounts for the background absorptions, often represented by ε_∞, whereas the second term accounts for the resonant contributions. If several oscillators exist (absorptions), outside the measured spectrum, the contributions from them are lumped into ε_∞. Interband excitations, bound electron oscillations and lattice vibrations often lead to contributions that can be described with the Lorentz model [14].

Figure 5 shows the frequency dependance of the dielectric constant (left panel) and refractive index (right panel) of a typical dipole oscillator material that is typical of a material having infrared absorption lines, such as an ionic crystal. We see that the imaginary part of the dielectric constant, ε_2, is a strongly peaked function of frequency ω with a maximum value at resonant frequency ω_0 and a full width at half maximum equal to damping rate γ. The real part of the dielectric constant, ε_1, gradually rises from ε_{st} (the static or low frequency permittivity) as the frequency ω approaches

ω_0 from lower values. It then falls sharply, before rising again to the high frequency limit given by ε_∞. Such a response is characteristic of many materials near a resonance. For example, as shown later, a Lorentz oscillator is used to model an inter-band absorption observed in gold and titanium nitride around a wavelength of ~500 nm. This leads to strong absorption of the green part of the visible spectrum, resulting in the bright gold colors of these two materials.

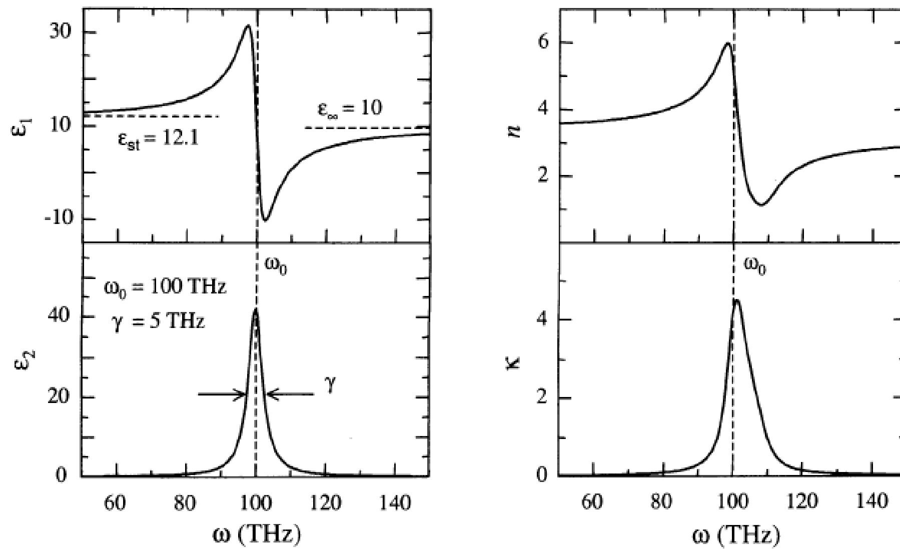

Figure 5: Frequency dependence of the real and imaginary parts of the complex dielectric constant (ε_1 and ε_2 respectively, left panel) and of the refractive index of a typical dipole oscillator material (n and κ respectively, right panel), at frequencies ω close to a resonance ω_0 [8].

2.2. Drude Model

The Drude free electron model is often used to model the optical response of metals, which tends to be dominated by free valence shell electrons [14]. When an electric field is applied, the free electrons accelerate and then undergo collisions with a characteristic scattering time τ. This acceleration and collisions of the electrons can be modelled by a harmonic oscillator model similar to equation 1, but without the restoring force term, as the valence shell electrons in metals are not bound:

$$m^* \frac{d^2x}{dt^2} + m^* \gamma \frac{dx}{dt} = -qE \qquad 14$$

where m^* is the effective mass of electron, and the damping rate is given by $\gamma = 1/\tau$. Solving the equation and plugging the displacement term into the polarization equation, we obtain the following equation for the relative permittivity ε_r:

$$\varepsilon_r = \varepsilon_\infty - \frac{\omega_p^2}{\omega^2 + i\gamma\omega}, \qquad \text{where } \omega_p^2 = \frac{Nq^2}{\varepsilon_0 m^*} \qquad 15$$

N is the free carrier concentration, and ω_p is the unscreened plasma frequency, ω_p is the frequency at which the permittivity of the material crosses 0. However, due to high frequency absorptions, given by ε_∞, the crossover wavelength red shifts. This is the crossover frequency that is observed in experiments and is referred to as the screened plasma frequency (ω_{sp}). This is not to be confused with the surface plasmon frequency that will be described later, which uses the same notation as well.

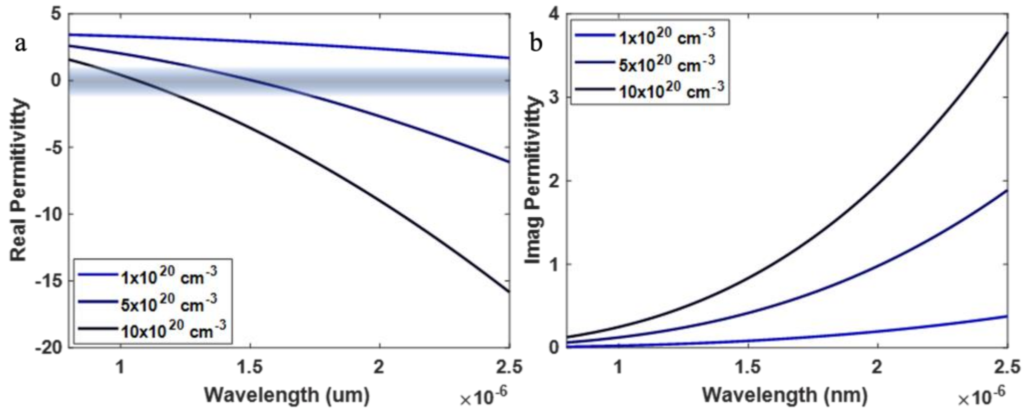

Figure 6: (a) Wavelength dependence of the real (left) and (b) imaginary (right) parts the of complex relative permittivity of a typical material of dielectric response given by the Drude model, with free carrier density N (legend insets) as a parameter. The crossover point shifts to shorter wavelengths as N increases. Blue shaded area denotes the epsilon-near-zero region. [Graphs plotted using the Drude model in Matlab.]

Figure 6 shows a typical wavelength dependence of the dielectric constant of a material modelled using the Drude model. With a clear understanding of the Drude and the Lorentz model, the next section presents details on method of optically characterizing absorbing thin films to determine the thickness, real and imaginary parts of the permittivity. This is done using a technique called ellipsometry.

2.3. Characterization of Thin Films of Metal

Many techniques exist to measure the optical properties of thin films, including spectroscopic ellipsometry (SE) and reflection transmission (RT) [15]. Both measurements utilize known material properties and physically based calculations to find unknown material properties from measured values. SE is a widely used method due to its relative ease and self-referenced nature [16,17]. It is often used for non-absorbing and semi-absorbing thin films that are easily determined from layers of unknown thickness. Absorbing films, such as metals, present a special challenge to measurement of either RT or SE. If using SE, the model often has to be supplemented by measurements of transmission intensities to obtain a unique fit to the data.

Spectroscopic ellipsometry is a powerful method for finding the refractive index and thickness of thin films. Spectroscopic ellipsometry measures the reflected change of polarized light at oblique angles to characterize the material properties. Bulk materials can be characterized from the complex reflection coefficients for s and p polarized light, see Figure 7 [18]. For thin films, reflections from the second surface interfere with the top-reflections to produce interference patterns in the measured SE spectra that can be used to calculate both film thickness and refractive index. SE data is characterized using two values, Ψ and Δ, which are calculated using the formula

$$\frac{r_p}{r_s} = \tan\Psi\, e^{i\Delta} \quad 16$$

where r_p and r_s are the complex reflection coefficient for p and s polarized light, respectively. The data represented by Ψ and Δ do not directly translate to thin film thickness and refractive index; rather, the data must be matched to a model-calculation based on best-fit sample properties. To reduce unknown parameters that describe material optical constants, a variety of dispersion equations are often implemented such as Cauchy, Sellmeier, general oscillators (e.g. Drude, Lorentz), and B-Spline.

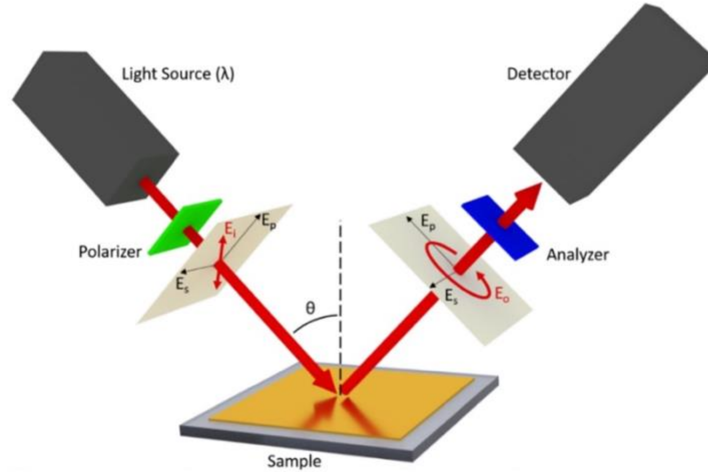

Figure 7: Schematic of spectroscopic ellipsometry. Here, a light source with wavelength λ is configured to produce an arbitrary polarization state (E_i) by a variable polarizer. The incident beam is then used to interrogate the sample at an angle θ. The polarization state of the reflected, beam (E_o) is altered by the interaction with the sample. After passing through an analyzer which allows the polarization state of the reflected beam to be measured at two perpendicular states, the complex s and p reflection coefficients of the sample can be determined [9].

As plasmonic materials are inherently lossy, general oscillator and B-Spline dispersion are used in this work. B-Spline dispersion equations provide an efficient and easy way to extract optical parameters, but some limitations exist such as an inability to extract physical meaning from the results [19]. General oscillators are a broad category of dispersion equations that use physically

derived functions, such as Drude, Lorentz, Tauc-Lorentz, and others, to model the permittivity. As an example of parameter extraction, the Drude equation has the unscreened plasma frequency (ω_p) that can be calculated as $\omega_p = \sqrt{\frac{Nq^2}{\varepsilon_0 m^*}} = \sqrt{\frac{1}{\rho_0 \varepsilon_0 \tau}}$, and from this, possible extracted values include the free electron density N, effective mass m^*, relaxation time τ , and resistivity ρ_0 if the other parameters are known.

B-Spline dispersion, on the other hand, has no physically retrievable values and is purely a fitting function to accurately match the ellipsometry data. B-Spline uses a set number of nodes for basis-functions to describe the optical functions and find a best match for Ψ and Δ. B-Spline can be implemented with Kramers-Kronig consistency to keep the optical functions physically plausible, but it does not allow for the extraction of any physical parameters from the fit. This method is very easy to implement and can then be converted to general oscillators and vice versa.

The optical model is used to generate Ψ and Δ for a given sample structure using parameters such as thickness and refractive index for each film, along with the substrate optical functions. The model-generated data are compared to the measured Ψ and Δ spectral data using a single output value to quantify the fit quality. Mean squared error (MSE) is a typical representation of how well the modelled data matches the SE data. This formalization provides a single value for how well the model fits the data, but we note that there is no ideal universal MSE value, as the value depends upon the assumptions, known quantities about the material, and measurement noise. A major limitation of the MSE is a tendency to define a “correct fit” based solely upon its minimum value. If correlation exists between multiple unknown fit-parameters, then many combinations of values can manifest in an acceptable MSE.

Dielectric films have negligible loss, so the refractive index is purely real. For dielectric films of unknown thickness, the balance of variables is data-heavy to Ψ and Δ, see Figure 8(a), as the parameters fit are refractive index $n(\lambda)$ and thickness t while the measured values are $\Psi(\lambda)$ and $\Delta(\lambda)$. This data saturation allows for very nice data fits to determine both thickness and refractive index for many material systems.

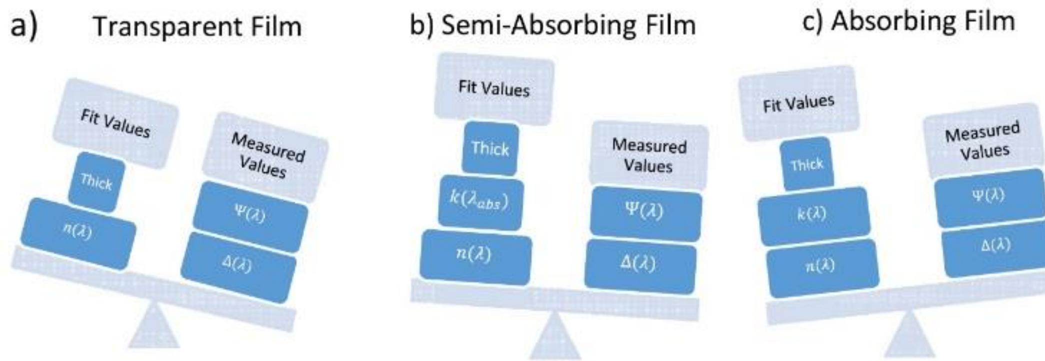

Figure 8: Comparison of data balance for a) transparent film, b) semi-absorbing film, and c) thin absorbing film. For transparent and semi-absorbing films, the ellipsometry measurement are sufficient to allow for unique retrieval of the refractive index and thickness. However, for absorbing films, the ellipsometry measurements alone are insufficient to allow for a unique retrieval of the optical properties and thickness, and additional information should be added to improve the confidence of the result [9].

When loss is added to a system the refractive index becomes complex leading to two values, n' and κ, yielding a complex index of refraction $n' + i\kappa$ at each wavelength For some materials, such as doped semiconductors, a region exists where κ is negligible so the balance of variables continues to favor Ψ and Δ, see Figure 8(b), as the thickness can be uniquely fit within the transparency window and fixed. However, in very thin films with absorption across the spectrum, the balance of data no longer favors the measured values, see Figure 8(c), which can lead to fit ambiguity. Multiple methods exist for overcoming the data discrepancy [20,21]: adding RT

measurements, interference enhancement [21], multi-sample analysis, and in situ ellipsometry [18]. Through the course of this thesis, we have relied upon transmission measurement along with SE to obtain a reliable and a unique fit to the model.

While this section elucidated the method of accurately determining the optical properties of metals and doped semiconductors, the next section discusses the interaction of EM energy with the free electrons in a metal. This interaction leads to intriguing effects which have been used to miniaturize nanophotonic devices to address the large disparity in the size scales of electronic and photonic devices.

2.4. Plasmonics

Plasmonics is the study of coherent collective oscillations of free electrons on the surface of a metal coupled to an incoming electromagnetic wave [13,22–25]. These oscillations can be thought of as quasi-particles which are part electron and part photon, called plasmons. There are several types of plasmons such as volume plasmons (volumetric oscillation of the electron population), surface plasmons (SPPs, surface oscillation of electron population) and localized surface plasmons (LSPs, surface oscillation of electrons in a finite structure). Out of these, SPPs and LSPs have been widely used due to advantages such as enhancing light matter interaction, providing THz operation bandwidth, and enabling confinement and guiding of light at scales way below the diffraction limit. Surface plasmon polaritons are waves that propagate at the interface between a dielectric and a conductor, evanescently confined in the perpendicular direction. To investigate the physical properties of SPPs, Maxwell's equations, shown below in real form, can be applied to the flat interface between a conductor and a dielectric.

$$\nabla \cdot D = \rho_{ext} \qquad (17)$$

$$\nabla \cdot B = 0 \tag{18}$$

$$\nabla \times E = -\frac{\delta B}{\delta t} \tag{19}$$

$$\nabla \times H = J_{ext} + \frac{\delta D}{\delta t} \tag{20}$$

where *H* represents magnetic field strength, *B* represents magnetic field, ρ_{ext} represents an external charge and J_{ext} represents the current density. In the absence of external charge and current densities, the curl equations can be combined to yield:

$$\nabla \times \nabla \times E = -\mu_0 \frac{\delta^2 D}{\delta t^2} \tag{21}$$

Using the identities $\nabla \times \nabla \times E = \nabla(\nabla \cdot E) - \nabla^2 E\ E$ and $\nabla^2 E$ & $\nabla \cdot (\varepsilon E) = E \cdot \nabla\varepsilon + \nabla\varepsilon \cdot E$, Eq. 21 results in

$$\nabla\left(-\frac{1}{\varepsilon} E \cdot \nabla\varepsilon\right) - \nabla^2 E = \mu_0 \varepsilon_0 \varepsilon \frac{\delta^2 E}{\delta t^2} \tag{22}$$

If we assume the variation in the dielectric constant to be negligible over one to a few optical wavelengths, Eq. 22 simplifies to,

$$\nabla^2 E - \frac{\varepsilon}{c^2} \frac{\delta^2 E}{\delta t^2} = 0 \tag{23}$$

The E-fields are assumed to have a harmonic time dependance, $E(r,t) = E(r)e^{-i\omega t}$. Inserting this into Eq. 23 yield,

$$\nabla^2 E + k_0^2 \varepsilon E = 0 \tag{24}$$

where k_0 is the wave vector of free space. This equation is known as the Helmholtz equation.

Now, we assume a 1-D geometry, for simplicity, under form of an semi-infinite half space of conductive material of complex permittivity ε_1, facing a semi-infinite half space of dielectric

material of complex permittivity ε_2 with permittivity variation in the z-direction, only (Fig. 8(a)). The plane z=0 coincides with the plane sustaining the propagating wave. This results in,

$$\frac{\delta^2 E(z)}{\delta z^2} + (k_0^2 \varepsilon - \beta^2) E = 0 \qquad 25$$

A similar equation exists for magnetic fields, as well. Using the curl equations, a set of coupled equations can be obtained which determine the spatial field profile and dispersion of propagating waves. Given that $\frac{\delta}{\delta x} = i\beta$ and $\frac{\delta}{\delta y} = 0$, this system of equations leads to the following TE and TM mode solutions:

$$\frac{\delta^2 H_y}{\delta z^2} + (k_0^2 \varepsilon - \beta^2) H_y = 0 \text{ and } \frac{\delta^2 E_y}{\delta z^2} + (k_0^2 \varepsilon - \beta^2) E_y = 0 \qquad 26$$

For a simple geometry that could sustain an SPP, such as the one shown in Figure 9(a), the TM mode equation results in a dispersion relation given by:

$$\beta = k_0 \sqrt{\frac{\varepsilon_1 \varepsilon_2}{\varepsilon_1 + \varepsilon_2}} \qquad 27$$

As shown in Figure 9, SPP is a TM mode propagating along the interface in the x direction and evanescently decaying in the z direction, both into the metal and the dielectric. Figure 9(b) shows plots of Eq. 27 for a metal with negligible damping described by the real Drude dielectric function for an air (ε_2 = 1) and a fused silica (ε_1 = 2.25) interface [13]. In this plot, the frequency ω is normalized to the plasma frequency ω_p, and both the real (continuous curves) and the imaginary part (broken curves) of the wave vector β are shown. Due to their bound nature, the SPP excitations correspond to the part of the dispersion curves lying to the right of the respective light lines of air and silica. Thus, special phase-matching techniques such as grating, or prism coupling are required for their excitation via three-dimensional beams. Radiation into the metal occurs in the

transparency regime $\omega > \omega_p$, which is referred to as the bulk plasmons. Between the regime of the bound and radiative modes, a frequency gap region with purely imaginary β prohibiting propagation exists.

In the regime of large wave vectors, the frequency of the SPPs approaches the characteristic surface plasmon frequency given by the equation:

$$\omega_{sp} = \frac{\omega_p}{\sqrt{1 + \varepsilon_2}} \qquad 28$$

as can be shown by inserting the free-electron dielectric function into Eq. 27. In the limit of negligible damping of the conduction electron oscillation (implying Im [ε(ω)] = 0), the wave vector β goes to infinity as the frequency approaches ω_{sp}, and the group velocity $v_g \rightarrow 0$. The mode thus acquires electrostatic character and is known as the surface plasmon.

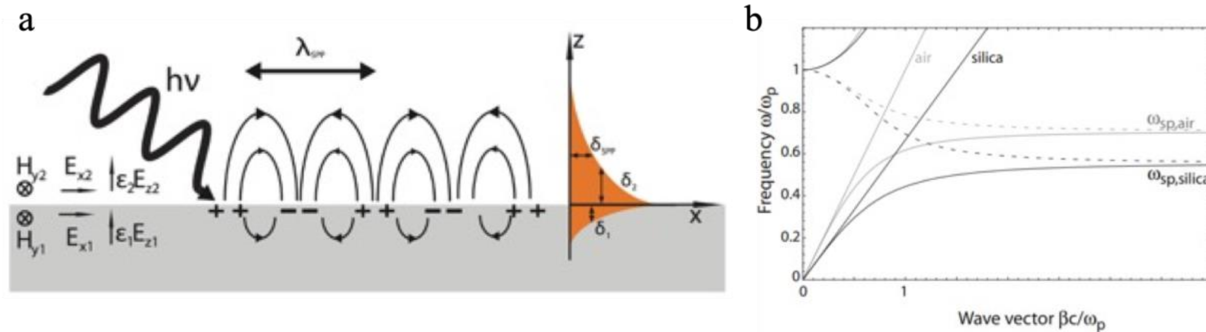

Figure 9: a) Geometry of a dielectric and metallic slab to sustain SPP propagation along the interface; b) Frequency vs. wavevector diagram of the SPP mode and the metal dielectric interface when the dielectric is air and silica, respectively [17].

Plasmonics has enabled confinement and control of light at scales much smaller than the diffraction limit and has led to enhancement of light–matter interaction. Over the last two decades, a variety of applications including chemical sensors [26], nonlinear optics [27], metamaterials [28], and transformation optics [29] have immensely benefited from the plasmonic

properties of metals leading to extraordinary demonstrations of devices such as a perfect lens [30], optical black holes [31], and negative refraction [32]. More recently, the focus has shifted to realizing dynamic and reconfigurable meta-devices, such as lenses [33], beams steerers [34], modulators [35], and phase shifters [36], for potential applications in THz telecommunications, label-free and non-invasive biosensors, and compact LIDARs. As the constituent materials used to build these devices (dielectrics such as silicon, lithium niobate, indium phosphide or plasmonic elements such as gold, silver and aluminum) do not offer large tunability, many of them incorporate a dedicated dynamic layer based on phase-change materials [37], electro-optic polymers [35], micro-electro-mechanical components [38], and, more recently, an epsilon-near-zero (ENZ) condition [39,40]. Among these, ENZ materials are particularly attractive as they offer large tunability under both electrical and optical control, offer sub-picosecond response times, and are of purely solid-state nature [41–44]. The next chapter introduces ENZ materials and details their advantages.

2.5. Epsilon Near Zero Media

Epsilon near zero (ENZ) materials are a class of materials that exhibit permittivity close to 0 in a given wavelength range. As the permittivity approaches zero, the boundary conditions at the interface between a material, labeled 1, of permittivity ε_1 and an ENZ material, labeled 2, of permittivity ε_2 dictate that the normal components of the electric displacement vector must be continuous across the boundary between two materials. Due to this continuity boundary condition, $\varepsilon_1 E_{(1,n)} = \varepsilon_2 E_{(2,n)}$, when ε_2 approaches 0, the electric field in material 2 tends to infinity. This leads a large E-field enhancement in material 2 (Fig. 10) which drastically improves light-matter-interaction (LMI).

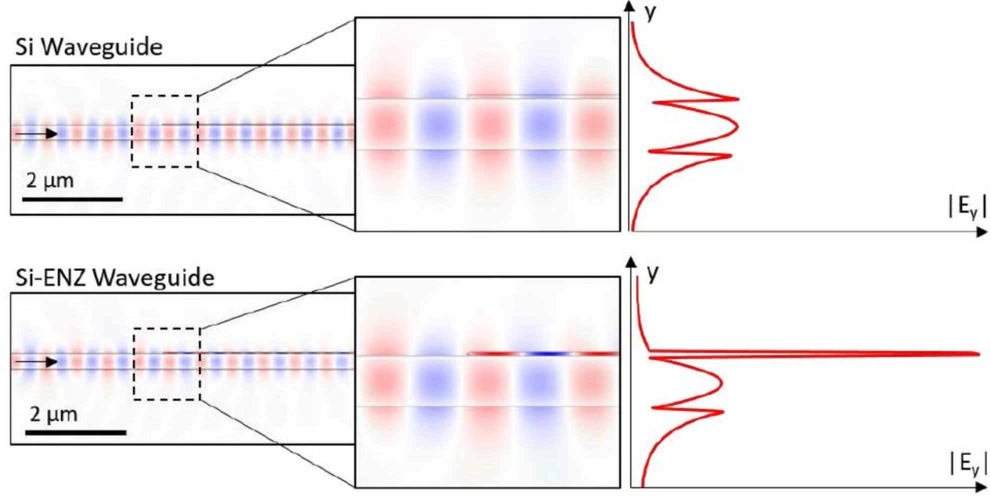

Figure 10: Vertical (y) component of the electric field for a mode propagating in a silicon waveguide on glass a) cladded by air, b) cladded with air and a thin layer of ENZ material. The thin ENZ layer results in a strong confinement of the electric field.

Furthermore, if the loss in these materials is low enough, such that not only the permittivity but also the refractive index tends to 0, other effects such as wavelength expansion, diverging group and phase velocities and DC light are observed [41,45,46]. Diverging velocities can be observed by considering a Drude dispersion. As $\omega \rightarrow \omega_p$ in the lossless case, $n(\omega) \rightarrow 0$. Since phase velocity is given by the equation, $v_p = \frac{c}{\sqrt{\varepsilon(\omega)}}$, where $\varepsilon = n^2/\mu$, this leads to $v_p \rightarrow \infty$. However, the group velocity is dependent on the slope of the permittivity and is represented by the equation:

$$v_g = \frac{d\omega}{dk} = \frac{c\sqrt{\varepsilon(\omega)}}{\varepsilon(\omega) + \frac{\omega}{2}\frac{d\varepsilon(\omega)}{d\omega}} \qquad 28$$

As it is evident, due to the finite slope, the group velocity tends to 0. The phase velocity tending to infinity is referred to as DC light, as this leads to 0 phase accumulation. While the group velocity tending to 0, is the slow light effect which enhances light matter interaction (Figure 11).

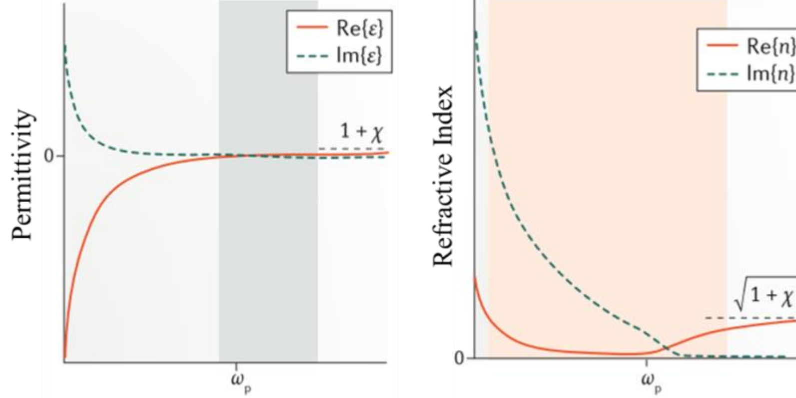

Figure 11: Complex permittivity (left) and complex refractive index (right) components given by a typical Drude model [34].

The physical mechanism behind this can be explained by considering the propagation of light through a low-loss ENZ media. The incident electric field polarizes the atoms, which then reradiate (scatter) the light with a frequency-dependent phase delay, $\Delta\varphi(\omega)$, determined by the loss of the oscillator γ. This process occurs many times as the light passes through the material, which effectively contributes an additional, spatially varying phase (momentum) to the propagation of the wave, $a(\omega) = \Delta\varphi(\omega)/d$, where ~~d~~ d is the distance between scattering events. The phase velocity becomes $v_p = \omega/(k_0 - a)$, where k_0 is the free-space momentum; thus, the phase velocity diverges when $a = k_0$, essentially the condition when the phase lag produced by the scattering events compensates for the phase gain of the wave over the same effective distance, such that the wave appears uniform over that distance. Such a large phase shift typically occurs when strong light–matter coupling is present (that is, near resonance) and dispersion results in a reduced group velocity [41].

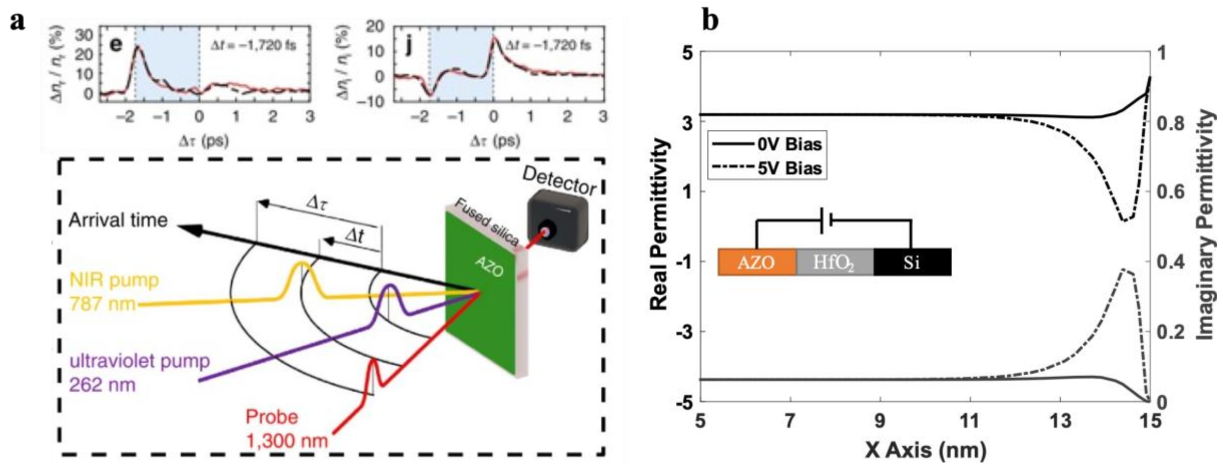

Figure 12: (a) Ultra-fast (few ps) response time of an AZO film under optical tuning [42]; (b) Change in local permittivity of an AZO film under electrical biasing where the AZO forms the anode of a capacitor structure of AZO/ HfO_2/ Si. x axis denotes the position in the AZO film normal to the planar interface with HfO_2 (located at x=15 nm [Calculated using COMSOL Multiphysics and Matlab]

Although ENZ properties can be realized in several ways, transparent conducting oxides (TCOs) have received significant attention due to their intrinsic ENZ condition. Specifically, TCOs can support heavy doping without any considerable degeneration of structural quality and exhibit an ENZ regime at technologically relevant wavelengths. Furthermore, these materials are particularly attractive for use in active devices as they offer large tunability under both electrical and optical control (Figure 12) [47], offer sub-picosecond response times [48,49], and are of purely solid-state nature [47]. Apart from providing excellent tunability, TCO's also exhibit enhanced LMI, due to slow light effects, enabling more compact and energy-efficient devices, in the ENZ region. As a result, these materials have been shown to enhance several nonlinear optical processes (such as adiabatic frequency shifts, second and third harmonic generation, and four-wave mixing) and have led to the realization of sub-micron modulators and high angle beam steers, making these materials

a key for several areas of dynamic nanophotonics. The following section provides information about some of these works and discusses their limitations.

2.6. Prior Works and Challenges

Briefly summarizing the discussion thus far, optical technologies have led advancements in several key areas such as high-speed and efficient data transfer through optical fibers, non-invasive biosensors such as the heart rate sensors found in smart watches and optical interconnects in data centers. Most of these advancements have been fueled by the rise of silicon photonics as it provided a CMOS-compatible platform with numerous low-loss passive and active components such as waveguides, delay lines, phase shifters, modulators, switches, nano-resonators etc [50]. While Si photonics has been excellent for passive devices, active devices are in general quite large (many wavelengths) and are relatively slow (sub-MHz for switches/shifters or ~10 GHz modulators), leading to a low compute density, see Figure 13(a) (Tier 1 speed devices operate on data packets in the kHz to MHz range, Tier 2 speed devices operate per-bit in the GHz range). As a result, numerous parallel channels and/or advanced formats (wavelength multiplexing, phase shift keying, etc.) must be used to push bandwidths, which ultimately increase system size, cost, power consumption, and complexity. As a result, photonic active devices must generally employ long interaction lengths or high-quality factor resonators which limit the frequency at which the devices may operate due to a large capacitance or long cavity ring-down time ($f \sim 1/RC$ or $\sim 1/Q$).

On the other hand, plasmonic structures have been utilized to enhance the light-matter-interaction in active devices. As discussed earlier, this is achieved by confining light to spaces smaller than the diffraction limit and reducing the group velocity. As a result, plasmonic modulators have already demonstrated high-speed switching (> 200 GHz) with low energy consumption (sub-fJ/bit)

in a compact footprint (~5 μm^2). Yet, these devices are only able to achieve an off-state transmission (α_o) of ~10%, which is simply insufficient for many applications. Furthermore, the

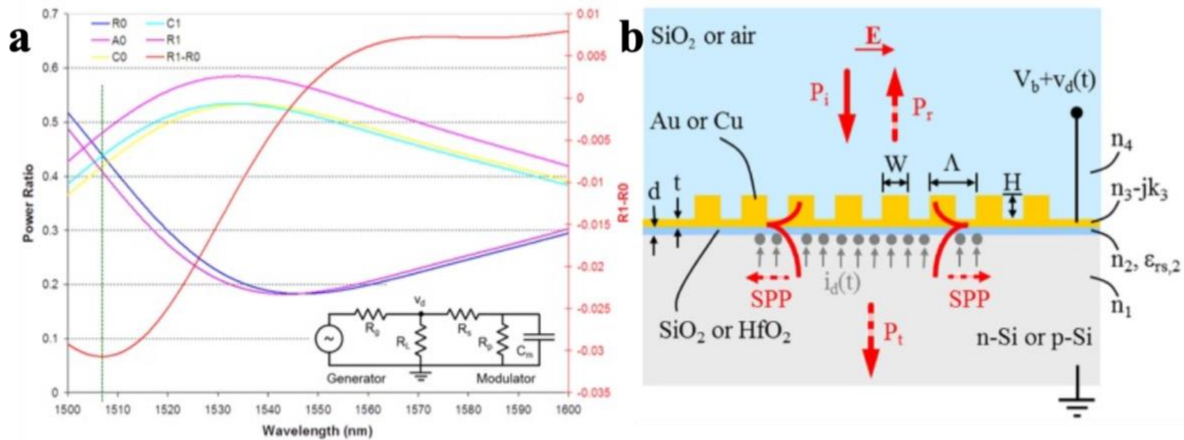

Figure 13: (a) and (b) are examples of a plasmonic metasurface design which although offer large changes in index, suffer from broad resonances [42].

high loss has been a detriment to free space, metasurface designs as well and has resulted in resonances on the order of 100's of nm FWHM (Figure 13(b)) [51].

> ***This essentially establishes a tradeoff: The energy confinement leads to larger modulation, which is counter acted by broader resonances or low insertion losses. As a result of this widespread loss issue, the practicality of plasmonic-based devices has been limited and has led to the belief that "plasmonics is too lossy to be useful" [22,52,53].***

To address the issue, the general theme of this thesis is to utilize plasmon-assisted or hybrid design approaches coupled with developing CMOS compatible tailored materials that are synergistically work with each other. This enables us to develop on-chip devices and carefully balance the modulation-loss tradeoff. More specifically though, while we simulate several such designs, the

goal of this these is to fabricate and test an all-oxide modulator device, which will serve as a proof-of-concept demonstration of the plasmon-assisted design philosophy.

2.7. Performance Metrics

Before exploring the device designs, it is essential to understand the performance metrics. The performance of EO Modulators is evaluated based on parameters such as extinction ratio (ER), insertion loss (IL), footprint, energy-bandwidth product, speed, power consumption, etc.

Extinction ratio (ER): ER or Modulation depth (MD) is a measure of effectiveness of the modulation mechanism on the light intensity at the output end between a modulator's on and off state. In other words, the difference between light intensities at the output end when a modulator is set to high transmission (HT) and low transmission state (LT) respectively. It is usually expressed in dB units [54,55]. For example, the ER of a modulator can be defined by:

$$ER = -10\log_{10}\frac{I_{O/P}}{I_{I/P}}\ (\text{dB}) \qquad 29$$

As a numerical example, a 3 dB ER corresponds to a reduction of light intensity by 50% at a low transmission state compared to the intensity at a high transmission state. Most modulators operate based on an ER of 6 to 9 dB.

Insertion Loss (IL): IL is the propagation loss or off-state loss, which is a measure of the optical loss the light signal suffers as it traverses through the modulating region in the passive state of the device. A low IL is desirable. For example, the IL of a Si rib-waveguide-based modulator can be determined by calculating the mode loss (from the imaginary part of the effective mode index derived from the 2D analysis given by Eq. 2.24 of ref. 50), as

$$\alpha = 10\,log\left|e^{-\frac{4\pi}{\lambda}Im\{n_{eff}\}}\right|\ (dB/um) \qquad 30$$

EO Bandwidth: EO bandwidth (BW) or speed measures how fast an electrical signal can be encoded onto an optical signal and directly indicates the maximum bit rate that a modulator can support [55]. It is usually defined by the frequency at which a modulator performs a 3 dB modulation given by the expression $f_{3dB} = \frac{1}{2\pi RC}$, where R and C refer to lumped resistance and capacitance of the device.

Energy Consumption: This is a measure of the energy consumed to modulate a bit from 0 to 1, or the transmission of light from either low to high, or vice-versa. In other words, it quantifies the energy expended in producing each bit of data [54,56] . It is usually theoretically determined as opposed to being experimentally measured. In case of capacitor-based modulators, energy consumption ~~it~~ can be determined using the expression $\frac{1}{4}CV^2$. Since the votlage term is squared, ~~a~~ highly energy efficient devices need to operate at low CMOS level voltages. Current state of the art modulators consume~~s~~ several pJ/bit. To sustain the rapidly growing demand this should fall to sub-100 fJ/bit levels.

3. NANOPHOTONIC DEVICES

3.1. Plasmon-Assisted Design Approach

Telecommunication applications and technologies have rapidly evolved over the past two decades, and continue to do so, with no end in sight. It has transformed from slow (kbps) point-to-point communication from home and offices to connected devices, practically everywhere. This tremendous growth has been supported, in part, by a deeper penetration of optical technologies such as fiber to home (FTTH), short distance fiber communication (within data centers) and massive parallelism. However, as 5G and millimeter-wave technologies become more ubiquitous, there is a need for optical components that are more efficient and provide a bandwidth closer to that of the carrier wave (current optical bandwidths are device limited, about a 1000x slower than what the carrier signal can theoretically carry).

However, current state of the art optical components relies on the use of dielectrics, such as Si, Si_3N_4 and $LiNbO_3$, which inherently have poor tunability [54,57]. This in turn leads to photonic devices with long interaction lengths or high-quality factor resonators which limit the frequencies at which the devices may operate due to a large capacitance (in non-traveling wave systems) or long cavity ring-down time ($f \sim 1/RC$ or $\sim 1/Q$) [54,57,58].

On the other hand, plasmonic devices offer great potential for solving the limitations of silicon photonics. Recent literature has demonstrated plasmonic modulators realizing speeds > 200 GHz in compact footprints (<20 μm^2). However, large insertion losses have limited practical applications. To minimize the losses, many researchers have clung to the use of gold and silver (the highest performing plasmonic materials) despite limited suitability for co-integration with

CMOS and extreme cost of such materials, but even this has not solved the problem. As a result of the challenge of increasing compute/area without simultaneously increasing insertion loss, the community has witnessed a diagonal transition in the corresponding performance plot as opposed to the vertical one once promised (Figure 14). In fact, the issue has persisted for so long in literature that it may be assumed the problem is beyond solving.

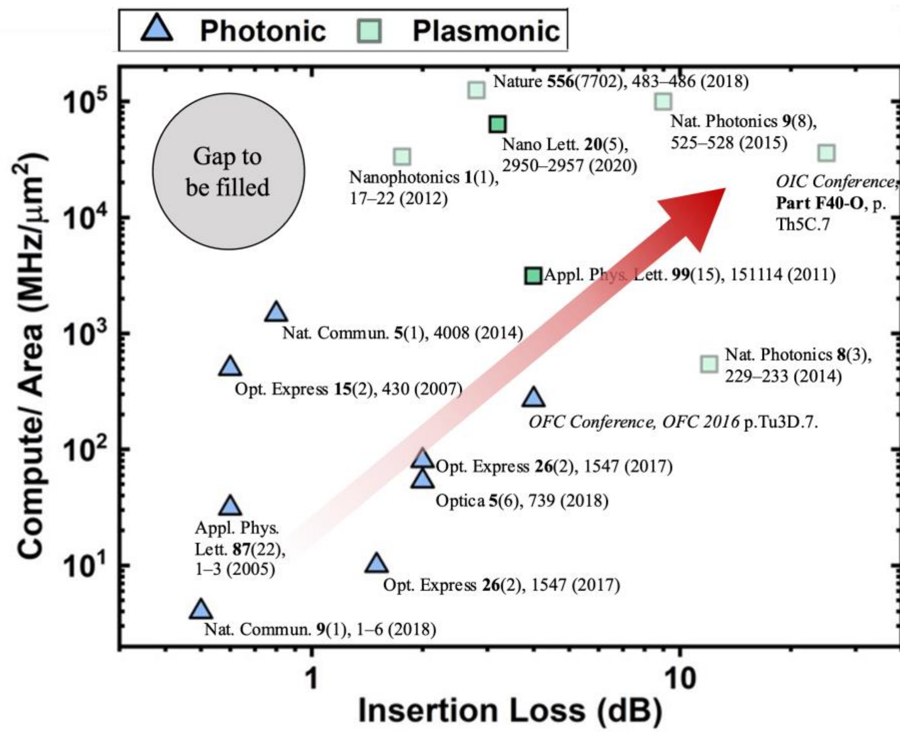

Figure 14: Plot of compute/area vs insertion loss for several photonic and plasmonic devices in literature. In the quest to increase the available compute/ area, these devices have simultaneously led to an increase in insertion loss. The goal is to achieve a vertical not diagonal transition. The gap which we want to fill is represented by the grey shaded region.

To counter this issue, we leverage a groundbreaking plasmon assisted design philosophy to realize a panoply of devices that benefit from high speed of plasmonic devices while maintaining the benefits of low loss photonic systems. The devices are designed such that the plasmonic nature can be selectively engaged and disengaged. Intuitively, it makes sense to engage the lossy

plasmonic component in the on-state of the device (defined as the state of low transmission) and disengage the plasmonic component in the off-state (defined as the state of high transmission).

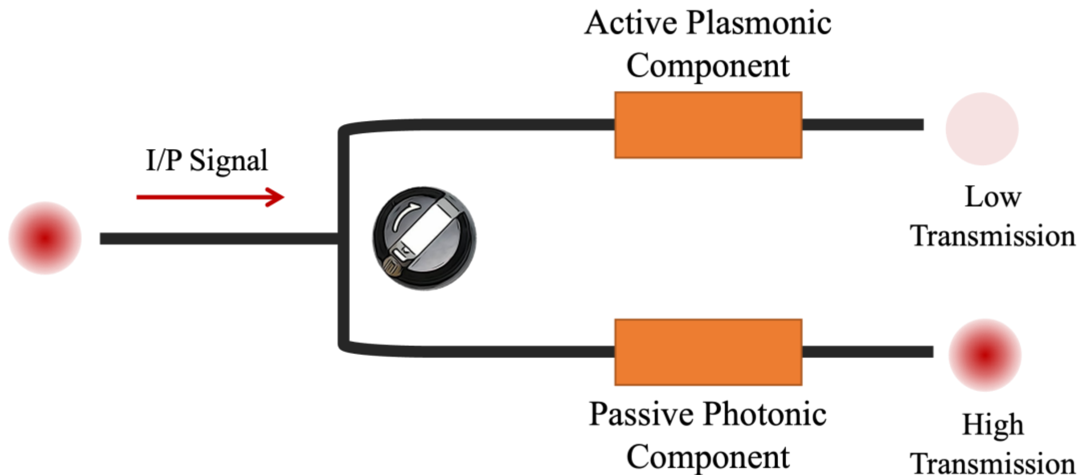

Figure 15: Schematic of the plasmon-assisted design principle. Using a "knob", the input signal is routed to either the lossy plasmonic section, or the low-loss photonic section, dependent on the desired on or off state of the device.

The plasmon-assisted device concept is highlighted in Fig. 15. An input signal enters the device and, by adjusting a "knob", it can be sent to a low loss channel, which results in a high transmission. This channel, for example, could be purely dielectric in nature. On the other hand, when low transmission is needed, the signal gets routed to a high loss plasmonic channel. This approach intuitively yields a combination that exhibit a of high modulation depth and low insertion loss.

The knob can be implemented in two ways, by either using materials that switch between metallic and dielectric states or structures that can route light into different channels. In a recent, demonstration of a plasmon-assisted switching device, C. Hafner et. al. [35], were able to reduce the insertion losses by a factor of 3, from 8dB to 2.5dB, by utilizing a "structured knob", such as an electro-optically engaged ring resonator (Figure 16). In the first iteration of a non-plasmon-

assisted device design, a Mach-Zehnder modulator was demonstrated. The input signal passed through the lossy metal-insulator-metal (MIM) waveguide, in both the on- and the off-state. This resulted in an IL of 8dB. On the other hand, switching to a MIM ring resonator coupled to a Si bus waveguide resulted in a device design, in which the input signal couples into the lossy plasmonic ring only in one of the states (the low transmission state in this configuration). The coupling and decoupling are based on constructive and destructive interference which in turn can be modulated by changing the index of the polymer (backfilled into the MIM slot). This plasmon-assisted configuration resulted in an IL of 2.5 dB, a 3X reduction as compared to the non-plasmon-assisted device design. However, since the device architecture relied on an all plasmonic, metal insulator-metal ring configuration, the insertion loss was prohibitively high to begin with. Another method recently proposed to engineer the "knob" of a plasmon-assisted device is to use ENZ materials [39]. As discussed in section 2.5, these are materials for which the permittivity can be tuned close to 0 at an operating wavelength of interest, such as, in our case, within the range 1300 to 1550 nm.

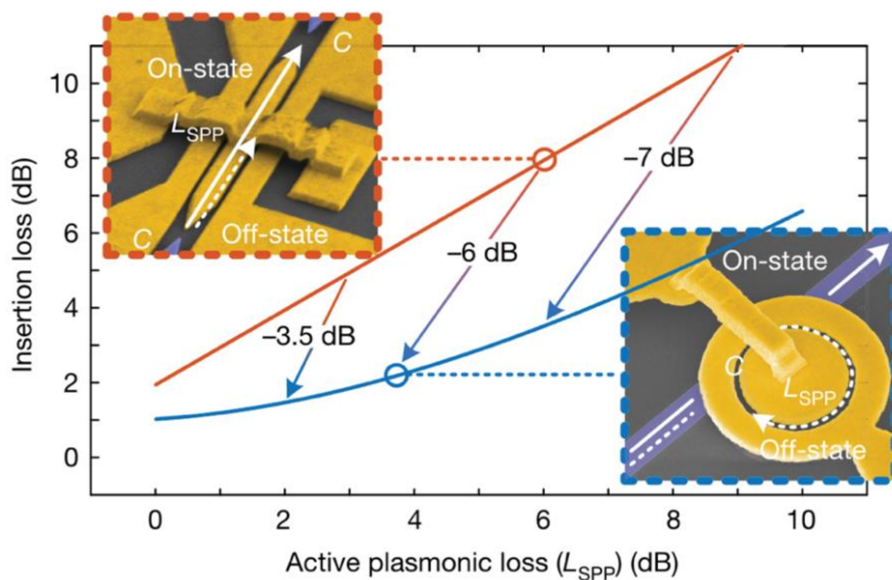

Figure 16: Comparison of plots of insertion loss vs. active plasmonic loss for the all-plasmonic Mach-Zehnder interferometer modulator of ref. [59] and the plasmon-assisted ring resonator modulator of ref. [30], respectively. Losses in the plasmon assisted design can be reduced by more than 6 dB, primarily due to the loss bypassing mechanism in the passive state.

Through the rest of the thesis, I explore the following 4 devices and their respective "knobs":

- Tier 1 Speed Devices:
    a. Opto-mechanical polarization controller: structured knob
    b. Opto-mechanical optical router: structured knob
- Tier 2 Speed:
    a. Epsilon-near-zero based EO modulator: material knob
    b. Polymer based EO modulator: material knob

These devices form the foundation of a CMOS-compatible integrated plasmonics toolkit, which when paired with established silicon photonics for low loss routing and guiding will fuel the continued growth of integrated photonics for applications including telecommunications and LIDAR while enabling new opportunities for reconfigurable photonic circuits and networks.

3.2. All-Oxide Plasmon Assisted EO Modulator (Tier 2 Speed)

Electro-optic modulators exhibiting greater than 6 dB modulation while maintaining sub-1 dB insertion losses in an energy efficient (sub-500 fJ/ bit) and compact footprint (sub-10 um^2) are imperative to sustain the trends of increasing data consumption. To realize such a device, it would be highly beneficial to "engage the lossy plasmonic-nature" of the device when modulation is desired, while "turning-off the plasmonic-nature" in the off-state (high transmission). This distinctive design approach can be accomplished by using ~~a~~ transparent conducting oxide (TCOs) and their unique ability to act as metals, dielectric and epsilon-near-zero materials in the near-infrared region based on the free carrier density.

While EO modulators using ENZ materials have been demonstrated in the past, such as the ones shown in Figure 17, the IL exhibited by these devices have been relatively high, 2 to 4 dB. The origin of the high IL can be traced to the incorporation of the metal in the active region. Due ti this, the input signal never experiences a low loss dielectric channel, as while the ENZ material switches between the metallic and dielectric states, the metal always remains in the high loss plasmonic state. This leads to large losses in the off-state primarily due to two reasons. The metal excites a hybrid mode, which results in ohmic losses and causes a large mode-mismatch between the rib and the hybrid waveguide, which causes back reflections.

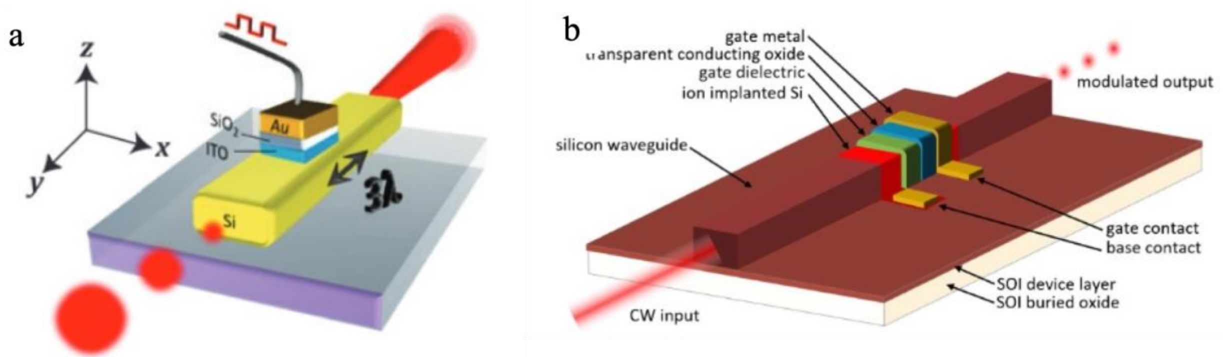

Figure 17: Examples of EO modulators in literature fabricated using ENZ materials. Notice the metal layer in the active region in both these devices. The metallic layer excited a hybrid mode which causes an increase in IL due to ohmic losses [39,60].

In our work, we improve on this configuration by removing the metal layer from the active region of the device, to reduce the insertion loss. However, the metal layer serves two key roles. It pulls out the E-field from the bulk of the Si waveguide and confines it in the low index region, while also serving as the top electrode. Replacing the metal, with a conducting oxide addresses the second point, however now the E-field reside in the bulk of the Si waveguide, as opposed to the low index region on top of the waveguide. This would lead to a reduced MD, as the E-field no

longer experiences the index change. To counteract this, our design incorporates a slot waveguide, which confines the E-field in the low index region between the two Si waveguides.

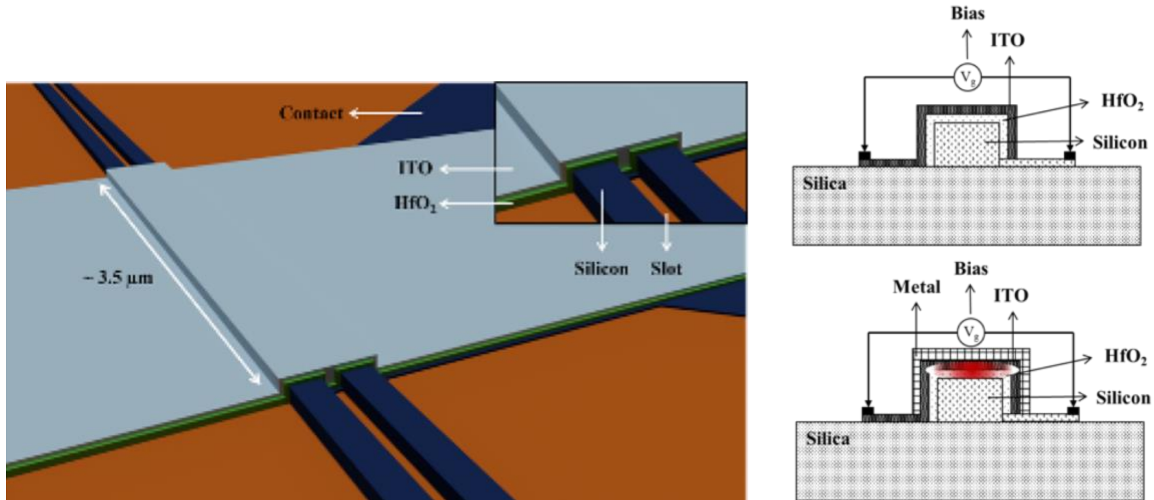

Figure 18: (a) A schematic of the slot waveguide electro-optic modulator. The inset shows the zoomed in version of the active region, (b) Example of plasmon-assisted design approach, (c) Representative image of devices explored in literature.

The device design consists of a silicon slot waveguide wrapped around by a dielectric spacer which is comprised of HfO_2, as shown in Figure 18(a). The dielectric spacer is further wrapped around by a transparent conducting oxide, which can act both as a metal and a dielectric at technologically relevant wavelengths, depending on the free carrier density of the material. As can be seen, this underlying structure is very similar to other devices reported in literature, which have a base waveguide, a dynamic tunable layer and a metal wrapped around the waveguide (Figure 18(c)), although with two important differences, the exclusion of metal from the active region and the incorporation of slot waveguide, as opposed to a rib waveguide. Several devices in the literature incorporate the metal layer due to the inherent advantages such as enhanced modulation, engrained electrical contacts and the ability to extract light out of the photonic mode into the plasmonic mode,

for better control (Figure 18(c)). However, from Figure 14, it is evident that the plasmonic element also leads to drastically increased insertion loss, detrimentally impacting the performance of the device. To overcome this limitation, while maintaining the enhanced modulation advantage, the plasmon-assisted design philosophy is implemented, replacing the metal layer with an epsilon-near-zero material that can switch between a high loss "metallic state" and a low loss dielectric state (Figure 18(b)). The engaging and disengaging of the plasmonic element can be accomplished using several methods such as ring resonators, directional couplers, phase change materials and TCOs. The first two guide light into different sections of the device while the latter are based on dynamically changing material properties that can exhibit metallic and dielectric permittivity. The proposed device is based on the use of TCOs, due to their projected sub-picosecond response times. However, metal serves another key role – extracting light out of the Si waveguide and into the low index medium. To enable this effect, the design is switched from a rib waveguide (Figure 18 (b)) to a slot waveguide (Figure 18(a)).

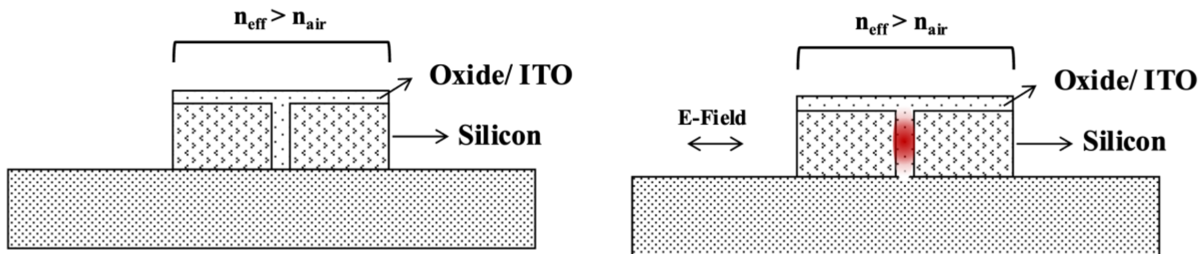

Figure 19: Schematic of the proposed slot waveguide configuration, illustrating how the effective index of the two silicon waveguides combined with an TCO-filled slot in the middle is larger than that of the surrounding air. Subsequently, the E-field is localized in the low index oxide medium due to the continuity of the D-field.

While it is well known that light is guided in a layer of a high index medium surrounded by a low index cladding, such as in the case of a rib waveguide, the slot waveguide induced profile of

confined light in a low index medium might seem counterintuitive at first glance (Figure 19). However, if the overall effective index of the two Si waveguides with a slot in the middle is considered, it will prove to be higher than that of air or oxide around it. Thus, the two Si waveguides along with the slot in the middle form a super mode, which guides light. The E-field profiles of within the super mode is governed by the boundary conditions. When the E-field is normal to the slot, the D-field continuity condition ($\varepsilon_1 E_{1,\perp} = \varepsilon_2 E_{2,\perp}$) kicks in. This results in the medium with a lower index having a larger E-field, which in the case of the slot super mode, results in the slot carrying the stronger E-Field. It is the same reason why an ENZ material experiences large E-field enhancements, when its permittivity approaches 0.

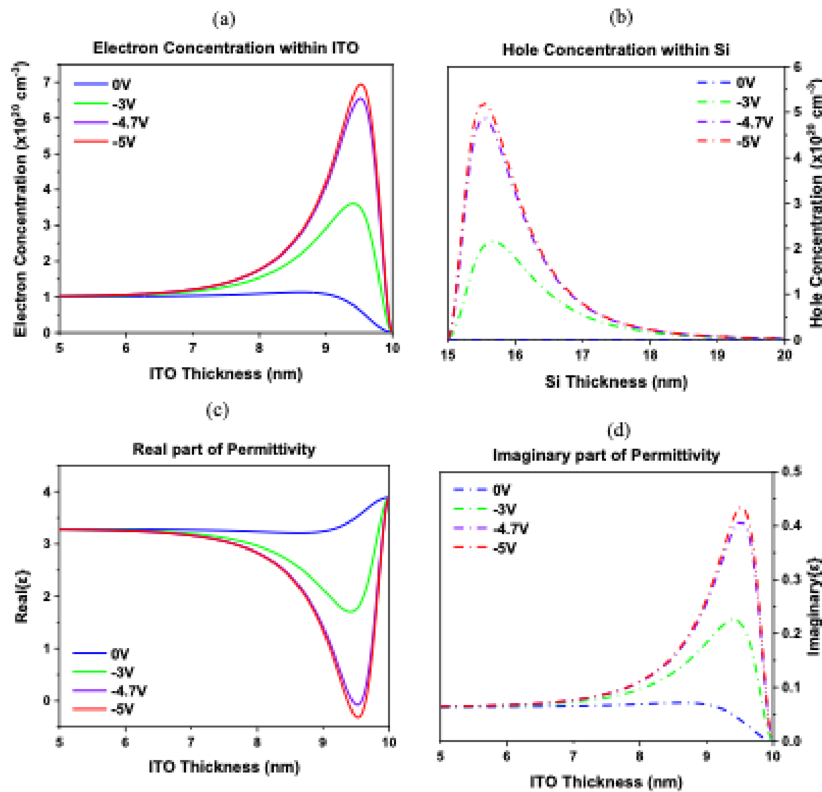

Figure 20: (a-b) Electron and hole concentration within ITO and p-type Si as a function of gate voltage. The bulk hole carrier concentration within p-type Si is $1x10^{18}$ cm^{-3} (c-d) Real and

imaginary part of permittivity within ITO as a function of gate voltage and position within the ITO layer. Simulations done using a COMSOL FEM solver [61].

The portion of the silicon slot waveguide underneath the dielectric (Figure 18(a)) is p-doped to a free carrier density of 10^{17} to 10^{19} cm^{-3}. This carrier concentration results in sufficient conductivity of the silicon rib waveguide to serve as the contact, while being low enough to exhibit a positive permittivity at the telecommunications wavelengths. The TCO is n-doped to a carrier concentration such that it exhibits a positive value of permittivity when no bias is applied, but on application of a bias (Vg), exhibits a permittivity between -1 and 1. In the case of ITO, this range corresponds to a free carrier density of about 1.0×10^{20} cm^{-3}.

In the off-state (high transmission), a continuous wave of in-plane polarized electromagnetic wave, at 1550 nm, guided by the silicon slot waveguide, passes through the modulator. Most of the energy is confined within the silicon slot waveguide and interacts with the dielectric spacer and the TCO. In the current state, all components of the system exhibit a positive permittivity with minimal loss. This is referred to as the all dielectric, off-state. In the on-state (low transmission), a bias is applied across the silicon contact and the ITO contact. This leads to the accumulation of charge carriers at the interface of ITO / dielectric spacer and the silicon waveguide / dielectric spacer, as shown in Figure 20(a,b), which displays simulations done using a ~~an~~ COMSOL finite-element-method (FEM) solver. A voltage-induced increase in charge carrier density at the interface leads to a decrease in permittivity, as predicted by the Drude Model. Referring to Figure 20(c,d), the permittivity at the ITO and dielectric interface approaches and crosses 0. This region is referred to as the epsilon near zero regime. When the permittivity approaches 0, the electromagnetic radiation experiences wavelength expansion, because of which the group velocity tends to 0 and the phase velocity tends to infinity. Furthermore, due to the continuity of the normal component of the

displacement field, the electric field within the epsilon near zero media becomes very large. All these effects put together lead to enhanced light-matter interaction. In the current design, on application of a bias, the metallic/ENZ component of the system is engaged and the electromagnetic radiation from the silicon waveguide is pulled out into the thin ENZ region. This leads to significantly higher loss in the system, as compared to the state with no bias. It is in this way that an incoming continuous wave of light can be encoded with information and transformed into a pulse train based on the given electrical signal.

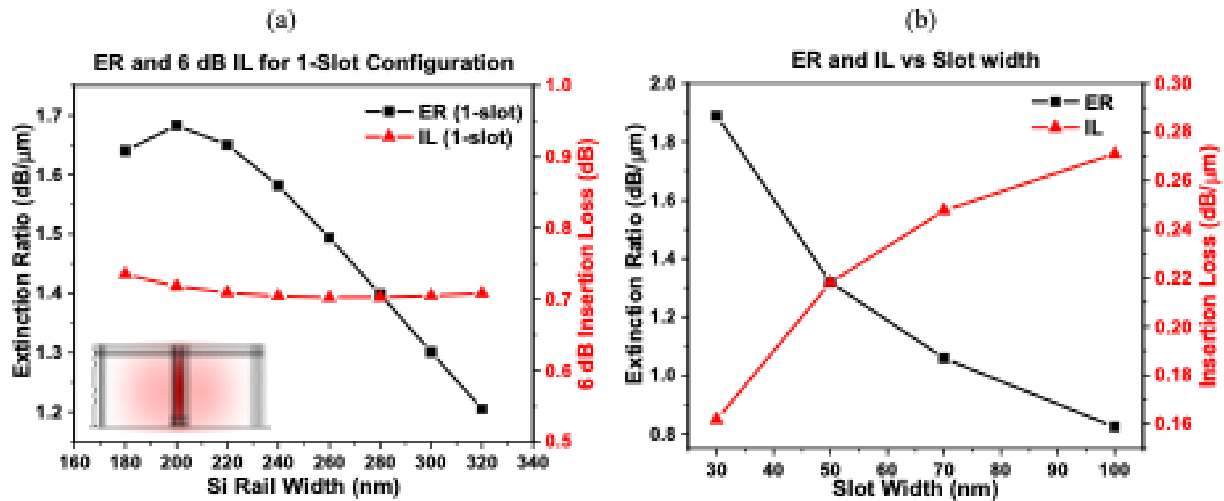

Figure 21: (a) ER (dB/µm) (black) and IL for 6dB modulation (red) for a slot modulator. The slot width is 40 nm, (b) ER (dB/µm) and IL (dB/µm) for single slot configuration as a function of slot width. A smaller slot width is more favorable to obtaining a low IL and high ER. The rail width is fixed and equal to 200 nm

The critical parameters of the device are the width of the rail waveguides and the slot width. Figure 21(a) shows the influence of the rail width on the ER (per um) and the IL for 6 dB ER. As the rail width varies from 140 nm to 340 nm, the insertion loss (IL, loss in the off-state) stays roughly constant, but however, the ER per um drops. In theory, this would result in the requirement of a longer device to obtain a target ER, which in this case is 6 dB. This in turn would increase the

capacitance and would both reduce the bandwidth and increase the energy consumption of the device. Thus, a smaller rail width is preferred. The next critical parameter is the slot width (Figure 21(b)). An increase in the slot width not only reduces ER (per um), but also increases the IL (per um). This is highly detrimental to the device from all perspectives. Thus, a thinner slot is preferred. However, the slot thickness is limited by the thickness of ITO and the oxide layer. To build sufficient capacitance for carrier accumulation, while avoiding tunneling effects, a 5 nm thick oxide layer is preferred. At the same time, an ITO films with thicknesses below 20 nm, typically display poor quality and increased losses due to surface scattering effects. Thus, on the lower end, the slot width is limited by the thicknesses of ITO and oxide.

From the perspective of the capacitor, the dielectric spacer thickness is a critical parameter as it affects the maximum amount of free carrier accumulation at the interface. In the current device design, the optimum spacer thickness was found to be 5 nm. The accumulation of charge carriers can be modelled using the Density Gradient Model, that considers quantum confinement effects as compared to the Drift Diffusion Model, which does not. The Density Gradient Model ~~This~~ results in a grossly overestimated free carrier accumulation along with an incorrect exponentially increasing profile. The more physically accurate profile modelled using the Drift Diffusion Model is shown in Figure 20(a,b). Lastly, the carrier concentration and the mobility of ITO were assumed to be 1.0×10^{20} cm^{-3} and 40 cm^2/Vs.

<u>For a length of 3.6μm, a capacitance of 220 fF and resistance of 100Ω, this device has a speed of 42GHz at a 6 dB modulation depth and consumes about 1pJ/ bit of energy.</u>

While the all-oxide modulator is one way of implementing the plasmon assisted design approach, one other way is utilizing a ring resonator. Designs related to this have been simulated in the following section.

3.3. Polymer based EO Modulator (Tier 2 Speed)

Modulators can be thought of as the bridge between electrical and optical signals in a photonic integrated circuit and could potentially be referred to as the single most important device. This is well recognized by the research community as evident from the sheer number of demonstrations of modulators, in the recent past. However, as evident from Figure 13(c), plasmonic modulators still exhibit large IL.

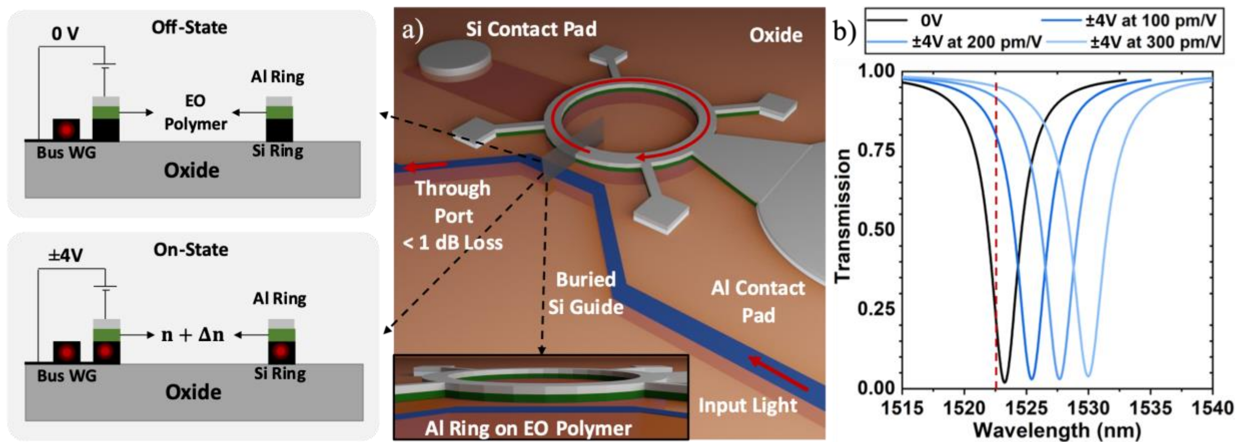

Figure 22: Schematic of the hybrid EO modulator design. The inset on the left shows the on- and off-states of the device. In the off state, the light bypasses the HPP ring due to destructive interference, while under a bias, the index of the EO polymer increases due to the Pockel's effect and the light couples into the plasmonic section where it is absorbed. b) Plot of the transmission spectra in the off-state versus on-state (black curve) which illustrates the strong modulation depth and low insertion loss of the device

The device (Figure 21) consists of a bus waveguide connected to an hybrid photonic-plasmonic (HPP) ring. The dielectric region of the HPP consists of an electro-optic (EO) polymer. EO

polymers have been used quite successfully in nanophotonic devices [36,62], as they provide large index change upon application of an electric field, based on the Pockel's effect, while introducing negligible losses. In this case, after polling the polymer, an applied bias in-duces an index shift in the polymer which alters the mode index of the light in the ring, shifting the resonance condition (Figure 22). When the device is biased to bring the ring is in resonance with the incoming light (on-state), light is critically coupled to the ring where it is absorbed by the Al forming the top layer of the ring. When the device is unbiased (off-state), light destructively interferes in the ring and exits at the through port with minimal IL. While there are numerous EO polymers available, with r_{33} coefficients as high as 350 pm/V,41 the current device design is conservatively based on Disperse Red 1 [N-Ethyl-N(2-Hydroxyethyl)-4-(4-Nitrophenylazo)Aniline], available from Sigma Aldrich. This can be dispersed in PMMA and has been shown to exhibit an r33 co- efficient of about ~100 pm/V [63].

For a device geometry with a 2 µm ring radius, 340 nm Si thickness, and 60 nm gap filled with an EO polymer of index 1.49 (PMMA), a critically coupled resonance is found [using a 3D FEM solver, COMSOL] at a wavelength of 1523 nm with a FWHM of 2.9 nm, see Figure 22(b). After being polled, the application of an 8 V differential bias (within the ±5 V of CMOS) between the Al and Si ring generates a ~0.022 index change, producing a 2.2 nm resonance shift. Most importantly, the device achieves an ER of 9 dB with a low insertion loss of 1 dB using the conservative r_{33} coefficient. Moving to a state-of-the-art EO polymer, with r_{33} coefficients of 300 pm/V and beyond has the potential to reduce the IL down to 0.2 dB, as shown in Figure 22(b).

Moving to a "Plasmon-Assisted" HPP configuration, we can potentially achieve an IL as low as 0.2 dB (lowest reported for plasmonics) with 9 dB modulation,

energy consumption of 23 fJ/bit, speed of 700 GHz (Tier 2), in an active area of 12 μm^2.

3.4. NOEM Dynamic Polarization Rotator (Tier 1 Speed)

As discussed in the previous section, plasmonic devices have usually resulted in larger insertion losses than their photonic counterparts. This is predominantly due to the large ohmic losses coupled with plasmons being more sensitive to fabrication imperfections such as surface roughness, oxidation and dimensional mismatches. Amongst several methods attempted by researchers, to reduce ohmic losses, one widely used method has been to adopt a hybrid plasmonic-photonic (HPP) waveguide configuration. While HPP's have been well studied in literature, designs have almost exclusively been filled with low index materials.

In this section of thesis, the proposed geometry replaces the low-index solid material with air, consisting of a Si ridge waveguide with a metal cap and nanoscale air spacer. We select Al as the metal of choice, due to its wide range of excellent properties including: respectable plasmonic performance in the near-infrared (ε'/ε" ~ 6) enabling propagation lengths of 10 μm – 800 μm (attenuation of 0.6 and 0.007 dB/μm, respectively) see Figure 23(a); combination of low-density (2.7 g/cm^3) and moderate Young's modulus (70 GPa) that allow high mechanical resonant frequencies and low energy actuation compared to soft/heavy metals; and CMOS-compatibility with low-cost, thereby enabling ready co-integration with electronics. The resonant frequency of a cantilever is given by the formula, $f = 1/2\pi(\sqrt{k/m})$, where k is the spring constant and m is the effective mass. The spring constant is further approximated by, $k = Ewt^3/4l^3$, where E is the Youngs Modulus, w is the width, t is the thickness and l is the length. The effective mass is given by the equation, $m = At\rho/4$, where A is the area, t is the thickness and ρ is the density. From this

set of equations, one can see that the frequency increases as the spring constant increases and effective mass decreases. In this sense, a material with a higher Young's Modulus and low density is beneficial to achieving higher frequencies of operation. However, the force needed for x deflection is linearly proportional to the spring constant. Thus, there exists a trade-off between energy efficiency and speed as the spring constant increases. However, a decrease in density leads to higher speeds and lower energy consumption. In this sense, Al is the preferred choice over materials such as gold, silver, and TiN.

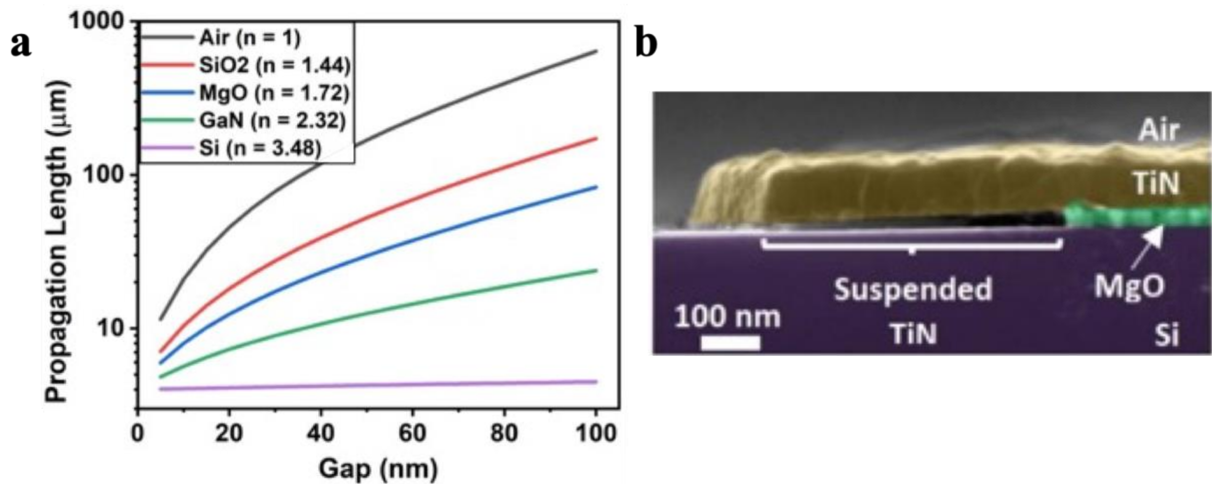

Figure 23: (a) Propagation lengths of Al-Si hybrid waveguides with various low-index materials, (b) Example of sacrificial under etch of TiN on Si using MgO in extremely dilute phosphoric acid

The most important aspect of the proposed design is the large reduction in propagation loss of the structure, wherein the airgap HPP waveguide achieves a performance similar to gold/silver HPP guides filled with silica (~0.01 dB/μm). Since Al is a more lossy metal than gold/silver, this is accomplished by reducing the plasmonic interaction. In this case, it is a direct consequence of the increased index contrast between Si and air and is achieved without substantial enlargement of the mode as in prior works. This of course, leads to a challenge as it reduces our ability to modulate –

obeying the loss-confinement trade-off. However, this is overcome by adopting the air-gap structure along with the “Plasmon-Assisted” design approach. Using this general design approach, the present and following sections proposes 3 devices which are tailored for, both, low and high frequency modulation, routing and polarization switching. In this section, we focus on the polarization rotation-based switch.

As photonic integrated circuits become more complex, on-chip polarization control increases in importance, as a single circuit could contain devices that are designed to operate with either TE or TM polarized light. For example, plasmonic elements generally utilize TM modes (H-field parallel to the substrate) while in photonic elements a TE mode is more widely used, due to the higher grating coupling efficiency and wider mode control by varying waveguide width. Current polarization controllers are either fiber-based stress-strain devices, which are bulky and typically not integrated on a chip or lithium niobate ~~LNB~~ based waveguides which are 100’s of um long, resulting in challenging integration in densely packed photonic circuits. In this sense, a compact dynamic on-chip polarization control would enable a host of new functionality including an additional degree of freedom to increase signal modulation bandwidth, enable dynamic signal multiplexing, facilitate new approaches to routing signals, and allow the selective activation of photonic/plasmonic elements. While several device designs have been proposed to enable static polarization control, dynamic polarization control on-chip remains elusive.

To address this limitation, we propose a “Plasmon-Assisted” dynamic polarization rotator that achieves speeds of up to 5.8 MHz (Tier 1), with IL <0.65 dB, in an area of ~6 μm^2 with a 200 aJ/bit energy consumption, enabled by mechanical modulation of the low loss airgap HPP waveguide.

To illustrate the operating principle, we first consider the mode indices for the three modes (TE, TM, and HPP) in the hybrid air-gap waveguide versus waveguide width assuming a 30 nm air gap (Fig. 24). At a width of 400 nm, the mode index of the HPP mode perfectly matches the TE polarized mode, enabling efficient coupling, while the TE and TM modes are mismatched. To begin the mode conversion, an adiabatic taper is introduced by gradually overlapping the metal cap with the silicon waveguide, see Figure 25. As the metal becomes centered over the Si waveguide, the polarization of the mode is gradually rotated from a horizontal TE mode to vertical TM mode by the HPP guide. This transition is efficient since the mode index is nearly constant throughout the entire rotation process. Once rotated, the mode is converted from the TM polarized HPP into a photonic mode through a symmetric taper which gradually lowers the index to match the TM mode in the Si guide. On the other hand, increasing the air gap to 80 nm decreases the mode index of the hybrid mode by 0.1 (Figure 25), precluding it from coupling to the TE mode and eliminating the rotation effect. This can be seen in Figure 25 (insets, 80 nm gap condition) where no coupling to the hybrid mode is observed despite the presence of the metal cap – achieving a "Plasmon-Assisted" operation.

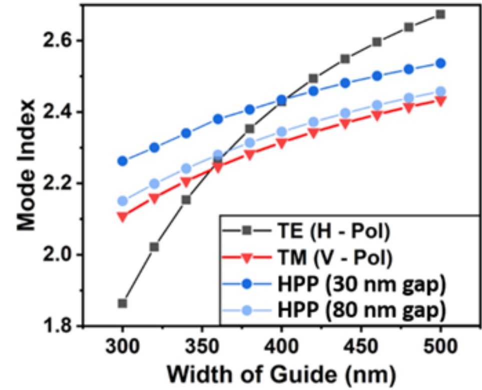

Figure 24: Effective mode index of TE, TM and Hybrid (HPP) mode of hybrid air-gap waveguide (gap size: 30 nm and 80 nm) plotted as a function of the width of the Si waveguide.

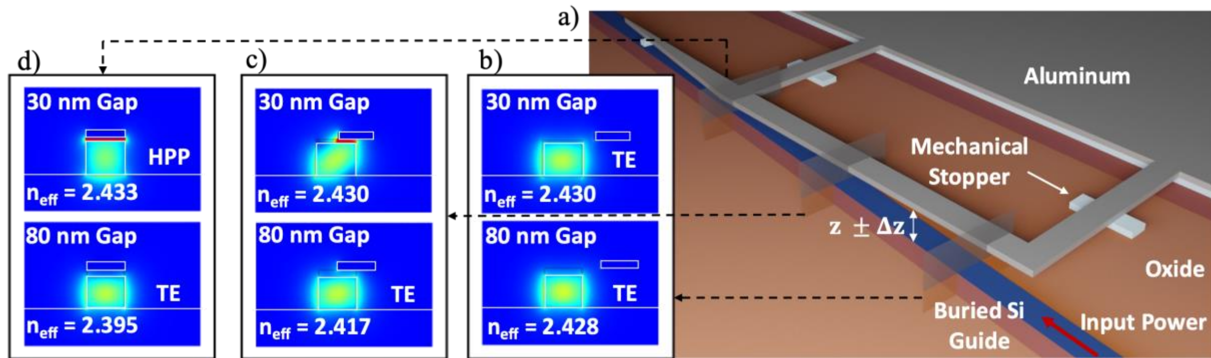

Figure 25: (a) Schematic of the proposed dynamic polarization rotator, which includes a Si waveguide with a suspended Al cantilever and stopper layers to limit pull-in. (b), (c) and (d) Normalized electric field mode profiles for a 30 nm and an 80 nm gap and various distances along the structure. When the gap is 30 nm, the mode adiabatically transfers from TE (horizontal) to a HPP (vertical) mode. In the case of an 80 nm gap, the two modes are sufficiently mis-matched to preclude efficient coupling within the device length

To estimate the device performance, an Al cantilever of 400 nm width and 55 nm thickness overlapping with a Si waveguide of 400 nm width and 340 nm thickness is simulated using 3D finite element method (FEM) mechanical simulations, where a 5.8 MHz mechanical resonance is found. Actuation is achieved by placing a bias between the Al and Si which induces an electrostatic force that deflects the cantilever and reduces the gap height to initiate the rotation. Simulations show that the 50 nm displacement can be achieved by applying a bias of 1.8 V. To ensure minimal reflective losses, the rotator is conservatively taken to be 15 μm long (more than 10× the effective wavelength for each taper) to achieve adiabatic evolution. As a result, the rotator achieves an IL of <0.65 dB (determined by the propagation loss of HPP mode, over the device length). The IL can be reduced further by altering the width of the Si guide during the asymmetric taper and removing the final symmetric Al taper, thereby cutting the plasmonic length in half. It is also important to note that a deflection of only 35 nm is sufficient to produce a 0.05 change in mode

index and decouple the hybrid and TE modes, thereby reducing the required voltage and IL. Further optimization of the device is expected to reduce these values even more.

Naturally, with the large relative motion mentioned (~60% of air-gap), runaway actuation due to the increasing electrostatic force with decreasing gap (known as pull-in) and breakdown of the nanoscale gap are concerns. Typically, pull-in limits actuation to around 1/3rd of the initial gap size (as documented in MEMs and NEMs) [64]. Here, we overcome this limitation by embracing pull-in (applying 1.8 V when pull-in bias is 1.7 V), and in turn, restricting cantilever motion by introducing a stopper that limits motion to the necessary 30 nm gap (Figure 265). Once the bias is removed, the actuator returns to its original position due to the restoring force of the cantilever (33 nN in this case) which is sufficient to overcome Van der Waal's forces that are minimized in our case due to the very small contact area [65,66]. A reliability of over 10^{14} switching cycles is estimated from prior works, limited by contact welding, and is sufficient for over 10-years of operation at 100 MHz with a 1% duty cycle [65]. Additionally, breakdown is avoided, as the peak electric field of 60 MV/m (1.8 V over 30 nm) is less than that sub-micron breakdown strength of air (>75 MV/m) [67].

3.5. NOEM Dynamic Switch (Tier 1 Speed)

Electrically programmable switches are an important part of PICs. They form the backbone of modern data centers and are the foundation of programmable photonic circuits [68–70]. However, low off-state losses are absolutely essential, as in a multi-port router the signal must pass through numerous devices before being routed. Thus, losses above 0.5 dB are essentially intolerable, a tough measure for plasmonics. Thus, nearly all switches in literature rely upon purely dielectric structures to route light, leading to devices occupying large areas device of 100's to 1,000's of

square microns, that are relatively slow (generally sub-MHz operation), and that require large drive voltages (>10 V), see Figure 13(c).

<u>Here we show that moving to an HPP "Plasmon-Assisted" approach enables the realization of a switch with 0.08 dB (through port) and 1.8 dB (drop port) IL, 6.8 MHz (Tier 2) operation, a record low 60 aJ/ bit energy consumption, in a size of just 36 μm^2.</u>

Moreover, this approach achieves better performance than the recently demonstrated hybrid plasmon switch using gold [38] and does so while achieving CMOS-compatibility. Hence, the device can increase the density of switching networks by over 100×, enabling new ultra-dense network routing and field-programmable optical logic.

The proposed device consists of two Si bus waveguides coupled to an airgap HPP ring formed by an Al membrane freely suspended over a Si ring (Figure 26). In this structure, the ring's optical resonance condition is dictated by the nanometer scale air gap in between Si and Al. Similar to the polarization rotator, applying a bias creates electrostatic forces between Al and Si that deflect the Al membrane causing an enhanced plasmonic interaction that increases the mode index, and shifts the resonance. When actuated (on-state, Figure 26), the ring is shifted to be in resonance with the incoming signal where light then passes through the HPP ring and couples to the drop port, providing switching. When unbiased, light destructively interferences in the ring, providing an output at the through port. Moreover, this destructive interference precludes light from interacting with the plasmonic element ("Plasmon-Assisted" operation), enabling exceptionally low through-port IL.

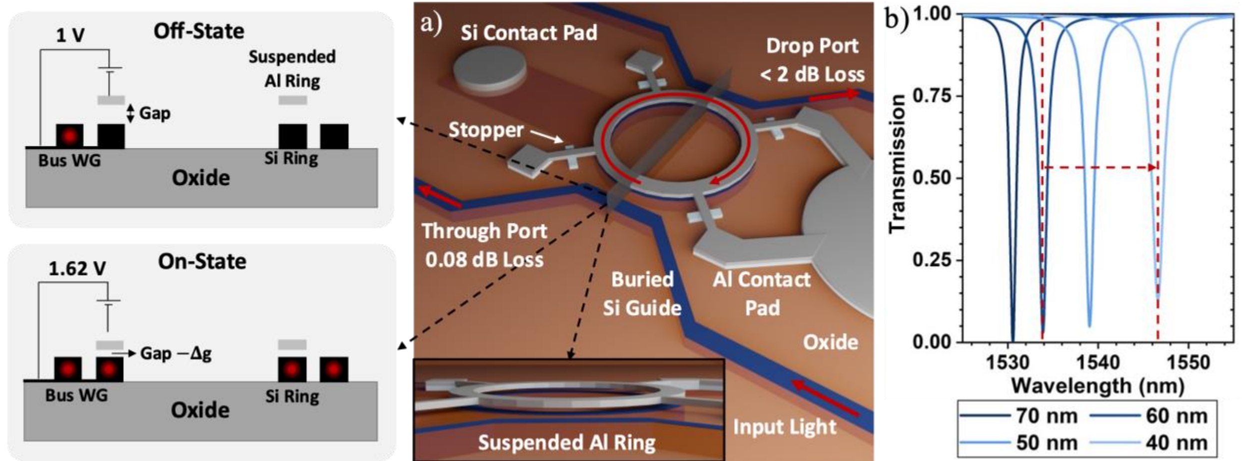

Figure 26: a) Schematic of the proposed hybrid "Plasmon-Assisted" dynamic NOEM switch, consisting of an Al ring suspended over a silicon ring, which is coupled to two bus waveguides. Inset on the left depicts the operation of the switch in the on- and off-state where switching is achieved through a shift in resonance induced by electro-static deflection of the Al ring. b) Transmission spectra at the through port, obtained from 3D simulations of a single bus waveguide coupled to a hybrid ring resonator with a 70, 60, 50 and 40 nm gap; a FWHM between 0.9 to 1.2 nm is obtained. With a 20 nm deflection, shown by the dashed lines in the figure, the resonance wavelength shifts by 13 times the FWHM, providing high contrast switching.

3D FEM optical simulations of the HPP ring structure with a radius of 2 µm and a 60 nm air gap coupled to a single bus waveguide show a resonance 1533 nm with a FWHM of 0.9 nm when at the critical coupling condition – where round trip loss equals the input energy from bus waveguide (Figure 26). A 20 nm decrease in the air gap is sufficient to shift the resonance by 13 nm, which results in over 20 dB extinction ratio at the through port, along with sub 0.02 dB IL due to the "Plasmon-Assisted" operation. Adding a second waveguide (drop port) has been shown in literature to broaden the FWHM by 2.5 times, thus conservatively increasing the IL at the through port to 0.08 dB. Drop port losses are estimated to be 1.8 dB based on the ratio of the through and drop port losses when compared to other switches in literature. This level of loss is tolerable in the

drop port as in typical routing fabrics, only a single drop port route is required. Thus, a signal can pass through 15 HPP switches, including one route operation, before reaching 3 dB total IL. Mechanically, for an Al layer thickness of 75 nm, a ring radius of 2 μm, a ring width of 400 nm, and a support length of 3 μm, 3D FEM simulations show a resonance frequency of 6.8 MHz for the Al membrane The actuation mechanism is similar to that of the polarization router, in that the necessary 20 nm of deflection is achieved through electrostatic deflection by modulating the bias from 1 V to 1.62 V (620 mV actuation), a value that is just above the pull-in voltage (1.6 V) for which motion is limited by the stopper. Again, our restoring force (33 nN) combined with a minimal stopper area is sufficient to overcome Van der Waal's forces and enable the actuator to return to its original position. Furthermore, an applied voltage of 1.62 V across a 40 nm air gap yields a field (40 MV/m) that is well-below the breakdown strength of sub-micron airgaps (75 MV/m). Similar to the polarization rotator, a reliability of over 10^{14} switching cycles, limited by contact welding, is estimated. While the stress in the metal cantilever in these device designs is well below the yield strength, the risk of creep exists. Creep is the tendency of a solid material to move slowly or deform permanently under the influence of persistent mechanical stresses. It can occur because of long-term exposure to high levels of stress that are still below the yield strength of the material. However, creep is more severe in materials that are subjected to heat for long periods and generally increases as they near their melting point, so while the risk is minimal in the proposed device designs, it is an area of concern which requires further investigation.

3.6. Conclusion

In conclusion, four (two Tier 1 and two Tier 2) devices have been discussed in this chapter. Out of the two Tier 2 speed devices (bit-wise operation in GHz), one of them is a broadband all oxide EO modulator and the other is a narrow bandwidth, high-Q ring based EO modulator. For the ring-based design we make use of the versatility of an air-gap hybrid waveguide structure and backfill the gap with an electro-optic polymer [71–73]. Although resonator structures are well explored, photonic devices generally employ high Q's (more than 2,000) due to the low modulation capability of Si [74,75], which limits the speed of the device. Alternatively, plasmonic resonant devices operate with extremely low Q cavities (due to the high loss) which require exceptionally large tuning (~10-20 nm shift) to achieve modulation. Here we find the "sweet spot" between the trades-offs of cavity-limited speed, RC limited speed, and resonance width, realizing a moderate Q-factor of ~600 (Si guide W: 400 nm, H:340 nm; airgap: 60 nm; radius: 2 μm). In this case, the HPP resonator introduces just enough plasmonic interaction to enable > 1 THz speed for both cavity (through an increase in loss) and RC limits (through reduced size), all while maintaining a full-width-half-max of the resonance within the modulation range of commercial nonlinear polymers under CMOS voltages, (~2 nm), allowing complete de-coupling of the HPP cavity to achieve a sub 1 dB IL. On the other hand, the truly broadband all oxide EO modulator completely shuns the use of metals and relies upon the switching of an ENZ material between metallic and dielectric states. The non-resonant slot waveguide structure also results in a comparatively small footprint.

At the other end of the spectrum, the Tier 1 devices operate on internet packets which change at a rate of ~1.6 MHz (>1,500 bits per packet, line speed of 20 GBaud40). In this we employ a hybrid-

plasmon-coupled mechanical actuation. In the active on-state of the device, we deflect the Al layer to reduce the gap size which increases the plasmonic interaction and improves our ability to dynamically control the mode – but we do so only when it is necessary. In the passive off-state, the plasmonic material is far enough away to not generate exceptional IL, (thereby motivating the choice the low loss devices we undertake to implement in the following chapter, the fields in the air-gap region vary rapidly in space, such that movement of the Al by 10's nm is enough to drastically change the mode properties.

Our proposed devices achieve exceptionally high optomechanical coupling coefficients >1,000 GHz/nm (sensitivity of the device to mechanical motion), more than 100× photonics, and enabling nanometer displacement with sub 2 V drive.

Another approach to overcome the reduced LMI of the airgap HPP guide is through the use of a resonator structure. For Tier 1 speed devices, the Q-factor provided by a ring resonator (~100 – 2,000 for airgaps of 10-100 nm) further enhances the sensitivity of the structure to mechanical deformation, increasing our ability to achieve high contrast dynamic functions without concern for cavity lifetime limited speed.

[This chapter contains results that have been previously published:

1. *Md. Sojib, D. Fomra, V. Avrutin, N. Kinsey, "Optimizing epsilon-near-zero based Plasmon Assisted Modulators Through Surface to Volume Ratio", vol. 30, issue 11, pp. 19781-19794, Optics Express, 2022*
2. *R. Secondo, D. Fomra, N. Izyumskaya, V. Avrutin, J. Hilfiker, A. Martin, U. Ozgur, and N. Kinsey, "Reliable Modeling of Ultrathin Alternative Plasmonic Materials Using Spectroscopic*

Ellipsometry," Optical Materials Express – Beyond Thin Films: Photonics with Ultra-thin and Atomically-thin Materials Feature Issue, vol. 9, no. 2, 2019 [Invited]]

4. DEVICE FABRICATION OF ALL-OXIDE MODULATOR

A photonic integrated circuit consists of components such as phase shifters, polarization controllers, routers and modulators. A few of these were discussed in the previous section. However, out of these, the capability to encode the incoming electrical signal onto an optical pulse is critical to the co-existence of optics with electronics. In this sense, we focus the fabrication effort on the EO modulator. Of the two EO modulators proposed, All-oxide EO modulator and the polymer based EO modulator, the former is investigated due to the ready availability of the materials needed to fabricate the device. The following section discusses the materials optimization studies and the fabrication details.

4.1. All Oxide EO Modulator – Material Deposition

4.1.1. Aluminum Zinc Oxide

A potential and promising choice of active material for the All-oxide modulator is aluminum-doped zinc oxide (Al:ZnO or AZO), which is a type of a transparent conducting oxide (TCO) [76]. These are a class of materials that exhibit near zero index (NZI) properties at telecommunication wavelengths. These materials are particularly attractive as they offer large tunability under both electrical and optical control, offer sub-picosecond response times, and are of purely solid-state nature. Apart from providing excellent tunability, NZI materials also exhibit enhanced light-matter interaction (LMI), due to slow light effects, enabling more compact and energy-efficient meta devices. As a result, NZI materials have been shown to enhance a number of nonlinear optical processes (such as adiabatic frequency shifts, second and third harmonic generation, and four-

wave mixing), and have led to the realization of sub-micron modulators [77] and high angle beam steers [34], making the development of these materials a key for several areas of dynamic nanophotonics. Among a wide range of transparent conducting oxides, aluminum- and gallium-doped zinc oxide are particularly attractive, as ZnO is a well-studied material system that accepts high levels of doping, has high conductivity, has well-established fabrication processes, and its elements are abundant in nature [78–80]. Thus far, a variety of techniques, including sputtering [81], molecular beam epitaxy (MBE) [82], pulsed laser deposition (PLD) [83], atomic layer deposition (ALD) [84,85], etc., have been utilized to deposit doped ZnO. Among these methods, ALD provides advantages such as conformal, pin-hole free, and low-temperature deposition with sub-nanometer thickness control along with being a CMOS compatible and scalable method [86]. However, the ALD route/process has so far resulted in Al- and Ga-doped ZnO films with high losses and insufficient carrier concentration to obtain NZI properties covering the entire telecommunication wavelength range (1260 nm to 1665 nm) or provide access to biological transparency windows (600 nm to 1350 nm) [87–89].

The lower quality of the ZnO-based TCO films produced by ALD using water as an oxygen precursor, compared to those grown by the sputtering and MBE methods, can be traced back to the digital nature of the ALD process. In the ALD regime, concurrent delivery of abundant Al and Zn species to the substrate which saturate the available surface sites favors Al_2O_3 growth due to the higher adsorption energy of the most widely used Al precursor, trimethyl aluminum TMA, compared to Zn precursor diethyl zinc, DEZ, on OH^- terminated surfaces [90,91]. Therefore, the conventional ALD route to deposit Al:ZnO ~~(AZO)~~, involves alternating two steps: 1) a combination of zinc and oxygen precursor pulses followed by 2) a doping cycle of aluminum and

oxygen precursor pulses. Intuitively, this leads to the incorporation of AlO_x layers sandwiched between ZnO layers. To form AZO, this process relies upon the subsequent diffusion of Al into ZnO, but the digital nature inherently results in non-uniform Al distribution along the growth direction [89]. Consequently, the doping efficiency, also frequently referred as dopant ionization efficiency, for these films (ratio of electron concentration to total Al content in the matrix,) is as low as 10% to 15%, and the excessive Al species form alumina inclusions in the matrix. In contrast to this conventional ALD approach, many other deposition methods (MBE, PLD, sputtering) involve concurrent delivery of Zn and Al species with precisely controlled flux ratios within a very wide range which gives rise to more uniform Al or Ga distribution through the matrix and achieves doping efficiencies exceeding 85% at high (>10^{20} cm^{-3}) doping levels [92].

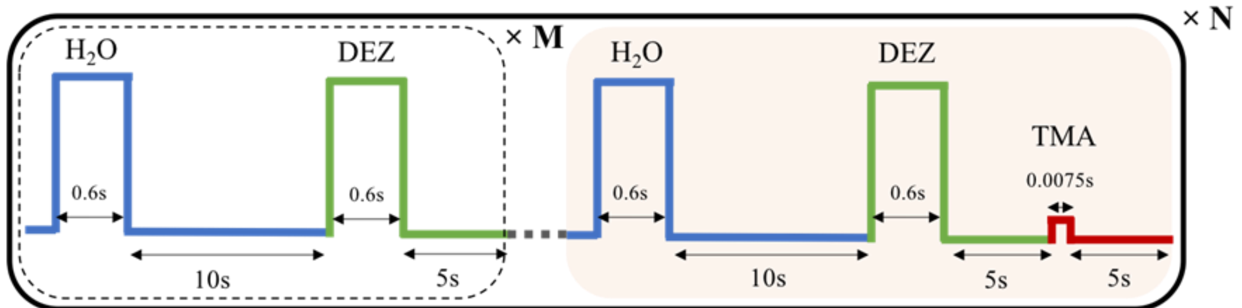

Figure 27: Schematic of the pulse sequence in the modified ALD process. 'M' alternating pulses of H2O and Diethyl Zinc (DEZ) are followed by a doping cycle of H_2O, DEZ, and Trimethyl Aluminum (TMA). The frequency of the doping cycle determines the carrier concentration and 'N' number of super-cycles determine the thickness [68]

To address the limitation of digital ALD growth for heavily doped TCO's, we have investigated a modified approach to the ALD growth of AZO thin films on silicon and sapphire substrates. The approach moves away from the surface saturation condition of ALD for the Al precursor pulse, which leads to a reduced Al incorporation in each dosing cycle in favor of more frequent pulses.

This process produces a more uniform distribution of the dopant along with reduced clustering of the excessive Al species that result in alumina inclusions. As a result, the AZO produced through the modified process provides tailorability of the NZI region across the entire telecommunication range while maintaining low optical losses: crossover wavelengths as low as 1320 nm on sapphire and 1370 nm on silicon with losses of 0.45 and 0.35, respectively. The short crossover wavelength coupled with low losses, reinforced by the advantages of the ALD method, makes these films extremely attractive for a range of dynamic nanophotonic meta devices.

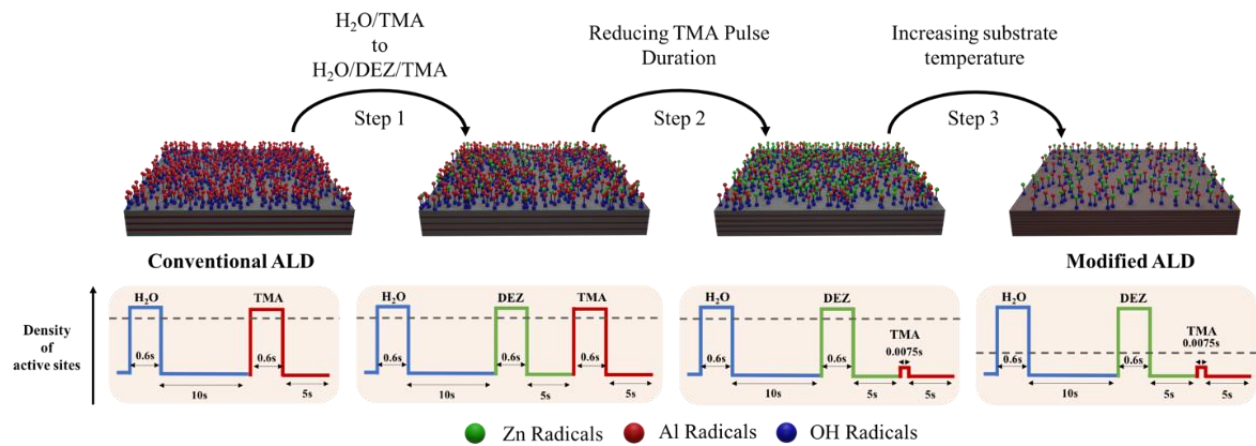

Figure 28: Schematic of modifications made to the doping the cycle, as the ALD process moves from the conventional to the modified regime. The dashed grey line in the pulse train schematic denotes the density of active surface sites. The conventional doping cycle includes H_2O and TMA pulses under surface saturation conditions leading to a very high Al incorporation. Step 1: introducing a DEZ pulse in between H_2O and TMA pulses leads to a mixture of Zn and Al radicals in the doping layer, thus reducing Al incorporation compared to the original doping cycle. Step 2: further reducing the TMA pulse duration limits the amount of TMA supplied, thus further reducing Al incorporation. Step 3: lastly, higher substrate temperature reduces the density of active sites (number of hydroxyl groups), thus reducing Al and Zn incorporation in each cycle. Ultimately, the reduction in the Al incorporation per cycle enables a more frequent occurrence of the doping cycle, thus producing more even and effective doping of the ZnO film [68]

The modified ALD pulse train is shown in Figure 27, where each super-cycle consists of 'M' number of alternating pulses of Diethyl Zinc (DEZ) and H_2O, followed by a doping cycle of DEZ,

Trimethyl Aluminum (TMA), and H_2O. The overall number of super-cycles 'N' is varied to control the film thickness and the frequency of the doping cycle controls the free carrier density. The detailed description of the growth conditions can be found in the methods section. Central to the modified ALD mechanism is the divergence from the surface saturation condition of the Al precursor. This decreases the incorporation of Al ions in each dosing cycle, enabling an increase in the frequency of doping cycles, a more uniform Al distribution throughout the film, and an increase in the Al doping efficiency while reducing electron scattering as it decreases the formation of alumina inclusions. This is achieved by utilizing H_2O/DEZ/TMA pulse sequence (Step 1 in Figure 28) [87,93], reducing the amount of Al precursor supplied in each pulse to decrease surface coverage of TMA (Step 2 in Figure 28) [94] along with increasing the substrate temperature to lower the density of OH^- groups on the surface, which act as active sites (Step 3 in Figure 28).

The first step in realizing improved AZO consisted of adopting a blended H_2O/DEZ/TMA pulsing sequence for the doping cycle, as opposed to the H_2O/TMA conventionally used in ALD. While the conventional pulsing sequence leads only to Al-O bonds, the modified pulsing sequence promotes competition between Zn-O and Al-O bonds during the dopant cycle. The introduction of DEZ into the reaction chamber (before TMA) leads to the formation of Zn-OH bonds but as the adsorption energy of TMA-OH (1.16 eV) is larger than that of DEZ-OH (0.74 eV), TMA is capable of randomly replacing adsorbed DEZ [90,91]. This decreases the amount of Al species incorporated into the film, as the active sites are now shared between Al and Zn ions. Thus, the reduced incorporation of Al species in each dosing cycle provides better doping control, as opposed to the conventional ALD sequence of H_2O/TMA that leads to the incorporation of an Al monolayer (Step 1 in Figure 28).

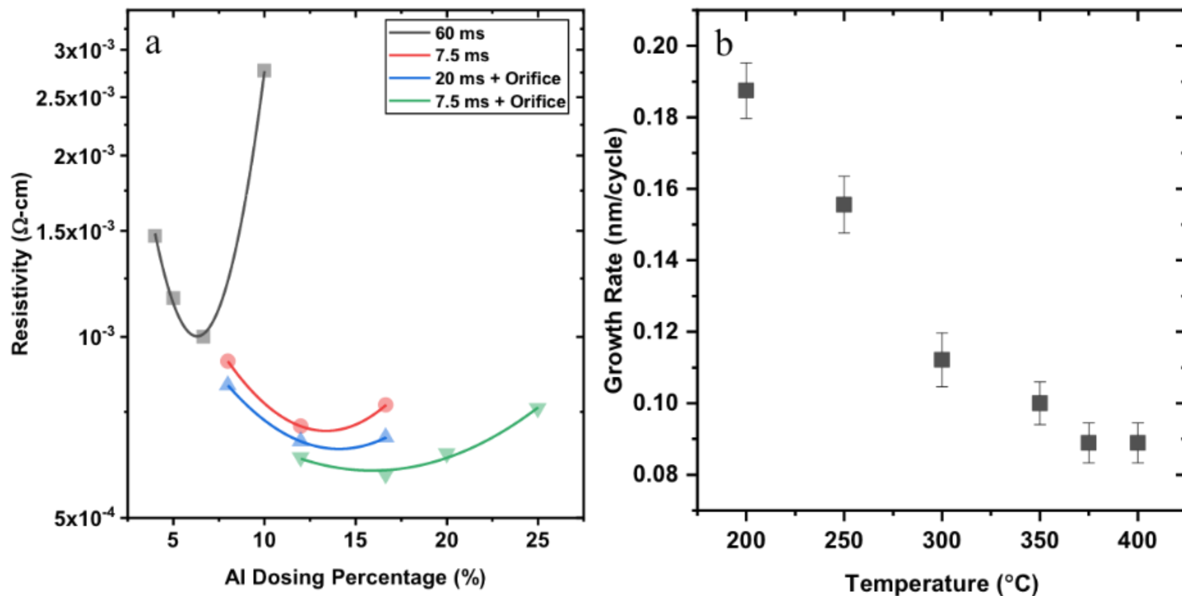

Figure 29: (a) Plot of resistivity versus Al dosing percentage at different TMA pulse durations, of AZO deposited on a sapphire substrate at a substrate temperature of 250°C. With reduced pulse duration, the optimum dosing percentage shifts to higher values due to the reduced Al incorporation in each dosing cycle. (b) A plot of growth rate versus deposition temperature. The reduction in growth rate occurs because of the evaporation of the H2O at elevated temperatures that reduces the number of active sites available with which Zn or Al radicals may bond [68]

Conventionally, in the ALD deposition of AZO, an increase in the dosing percentage (ratio of H_2O/DEZ/TMA pulses to H_2O/DEZ pulses) reduces the resistivity, up to an optimum point. Increasing the dosing percentage further results in an increase in resistivity due to the clustering of the excessive Al in the matrix [95]. Under surface saturation conditions, with an Al pulse duration of 60 ms, the optimum dosing (corresponding to the lowest resistivity) was 6% in our reactor, which is in agreement with commonly reported values of 3% to 6% (Figure 29(a)) [84,87,91]. To avoid the surface saturation with TMA, we reduced the TMA pulse duration from 60 ms to 7.5 ms (Step 2 in Figure 28), which was the system limit. To further reduce the amount of Al entering the chamber in each pulse and thus the amount adsorbed on the surface, our second optimization step was to install a 100-micron diameter orifice on the head of the precursor

bottle. In this case, the Langmuir exposure of TMA, the parameter describing the surface coverage of a precursor gas, reduces from 17×10^{-3} Torr at 60 ms to 0.6×10^{-3} Torr at 7.5 ms with an orifice, thus resulting in a higher optimal dosing percentage of 17%, as shown in Figure 29(a).

Finally, we increased the substrate temperature while utilizing the H_2O/DEZ/TMA sequence with a 7.5 ms pulse duration for the TMA+ orifice condition (the third optimization step). The increase in temperature further limits Al incorporation in each dosing cycle by reducing the number of surface-active sites (Step 3 in Figure 28). The decomposition of water molecules results in the absorption of OH^- radicals on the surface, which act as active sites for Zn^+ and Al^+ ions. At increased temperatures, the OH^- groups recombine to release H_2O and form O* radicals, thus reducing the number of active sites [89]. Therefore, the reduced growth rate of the material is believed to occur as a result of a decrease in the density of active surface sites, which in this case, is achieved by increasing the temperature, as shown in Figure 29(b). Under these conditions, the TMA adsorption is reduced, and the ALD is believed to be operating in a sub-saturation regime. The reduced adsorption of TMA leads to an increased incorporation efficiency of Al^+ ions, the effect of which can be observed in the decreasing resistivity trend (Figure 30(a)).

Figure 30(a), shows the resistivity of the AZO samples deposited on sapphire substrates with 20% Al dosing, at temperatures varying between 200°C and 400°C. More uniform Al^+ ion distribution through the matrix results in a decrease in resistivity from 8×10^{-4} Ω-cm at 200°C to 4×10^{-4} Ω-cm at 350°C. The reduced growth rate at higher temperatures not only gives rise to fewer Al ions being incorporated into the matrix during each dosing cycle but also leads to a more spatially frequent occurrence of the dopant layers due to reduced growth rate. For instance, the dopant layer occurs after every 1 nm of zinc oxide growth at 200°C, whereas it occurs after every 0.5 nm of

zinc oxide at 350°C albeit with a reduced number of Al species incorporated in each layer. The decrease in resistivity is predominantly the result of an increase in the charge carrier mobility with temperature up to 350°C, as the carrier concentration remains approximately constant (Figure 30(b) and (c)). This finding suggests a reduction in the clustering of Al ions, which decreases the density of scattering centers, thus contributing to an increase in mobility [94]. On the other hand, the increase in resistivity beyond 350°C is attributed to an increase in the decomposition of DEZ and TMA, known to occur at temperatures above 325°C, which leads to excessive impurity (carbon) incorporation [96,97]. While reliable Hall mobility data on the silicon substrate is challenging to obtain due to the parallel conduction channel, the optical mobility, extracted from the Drude model using the spectrometric ellipsometer is shown in Figure 30(d). It mirrors the trend observed on sapphire substrates, as the mobility doubles from 15 cm^2/ V-s to 29 cm^2/V-s when Ts increases from 200°C to 350°C. At higher temperatures, particularly above 375°C, we observed a drop in mobility only in films grown on silicon substrates. This could be attributed to a higher substrate surface temperature owing to the larger thermal conductivity of silicon as compared to sapphire. The small difference in surface temperature, particularly at temperatures near the precursor decomposition point, results in significantly different decomposition rates.

The tailorability of the crossover wavelength dictates the operating range of future dynamic meta-devices. To explore the extent of tailorability in the films grown under the optimized conditions (T_s =350°C, 7.5 ms TMA pulse duration with orifice and H_2O/DEZ/TMA dosing sequence), we varied the dopant dosing percentage between 2% and 33% and achieved a carrier concentration ranging from 2.5×10^{20} cm^{-3} to 8×10^{20} cm^{-3} (see Figure 31(a)). The highest carrier concentration was achieved for a dosing rate of 20% that translated to an ENZ wavelength of ~1400 nm on

sapphire and silicon substrates, for a ~45 nm thick AZO film (Figure 31(c) and (d)). Increasing the dosing percentage further gave rise to a decrease in free carrier concentration, presumably due to the formation of alumina inclusions. On the other hand, Hall mobility is observed to vary inversely with dosing percentage as it drops from 32 cm^2/V-s to 20 cm^2/V-s when the dosing percentage changes from 2% to 20% (Figure 31(b)). However, the optical losses remain sufficiently low (0.55 on sapphire and 0.45 on silicon), to maintain the near-zero index condition of these ultra-thin, ~45-nm thick films.

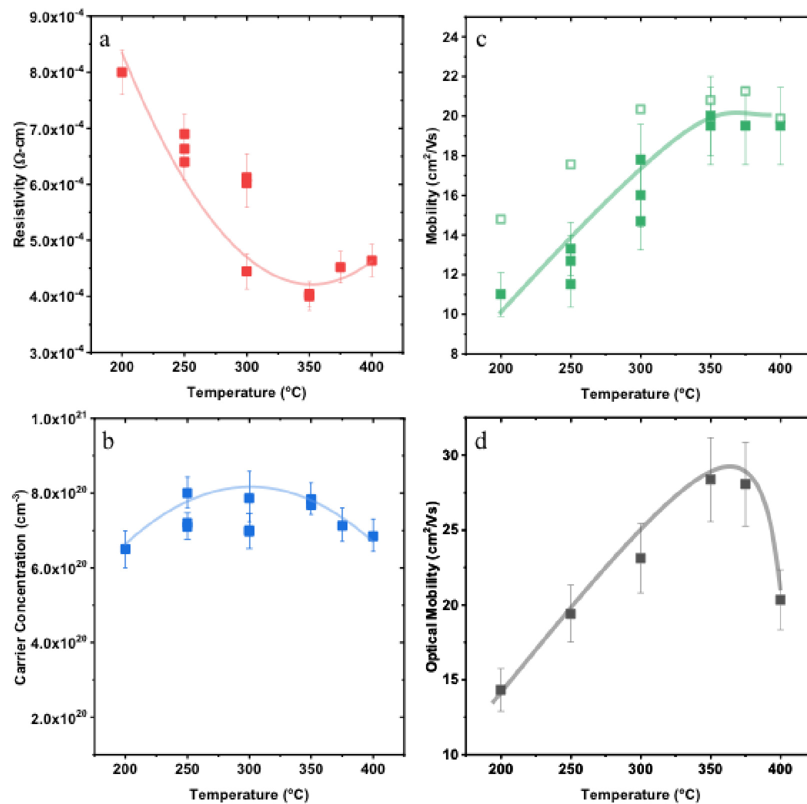

Figure 30: (a) Resistivity, (b) Carrier concentration and (c) Hall (solid squares) and Optical (Open Squares) mobility of ~ 45nm thick Al:ZnO films deposited on a sapphire substrate, at 20% Al dosing, as a function of deposition temperature. The drop in resistivity is largely attributed to the increase in the Hall mobility of these films, as the carrier concentration shows only a small change. (d) Optical mobility of Al:ZnO films deposited on silicon substrates under the same conditions [68]

Finally, the genesis of this enhancement of electrical and optical properties can be seen through the doping efficiency, expressed as $(N_{Al:ZnO} - N_{ZnO})/N_{Al}$ where, $N_{Al:ZnO}$, N_{ZnO}, and N_{Al} represent the density of free carriers in Al:ZnO, background (nominally undoped) carrier concentration, and density of Al atoms in the film, respectively. XPS analysis shows that the amount of Al incorporated in the ZnO thin films is 1.7%, producing a doping efficiency of 54%±1% using the modified ALD process compared to an efficiency of ∼13% reported in literature [95]. However, the use of higher deposition temperatures to reduce Al incorporation results in a lower structural quality of the Al:ZnO films as compared to those grown at 200°C, the conventional temperature for ZnO ALD, thus establishing a tradeoff. Nonetheless, the extent of improvement of optical properties is illustrated in Figure 32. Figure 32(a) shows the real and imaginary parts of the permittivity of our films (100 nm thick) grown under the optimized conditions on Si and sapphire substrates. Figure 32(b) compares the imaginary parts of the permittivity at the cross over wavelength for our films with ALD-deposited Al:ZnO and Ga:ZnO thin films reported in literature. As observed from the red points, the AZO films deposited in this work exhibit a significant improvement in the loss values over the values reported in literature [84,85,87–89], while exhibiting cross over wavelengths within the telecommunication O-band (1260 nm to 1360 nm). Furthermore, the 100 nm films with a resistivity of 2.8×10^{-4} Ω-cm are comparable to thick (700 nm – 900 nm) sputtered films, with a resistivity of 2.4×10^{-4} Ω-cm [98]. Lastly, the loss values of these ALD deposited films (ε’‘ = 0.35) are approaching and in certain cases even outperforming that of PLD (ε’‘ = 0.26) [43] and sputtered films (ε’‘ = 0.3 to 0.7) [81], while offering better

thickness control, which is advantageous for nanophotonic devices that typically require the use of sub-50 nm thin films.

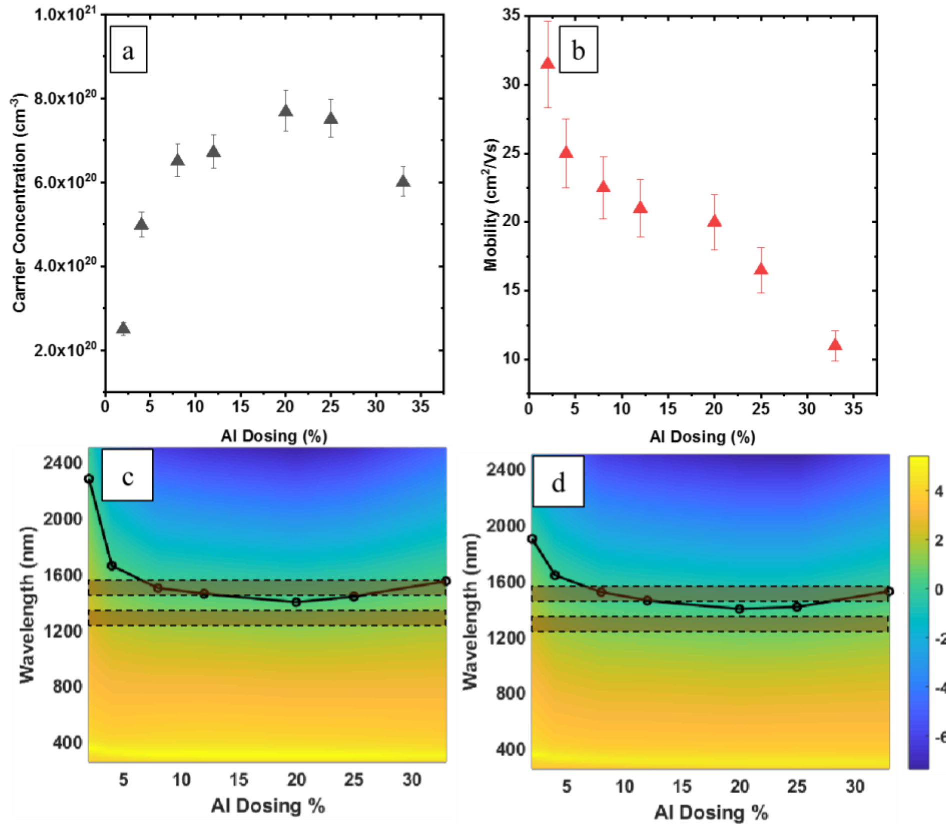

Figure 31: (a) Carrier concentration and (b) Hall mobility as a function of Al dosing percentage for ~45 nm thick films deposited on a sapphire substrate at 350°C, (c) and (d) Color map of the real part of permittivity, for films grown on sapphire and silicon substrates, plotted versus wavelength and Al dosing which shows the static tunability of optical properties of ~45 nm films on sapphire and Si grown under the optimized conditions of TS =350°C, 7.5 ms TMA pulse duration (with orifice) and H2O/ DEZ/ TMA dosing sequence. The symbol and the solid connecting lines denote the ENZ wavelengths of these films. The two highlighted regions mark the O and C bands of telecommunication [68]

The modified ALD mechanism, which includes moving away from surface saturation conditions for the dopant precursor, has resulted in an increased doping efficiency, from 13% to 54% including a more uniform doping profile. These attributes improved the optical and electrical

properties of the film significantly compared to prior works, with resistivity as low as 2.8×10−4 Ω-cm for a 100 nm thick film while maintaining uniform optical properties across large wafers. Moreover, the permittivity crossover was able to be statically tuned across the entire telecommunication spectrum and into the edge of the biological transparency window, thereby enabling the use of ALD deposited AZO in NZI-driven dynamic meta-devices. Further improvements are possible by reducing the purge times of TMA, DEZ, and H2O for processes involving Ts around 350°C, which is just above DEZ's and TMA's decomposition temperature. This can potentially address the trade-off between worsening crystal quality and improving doping efficiency, as a result of increased Ts. Moreover, the modified ALD process provides a pathway to improve the electrical and optical properties of other doped binary and ternary semiconductors such as doped gallium nitride, cadmium oxide, and gallium oxide, which are being explored for their large nonlinearities around the NZI region, occurring at technologically relevant wavelengths [99].

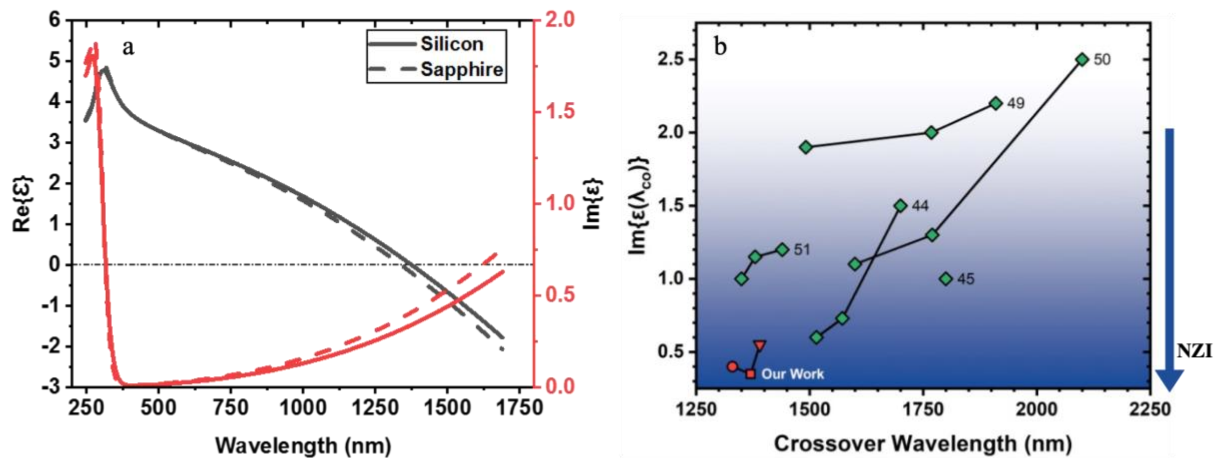

Figure 32: (a) real and imaginary part of permittivity for ~100nm thick films deposited on sapphire and silicon substrates at 350°C, with crossover wavelengths at 1330 and 1370 nm, respectively. (b) the imaginary permittivity of heavily doped (Al and Ga) ZnO films at the crossover wavelength. Moving to the modified ALD technique enhances doping efficiency thus enabling Al:ZnO films

with reduced losses and crossover wavelengths as low as 1330 nm. This enables the use of these films in integrated photonic devices, as the near-zero index properties are now accessible across most of the technologically relevant bands. The blue arrow and the shaded region on the plot denote the range of losses (ε" < 2) in which ENZ films exhibit NZI effects, such as slow light and wavelength expansion [23], emphasizing the need for low loss ENZ films. The red circle (~100nm film on sapphire), the red square (~100nm film on silicon), and the red triangle (45 nm film on sapphire) represent the Al:ZnO films grown under the optimized conditions [68]. Optical properties are estimated from Hall effect data using the Drude model, using a hyperbolic effective mass dispersion for ZnO for references that only reported electrical properties [52,52,55-57].

However, for the EO modulator, a low doped (~$1x10^{20}$ cm^{-3}) AZO film is needed, and counterintuitively, the low doped AZO exhibits a much higher loss in the NIR region. More discussion on this is in the following section.

4.1.2. Near IR Losses in Aluminum Zinc Oxide

While the losses in the highly doped films were low, and it is natural to expect the losses to be even lower in the case of low doped films, due to lower Drude contribution, that was not the case with ALD deposited AZO films.

Integral to the performance of the all-oxide modulator is the material quality of the active region, which in the present case is aluminum doped zinc oxide. More specifically, to obtain a high figure-of-merit (FOM), defined by the ratio of modulation depth to insertion loss, the active region should have as low of an optical loss as possible. In the previous section, we had demonstrated the deposition of high quality, low loss AZO on silicon and sapphire substrates (Figure 33). Ideally, in TCO's such as AZO, the loss in the near IR region is primarily due to the scattering of free electrons. Furthermore, as the carrier concentration decreases, the loss exhibited by the scattering of free electrons also decreases. However, for the films deposited by atomic layer deposition, this trend did not hold true. As the carrier concentration was decreased in order to shift the epsilon near

zero region further out into the IR, the loss in the near IR region (~1550 nm) increased (Figure 34). This proved to be an issue, as the higher-than-expected loss would lead to low off-state transmission of the all-oxide modulator.

Investigating the reason behind this counter-intuitive trend, ellipsometry measurements were conducted all the way down to 30,000 nm wavelength. This enabled us to analyze 5 samples with different doping concentrations to map out the trend of change in loss. It was found that in addition to the Drude loss there existed an additional contribution from either a defect state or a molecular vibration due to an impurity between 3 and 5 um. The presence of this feature can be readily observed in the S-Parameter of the ellipsometer measurement. The S-Parameter is a term derived

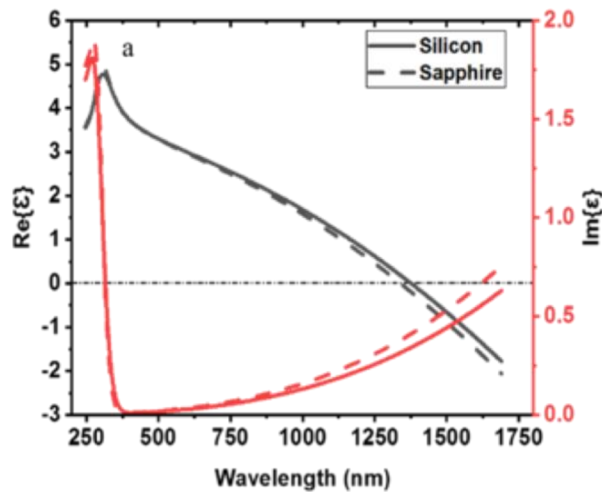

Figure 33: Real and imaginary parts of permittivity for ~100nm thick films deposited on sapphire and silicon substrates at 350°C, with crossover wavelengths at 1330 and 1370 nm, respectively.

from the sine and cosines of the Psi and Delta (ratio of r_p and r_s), which are direct measurements obtained from the ellipsometer. To extract useful insight, these curves are fit to a model. As any type of fitting leads to a certain degree of uncertainty, it is often beneficial to track the change in

the S-Parameter curves across samples to highlight changes. As shown in Figure 35, the curve indicated by 1 is the Drude contribution, while the feature indicted by 2 are the phononic contributions. The feature indicated by 3, which is especially pronounced for the case of AZO 2%, can only be fit using gaussian oscillators, which are usually indicative of absorption caused by either interband transitions, impurities or defects [100,101]. In the case of AZO, in the 3 to 5 um spectral range, literature suggests the presence of impurities which could lead to the broad absorption.

This is highly detrimental to the performance of the modulator, as this broad absorption found around 4 um has tails extending down to 1.5 um, the wavelength of interest. This tail not only increases the loss on the off state of the device, but also cannot be modulated dynamically, as this is not a free carrier driven effect. To overcome this issue, literature has shown that Indium Tin Oxide, another TCO which can be used in place of AZO, does not exhibit such a feature [102].

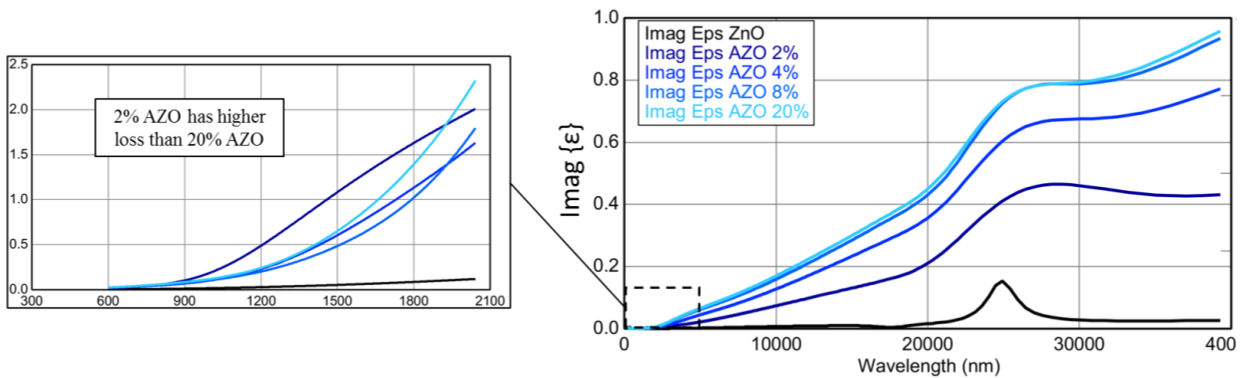

Figure 34: The imaginary permittivity, indicative of the loss in the films, is plotted as a function of wavelength (from 240 nm to 30,000 nm), for a set of AZO films deposited on silicon with ALD dosing percentage varying from 2% to 20%. Counter-intuitively, the loss in the lowest dosed films is higher than the loss in the higher dosed films.

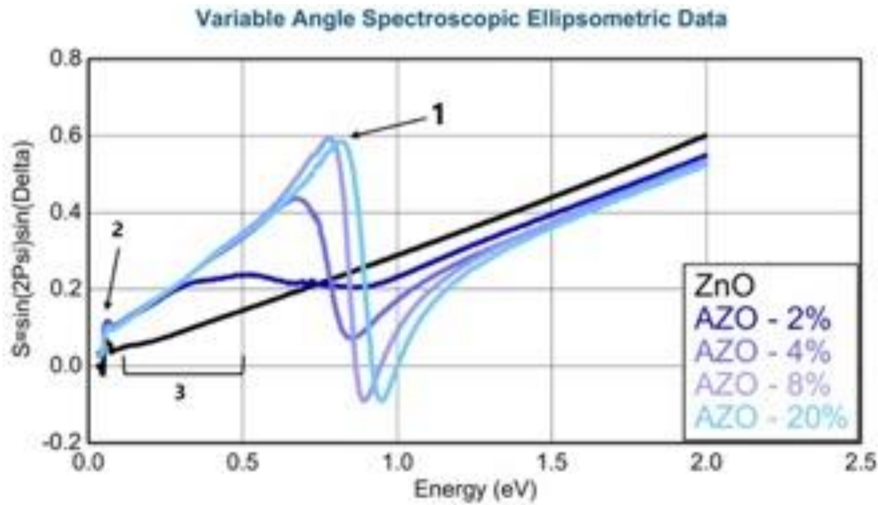

Figure 35: The curve indicated by 1 is the Drude contribution, while the features indicted by 2 are the phononic contributions. The feature indicated by 3, can only be fit using Gaussian oscillators, which are usually indicative of absorption caused by either interband transitions, impurities or defects.

4.1.3. Indium Tin Oxide

As a potential substitute for AZO, indium tin oxide (ITO) sputtering was explored at. ITO was deposited using the 4Wave Inc. cluster sputter deposition tool at the CNST NanoFab of the National Institute of Standards and Technology (NIST) located in Gaithersburg, MD. ITO films were deposited on fused silica wafers at room temperature via ion-beam-assisted sputtering. The deposition system consists of a 3-grid 14 cm RF ion gun directed at 200 mm diameter targets of SiO_2, Al and ITO. All three processes require a small flow of O2 to achieve stoichiometry. Typical conditions were: argon flow rate 3.3x10-7 m^3/s (20 sccm), beam voltage 600 V, beam current 220 mA and acceleration voltage 150 V. The substrate wafers rotated at 10 rpm and were kept at 20 °C. The base vacuum prior to deposition was 2.6×10^{-6} Pa (1.5×10^{-8} Torr). To vary the carrier concentration of ITO, O_2 flow rate was varied between 1.4 sccm and 4.2 sccm. The free electrons in ITO are contributed by the substitutionally entered Sn atoms in the sublattice and from the

doubly charged oxygen vacancies. Thus, a higher O_2 flow rate leads to a lower concentration of O_2 vacancies and in turn reduces the free carrier density while increasing the resistivity of the films. The effect of this reduction is manifested in the dispersion of the real part of the permittivity,

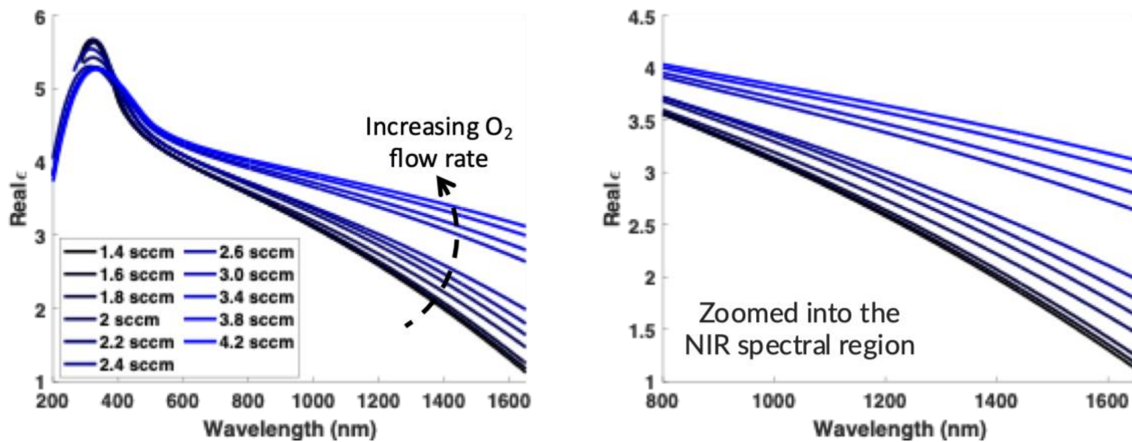

Figure 36: Real part of permittivity of a 50 nm thick ITO film deposited on a fused silica substrate using the 4Wave cluster sputter deposition tool.

as seen in Figure 36. Moreover, as the free carrier density reduces, the effect of the Drude component on the optical response of the materials also reduces, in effect reducing the loss in the all-important, telecommunication wavelengths (Figure 37).

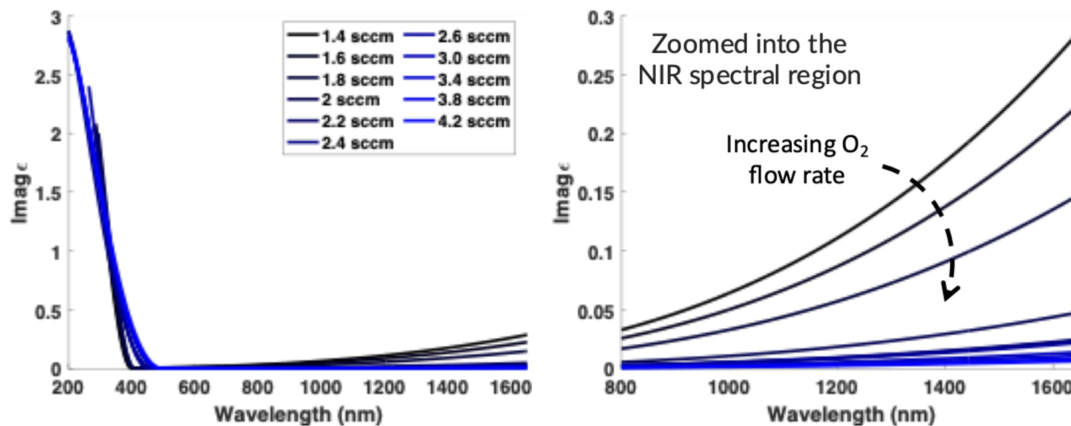

Figure 37: Imaginary part of permittivity of a 50 nm thick ITO film deposited on a fused silica substrate using the 4Wave cluster sputter deposition tool.

From the perspective of the all-oxide modulator, the target was to obtain an imaginary part of permittivity below 0.1, at a free carrier density of ~ 1×10^{20} cm^{-3} (Figure 38). This was readily achievable in these sputtered ITO films. The next crucial check was the conformality of the sputtered films. In the slot modulator design, ITO and the oxide would need to fill the ~40 nm to 50 nm gap in between the However, the sputtering deposition technique is not as conformal as the ALD deposition method, but given a wide enough area, conformality could be achieved. Figure 39 shows ~100 nm ITO deposited in grooves with a varying size between 50 nm and 500 nm. As seen from the images, the narrowest slots do not have an ITO coating in them. This renders the film unsuitable for the all oxide modulator in its current design. An alternative approach is to create a vertical slot, which will be discussed in the following section.

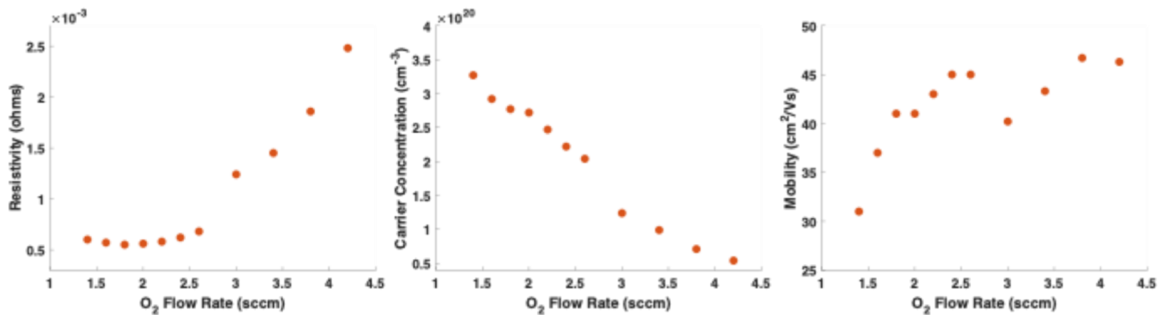

Figure 38: Electrical properties of a 50 nm thick ITO film deposited on a fused silica substrate using the 4Wave cluster sputter deposition tool and measured using the Hall Effect.

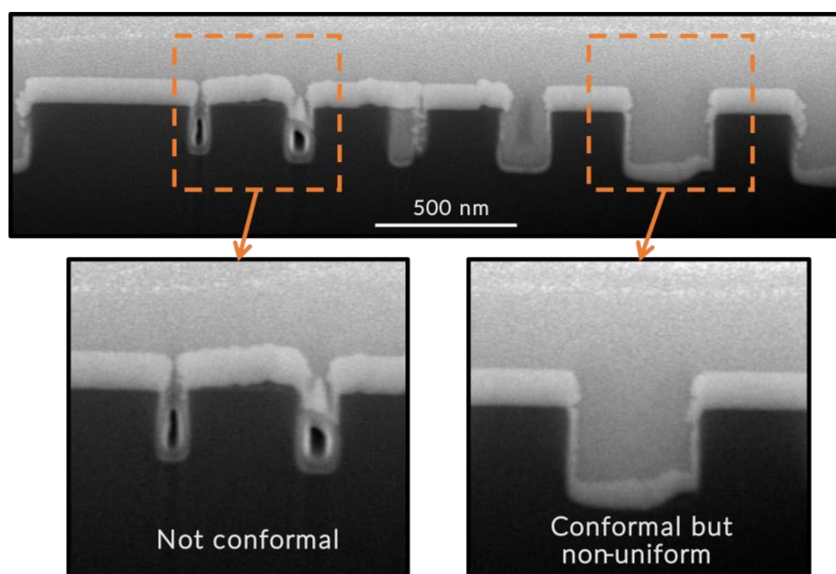

Figure 39: Scanning electron micrograph of focused-ion-beam (FIB) cross-sectional image of sputter-deposition test structure. Structure consists of 125-nm-thick ITO (light gray) sputter-deposited onto a Si grating (dark grey) with line width = 300 nm, trench width = 50 to 1500 nm, and grating depth = 200 nm. The narrowest structures exhibit a non-conformal coating of ITO. The backfilled material in the slot and overcoated material above the grating is Pt (medium gray), which was deposited during the FIB process to assist with the cross-sectioning process.

4.2. Vertical slot design

To overcome the non-conformality of sputtered ITO, a vertical slot modulator design was explored, as shown in Figure 40. Instead of attempting to backfill a horizontal slot, the new device design includes a vertical slot, with ITO and insulator oxide sandwiched in between crystalline Si and sputtered, amorphous Si. The advantages of this design are multi-fold. Firstly, considering that the performance of the device is heavily reliant on the gap width, an accurate and smooth gap is highly beneficial. In this sense a vertical slot, created by material deposition, offers much better control of the gap height as compared to a horizontal slot, fabricated by electron beam lithography (EBL) and etching. Furthermore, planarized Si waveguides, sputtered ITO, and insulator oxide can be expected to be fabricated with sub-2nm roughness, thus enabling to smooth gap interfaces.

Secondly, ITO and oxide can be deposited on top of each other without breaking vacuum, thus ensuring a contamination-free, pristine ITO/ oxide interface. This is especially important as this interface is the heart of the device, where the accumulation region is created on application of a bias voltage.

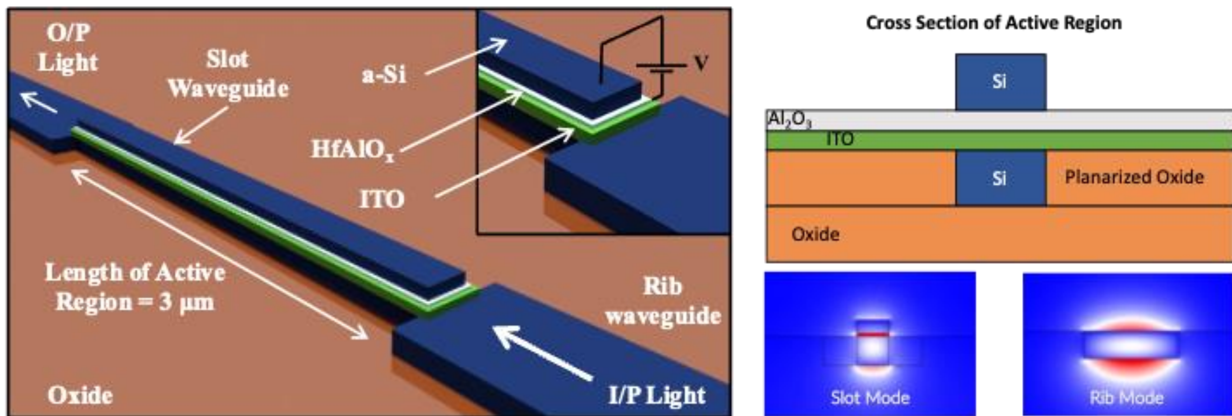

Figure 40: Proposed vertical alternative to the horizontal slot design. The advantages of the vertical slot are multifold. i). Better control over critical slot dimensions, ii). Smooth interfaces at the slot, iii). Potential for depositing ITO and Al_2O_3 without breaking vacuum.

To better understand and visualize the importance of slot in between the two Si rails, see Figure 41. The input mode is confined within the slot at 0V and a 5V bias. At 0V bias, high transmission is desired. The horizontal slot would have resulted in 5 to 10 nm of root mean square roughness, on the optimistic side. This roughness would have caused increased scattering, as the confined light becomes increasingly sensitive to small index/ structure perturbations. On the other hand, traditional Si rib waveguides are not affected by sub 10 nm roughness as the majority of E-field is trapped within the bulk of Si and does not experience the surface roughness as strongly. Furthermore, the figure also contains insets exhibiting the electromagnetic energy being pulled into a ~1nm ENZ region that is created at the interface of ITO/ oxide on application of a 5V bias.

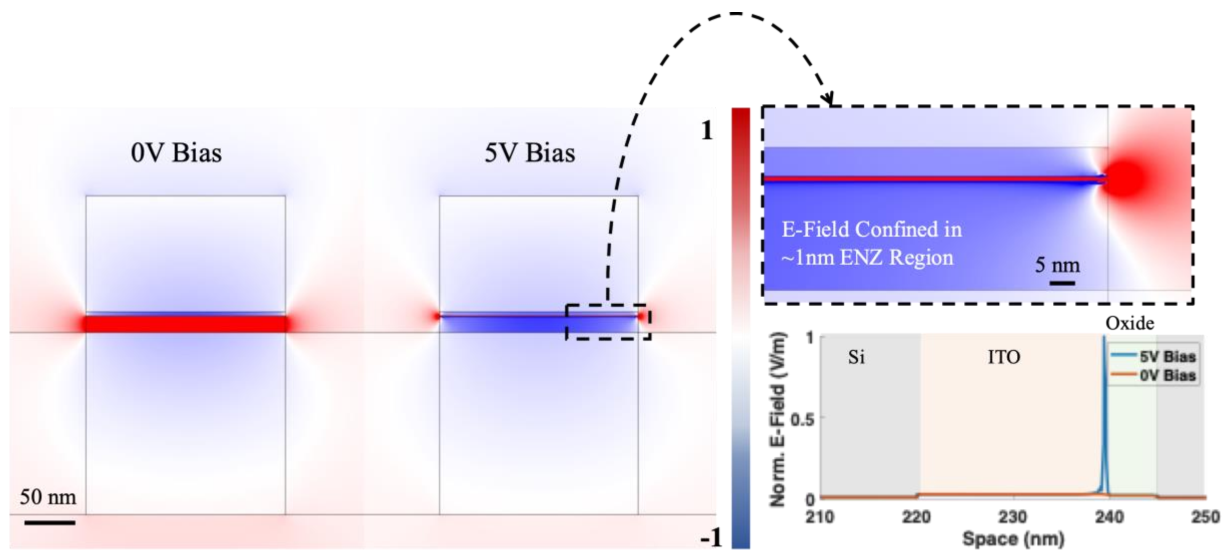

Figure 41: Simulated E-field profiles of the active region at 0V and 5V bias. Simulations performed using an FEM solver, COMSOL. At a bias of 0V, the incoming frequency experiences an all-dielectric structure. With the E-field polarized normal to the substrate, it is confined in the low index region (ITO and Oxide). On application of a 5V bias, a 1 nm region at the interface of ITO/ Oxide now exhibits a permittivity close to 0. The E-field now get confined into this narrow region, as shown in the inset, on right. The graph further demonstrates the drastically enhanced E-field. This thin region also exhibits higher losses due to increased electron-electron scattering, thus, in effect, attenuating the input signal drastically.

The next section of discusses the coupling details, from a rib mode to a slot mode. Unlike the horizontal slot device, which was adiabatically coupled (from rib waveguide to slot waveguide), the vertical slot waveguide is butt-coupled. To enable efficient coupling between the two modes, the effective mode index, and the E-field mode overlap, must be matched. The mode of the vertical slot can be varied by changing the width of the bottom Si waveguide and the thickness of the top a-Si. The result of this is shown in Figure 42(a), where a range of indices between 1.7 and 2.6 is obtained. We pick an effective mode index of ~1.8 due to the following two factors: i). The index of the rib waveguide can vary between 1.5 and 2, so technically any of the parameters these indices

can be selected, ii). From a fabrication perspective, a thinner a-Si layer is easier and more reliable to lift-off, than a thicker layer, thus a thickness of ~120 nm.

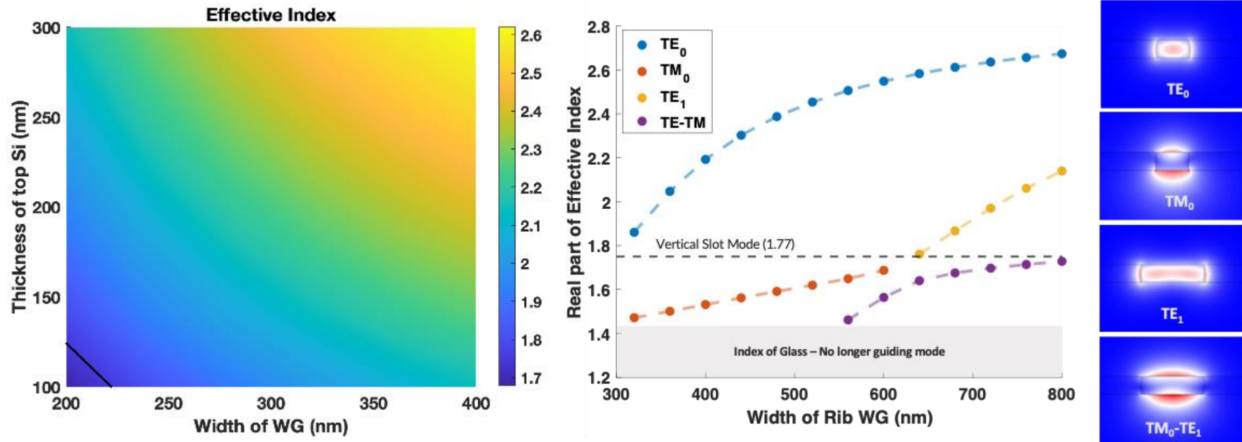

Figure 42: (a). Effective mode index of a vertical slot waveguide as a function of the thickness of the top a-Si and the width of the waveguide (WG). The black line highlights the ~1.77 index selected for device design, (b). The mode indices of a rib waveguide as a function of the width and their corresponding mode profiles.

With a mode index of 1.77, for a vertical slot, the closest TM mode of a rib waveguide that is available, is that of a 750 nm wide rib waveguide, as shown in Figure 42(b). This figure plots all the available modes of a rib waveguide as a function of the rib waveguide width, as that is the only parameter we can tune. Since a vertical slot waveguide requires a vertically polarized mode, we focus our attention on TM and TE-TM hybrid modes. The orange dots represent the TM mode evolution as a function of the width of the rib. As it approaches the mode-index target of 1.77 (index of slot waveguide), the mode splits into TE_1 and $TM\text{-}TE_1$ hybrid. To ensure the correct mode is excited (TE1-TM), we chose a 760 nm wide rib waveguide, as that provides a close match to an index of 1.77. In addition, the mode of interest exists in isolation, ensuring that small fabrication errors do not lead to the wrong mode excitation.

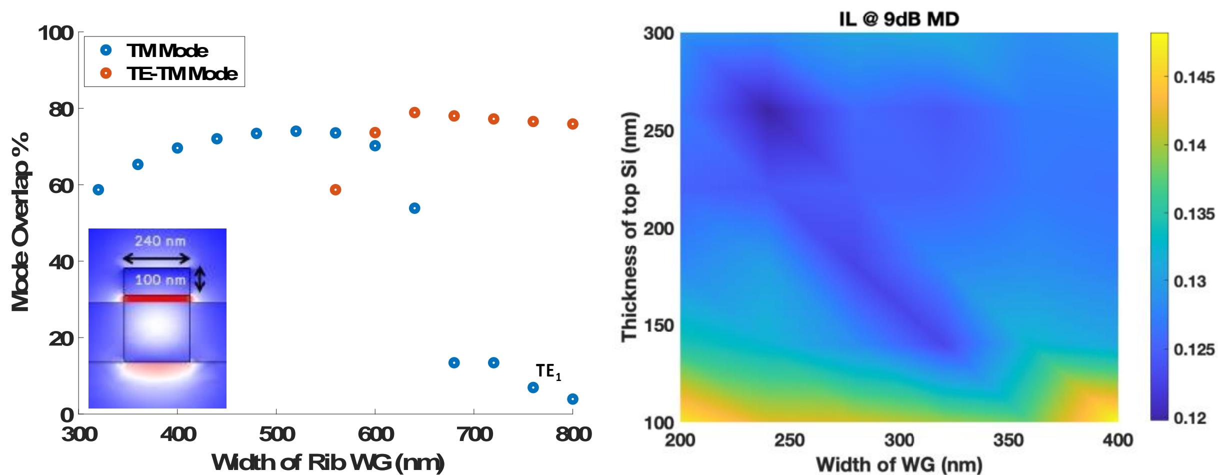

Figure 43: (a) Mode overlap percentage between the vertical slot waveguide and the various modes of the rib waveguide. (b) The insertion loss of the active area for a 9 dB modulation depth as a function of the thickness of the a-Si layer and the width of the waveguide.

To better elucidate the reason of picking the TE-TM hybrid mode over the TE_1 mode, Figure 43a shows the E-field overlap between the vertical slot and the rib waveguide locations. It is readily apparent that the hybrid mode has a much higher (~70%) mode overlap than the TE_1 mode (~10%). The final dimensions for the rib waveguide are: 220 nm by 750 nm, and for the vertical slot are: 100 nm by 240 nm. The final coupling efficiency was estimated from a 3D simulation, and up to 85% energy transfer from the rib to slot mode can be achieved. This corresponds to 0.7 dB loss per coupler. Moreover, power and mode stability are achieved within 1 um of travel distance with negligible beating of power beyond that.

To estimate the performance metrics of the modulator, 2D mode simulations were carried out. The simulations consisted of coupling the semiconductor module to the optics module in COMSOL, which ensures an accurate calculation of the carrier accumulation profile within ITO. As a function of the top a-Si thickness and the width, the IL was calculated for 9dB modulation (which is 3 dB more than the target) and are shown in Figure 43b. It is evident that irrespective of the design, a

record low IL of sub 0.2 dB is achievable. This dramatic improvement of performance of the vertical slot design over that of the horizontal slot design can be mainly attributed to the improved mobility of ITO. The optical mobility of ITO considered in this simulation was 160 cm^2/Vs. While this does seem like an unusually large mobility, the ellipsometer measurements reliably and repeatedly indicate optical losses that correspond to a mobility as high as 160 cm^2/Vs. Further evidence of this is shown in Figure 44

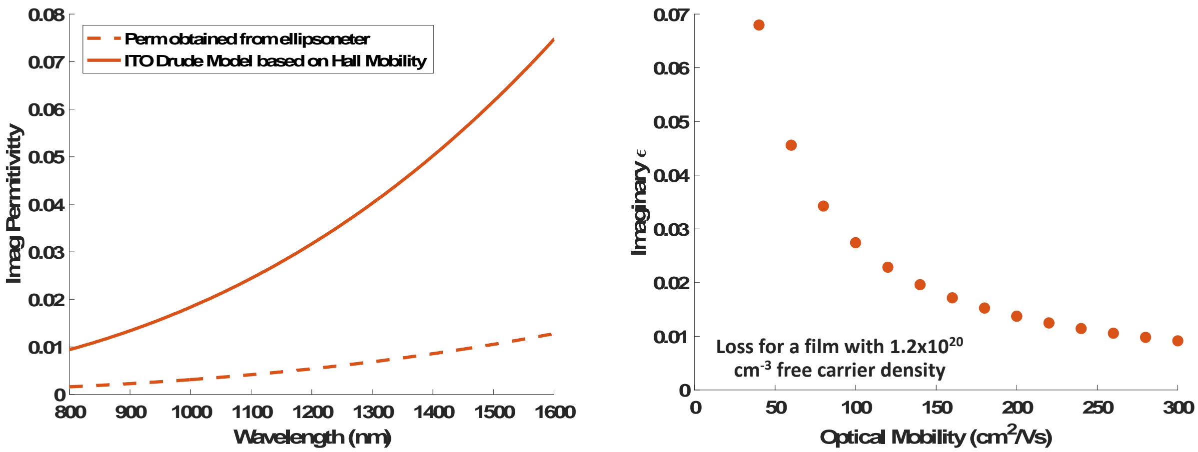

Figure 44: (a) Comparison of the loss of a sputtered ITO film measured using an ellipsometer (dashed line) and the modeled loss based on the values obtained from the Hall effect measurement (solid line). (b) The optical mobility needed to reach the loss measured using the ellipsometer.

Figure 44a plots the permittivity obtained from the ellipsometer (dashed line) and the modelled permittivity based on the data from hall measurements. At a wavelength of 1500 nm, there is over a 5x difference in loss. This is primarily due to the difference in optical and hall mobility. It is not uncommon for these two mobilities to differ, as optical mobility is dominated by short-range scattering whereas the electrical mobility by long-range scattering events. However, as the Figure 44b shows, to obtain a loss low enough, the optical mobility needs to be about 160 cm^2/Vs, whereas

the hall mobility from the Hall effect measurement, suggested a mobility of 40 cm^2/Vs. This difference is unusually large and warrants further investigation.

If this mobility were achievable, the all-oxide modulator would exhibit a record-breaking performance of 9 dB MD with a < 0.2 dB IL. Moreover, with an estimated length of 8 um (1.92 um^2 area and 30 fF capacitance), the RC limited speed of the device is 333 GHz (assuming 100-ohm resistance) and the estimated energy consumption of 480 fJ at a 8V operating voltage.

4.3. All Oxide EO Modulator – Device Fabrication

The fabrication process flow is outlined in Figure 45. It includes 6 aligned EBL steps starting with the patterning of embedded Au alignment markers. This is to avoid stripping of the Au alignment markers in the subsequent chemical mechanical polishing step (CMP). The Au alignment markers are embedded by etching and subsequently backfilling Au using the same patterned resist for both these steps. This is followed by lithography and Si etching dry etching to fabricate Si waveguides and grating couplers. The next step is CMP, critical to the realization of the all-oxide vertical modulator. This involves depositing thick layer of ~60 nm thick SiO_2 layer and then performing CMP to planarize. This will result in sub-nm of smoothness on the top of the wafer. Following CMP, ITO and aluminum oxide insulator (Al_2O_3) are deposited using the sputtering tool without breaking vacuum. Subsequently, ITO and Al_2O_3 are patterned using wet etching processes, such as $FeCl_3$ and TMAH, respectively. Material compatibility has been verified and Al_2O_3 is resistant

to $FeCl_3$. After the patterning of Al_2O_3 and ITO, a-Si and Au contact pads are patterned via liftoff. Out of these 6 EBL processes, 4 of them have been completed, up to the patterning of the oxide.

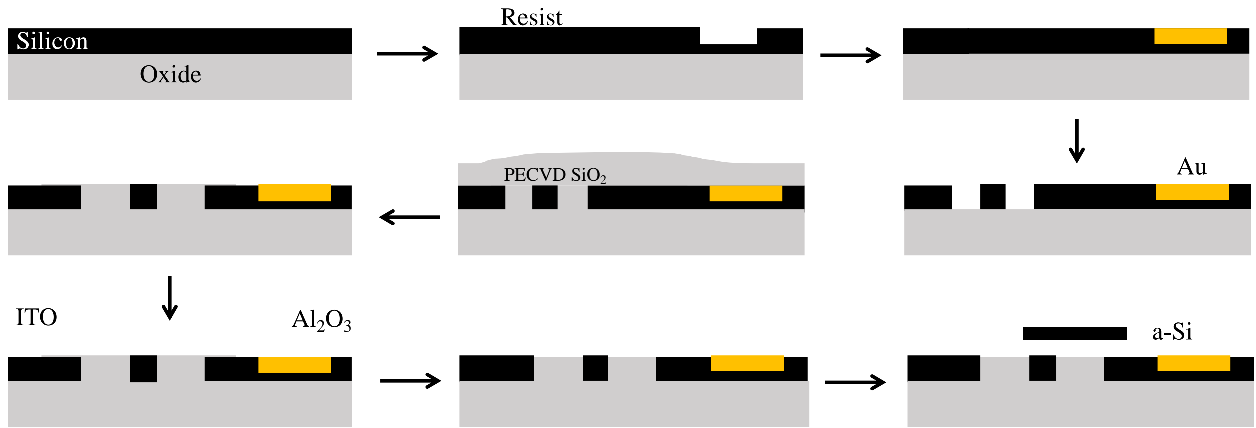

Figure 45: Schematic of the fabrication process, with non-critical alignment steps.

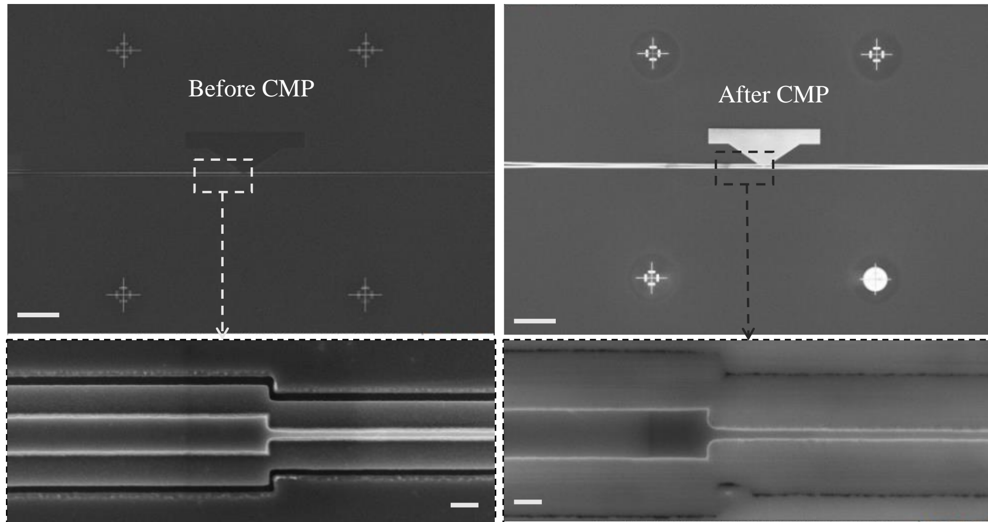

Figure 46: SEM images before and after planarization of the waveguides.

The most critical step to the realization of this device is CMP of the waveguides, as the tolerances are very small. If under or over etched, even with ~20 nm residual SiO_2 remaining or ~20 nm Si

removed, would lead to over a 10% change in height, thus altering the mode profile of the waveguide. To ensure that the process falls within tolerances, a uniform SiO_2 layer was deposited, and several intermediate thickness checks were carried out during the CMP process. This resulted in successful planarization of the wafer, as shown in Figure 46. This was followed by patterning of the ITO and p-Si contacts along with Al2O3 layer, which acts as the insulator. The final image of the device is shown in Figure 47. Note that this was a prototype device fabricated on a 4” Si wafer. The device which can support a guided mode will fabricated on an SOI wafer.

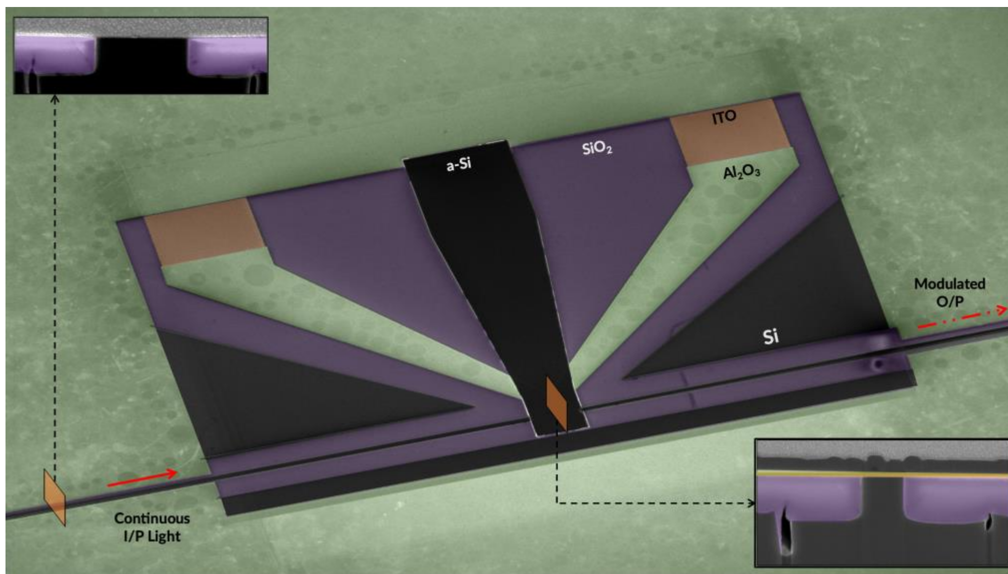

Figure 47: False-color SEM image of the all-oxide EO modulator fabricated on a 4” Si wafer. This is an example of a possible fabrication route to realize the device on a SOI wafer.

4.4. Other Devices – Proposed Fabrication Routes

While the all-oxide modulator will be fabricated, the section below offers proposed fabrication routes to other devices, intended to be used as a reference. The opto-mechanical devices can also be fabricated on commercial silicon-on-insulator (SOI) wafers; however, these would have a 340 nm thick active device layer. This is to reduce the evanescent tail leaking out of the waveguide

and interacting with the metallic layer. The process flow is shown in Figure 48, which begins with electron beam lithography (EBL) on the SOI wafers followed by dry etching in an inductively coupled plasma reactive ion etching (RIE) system using SF_6 and C_4F_8 gases. Next, a planarization process can be done using a 1 um thick spin-coated HSQ layer, which on rapid thermal annealing would form SiO_2. To etch down to the Si waveguide and fabricate the stopper layer, two etch steps (7:1 buffered oxide etch with 1.2 nm/s etch rate), and one EBL step using PMMA can be done. This can be followed by the deposition of MgO, which acts as a sacrificial layer. MgO can be deposited at room temperature using an electron beam evaporation system or using atomic layer deposition, for better thickness control. Following that, an aligned EBL exposure and lift-off can be carried out to fabricate the Al membrane structure. This step needs to be done without exposure to water due to the hygroscopic nature of MgO. Once the Al membrane has been fabricated, the device can be dipped in heavily diluted phosphoric acid, which under etches the membrane by dissolving MgO without harming PMMA. At this point, the Al structure is freely suspended (forming the base of the proposed structures). To realize a modulator, an EO polymer can be spin-coated where it back-fills the airgap. This will be followed by reactive ion etching of the polymer in low density, low-temperature oxygen plasma using Al as a hard mask. This step could lead to a few nm deep oxidation of the Al film, but that will not affect the device, as the light primarily interacts with the bottom side of the Al. If still a problem, a few nm thick protective layer could be added to the top of the Al layer before liftoff. After RIE etching, the polymer can be polarized by placing a bias across Al and Si.

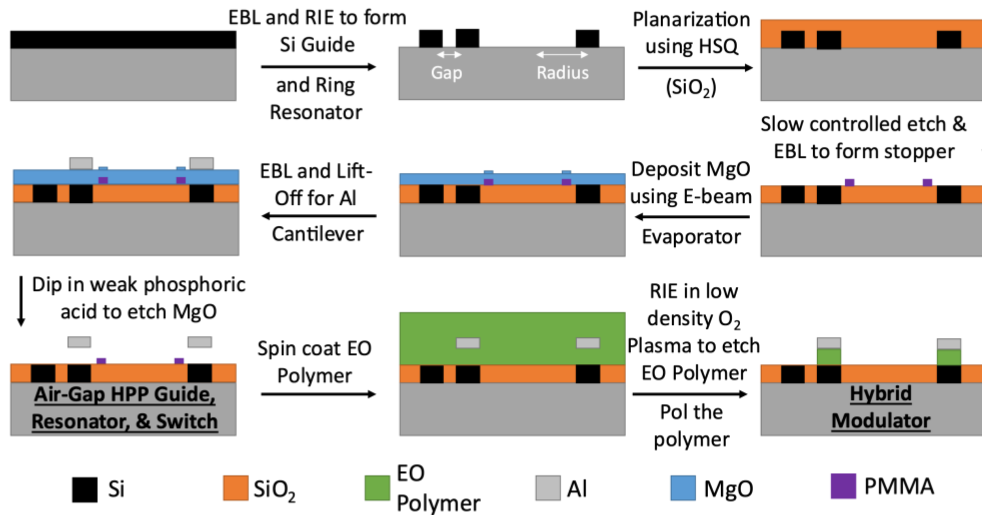

Figure 48: Schematic of the proposed devices, with a single critical alignment step of aligning the Al ring to the Silicon ring.

4.5. Characterization

To test and characterize the devices, a nanophotonic test bench for the optical characterization of the EO modulator is required, which can deliver signals to the device under test (DUT) for characterization. A schematic of the setup is shown in Figure 49. It consists of a tunable laser diode which emits at near IR wavelengths. This is followed by an Erbium doped fiber amplifier (EDFA), which amplifies wavelengths around 1550 nm. The output of the EDFA feeds into the polarization controller which aids in configuring the polarization entering the sample. Once the light is on-chip, it is guided by a waveguide and passes through the active region, which can either be the all-oxide modulator, a hybrid resonator coupled to a cantilever or a hybrid resonator with a polymer. Depending on the active region, the output is coupled into the air using a cleaved end or a grating coupler, which once again goes through an EDFA before being detected.

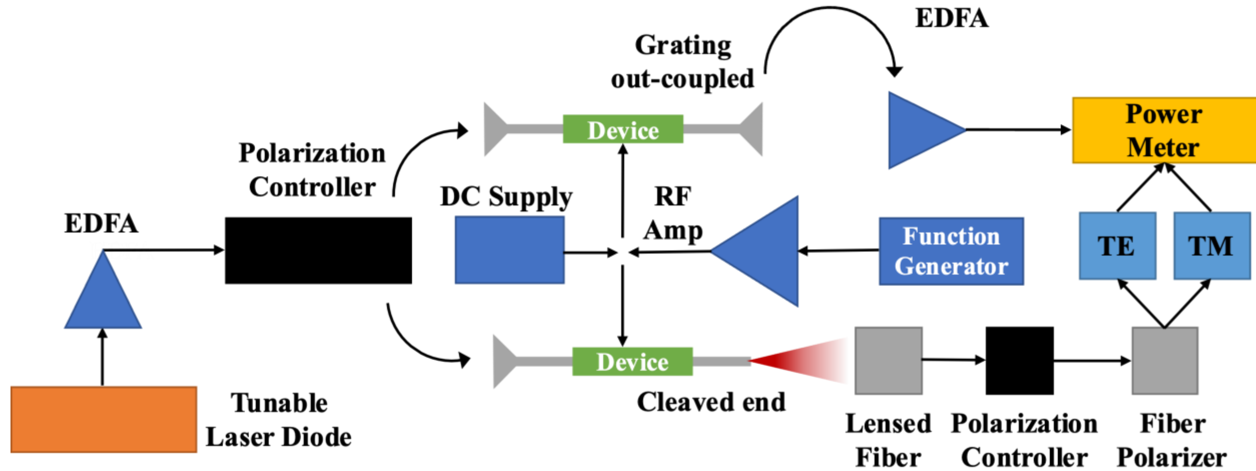

Figure 49: Schematic of the experimental setup used to measure the DC, low frequency, and high frequency response of the devices. EDFA's and RF Amplifiers will be used as required to maintain sufficient signal to noise ratio.

The first step towards testing is to realize a setup that can make passive waveguide measurements. Using the above schematic as a guide, the setup shown in Figure 50 was constructed. 1 is the wavemeter, to verify the wavelength, 2 is the source and the detector, 3 is a fiber amplifier (EDFA) and 4 is a polarization controller. In the subset, 5 is a near IR camera which picks of the scattered light off the sample to enable imaging of the waveguides and gratings. 6 and 7 are the output and input fibers mounted on a translational stage. Lastly, 8 is the sample holder stage. All stages provide X, Y and Z control to aid in precise positioning of the fiber at the input and output grating couplers.

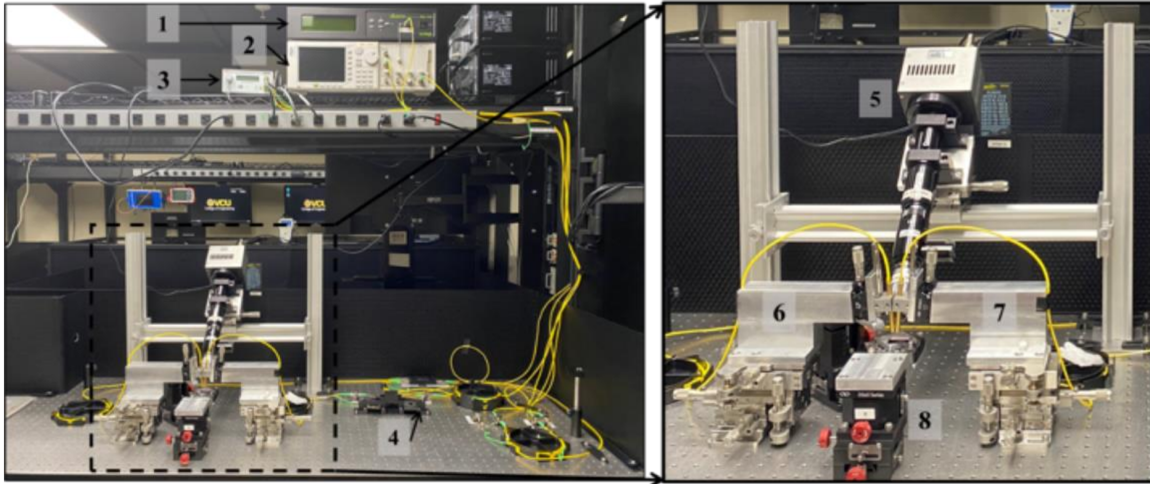

Figure 50: Picture of the constructed test bench which will be used from passive, DC and high frequency measurements of the proposed devices.

Preliminary measurements of passive waveguides through the system have been promising. In our best waveguide, we measured 15 dB of loss across 2 grating couplers and the waveguide, 3 mm long. The loss was low enough, that the output signal was above the threshold limit of the detector, thus negating the use of EDFA. However, in the event the signal dips below the threshold, the EDFA can provide up to 80 dB of amplification, thus providing a wide range of measurable powers.

[This chapter contains results that have been previously published:

3. *D. Fomra, K. Ding, V. Avrutin, Ü. Özgür and N. Kinsey "Al:ZnO as a platform for near-zero-index photonics: enhancing the doping efficiency of atomic layer deposition", Opt. Mater. Express 10, 3060–3072, 2020*
4. *N. Izyumskaya, D. Fomra, K. Ding, H. Morkoç, N. Kinsey, Ü. Özgür and V. Avrutin, "High-Quality Plasmonic Materials TiN and ZnO:Al by Atomic Layer Deposition", Rap. Res. Letter, 2100227 - 15(10), 2021 [Invited]]*

5. CONCLUSION AND FUTURE WORK

Optical technologies play a crucial role in many aspects of modern human life. From the fiber optic cables that make high-speed internet communication possible, to the lasers used in medical procedures and industrial manufacturing, optics are an essential part of our daily lives. One particularly important area of optical technology is photonic integrated circuits, which allow for the manipulation of light signals at the nanoscale. These circuits have paved the way for advanced communication systems, high-speed computing, and other cutting-edge technologies. Despite several benefits such as massive parallelism, high bandwidth and low crosstalk, there are also challenges facing the photonic integrated circuit industry. One of the main challenges is the size disparity between the photonic and electronic elements. This has made integration especially challenging. In addition, the cost and complexity of manufacturing PICs also possess a significant challenge. Unlike electronic integrated circuits, which can be easily mass-produced using standard semiconductor fabrication techniques, PICs require more specialized processes and materials, which can drive up costs.

To address the size disparity while maintaining good overall performance (IL, MD and energy consumption), this thesis has simulated 4 integrated photonic devices and demonstrated a prototype fabrication flow, for the all-oxide modulator. These 4 devices - 2 modulators, 1 router and 1 polarization rotator would be integral parts of realizing most PIC circuits. To design devices with the target performance metrics, we relied on an innovative plasmon-assisted design approach. As part of this design philosophy, either ENZ materials, ring resonators, and mechanical actuation were used in such a way that the light experiences a low loss photonic state when high transmission

is desired and a high loss plasmonic state when low transmission is desired. Employing this approach resulting in not one, but multiple devices with leading performance in a small platform, while critically addressing the loss issue that has so far plagued plasmonic technologies (see performance summary in Table 1). As outlined in Chapter 3 and Chapter 4, the results shown in this table were realized with an FEM solver, COMSOL while the speed and energy calculations are based on the resistance (estimated to be 100 Ω) and capacitance of the devices, which was calculated by treating the active regions as a parallel plate capacitor.

Table 1: Summary table of the performance metrics of the 4 devices simulated in this thesis.

Device	**Type**	**Bandwidth**	**Speed**	**Insertion Loss**	**Energy Usage**	**Size**	**Critical Parameter**
All Oxide EO Modulator	Tier 2 – Material Knob	Broadband (~200nm)	333 GHz	0.2 dB	480 fJ/bit	3 um^2	Mobility of ITO
Hybrid Polymer EO Modulator	Tier 2 – Structure Knob	Narrow (~5nm)	700 GHz	0.2 dB	23 fJ/bit	36 um^2	Pockels coefficient of Polymer
NOEM Router	Tier 1 – Structure Knob	Narrow (~2nm)	6.8 MHz	0.08 dB (1.8 dB)	60 aJ/bit	36 um^2	Mechanical stability of Al
NOEM Polarization Rotator	Tier 1 – Structure Knob	Broadband (~500nm)	5.8 MHz	0.65 dB	200 aJ/bit	6 um^2	Mechanical stability of Al

While it is seen that the proposed devices outpace leading competitors across all metrics, we return to the graphical performance summary, Figure 51a, introduced in Section 3.1, to place the advances outlined here into perspective. Before this work, the solution to improving the large size of photonic devices (blue triangles) through the introduction of plasmonic devices (green circles) resulted in a diagonal transition, where higher compute density (e.g. faster speed in smaller area)

was achieved at the cost of loss. This left the highly desirable loss, high compute density corner of performance unpopulated.

<u>As is depicted in Figure 51, The all-oxide modulator (red circle) and the hybrid polymer modulator (red star) result in vertical transition in this graph. This implies, these devices can achieve high compute per unit area, while maintaining a low, sub-1 dB insertion loss.</u>

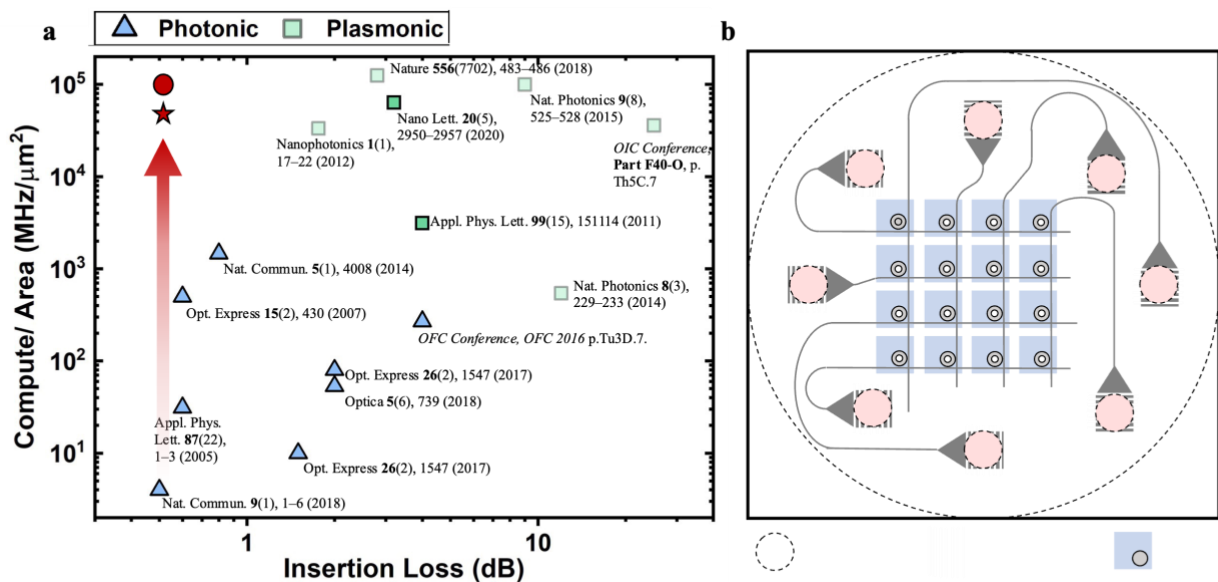

Figure 51: Plot of compute/area vs insertion loss for several photonic and plasmonic devices in literature. In the quest to increase the available compute/ area, these devices had led to an increase in insertion loss. However, the all-oxide modulator (red circle) and the hybrid polymer EO modulator (red star), with their innovative plasmon-assisted design principle, can introduce a vertical transition in the graph, (b) conceptual schematic of miniaturization of PIC circuits.

With this advance comes entirely new capabilities in PIC design. For example, Figure 51b shows the benefits of miniaturization of PIC circuits that is only possible through the use of the low-loss and compact devices proposed herein. With the radically reduced IL and size of the HPP "Plasmon-Assisted" components, new avenues to realize ultra-high-density dynamically reconfigurable photonic circuits, field-programmable pho-tonic chips, and routing hubs are now possible. To

illustrate one such case, common multi-core fibers contain between 4 and 8 cores. When placing the fiber normal to the surface of the chip, 2×2 and 4×4 switching networks could be designed to fit within the area of the fiber itself (~12,000 μm^2 for a 125 μm diameter fiber), requiring only ~1,600 μm^2 (16 switches needed for 4×4, each taking ~100 μm^2 when integrated) leaving plenty of room for waveguide routing, grating couplers, etc., see example configuration in Figure 51b. Here, by moving to an out-of-plane approach and minimizing com-ponents to fit within the fiber area, up to 4096 connections/mm^2 can be achieved.

<u>These devices have the potential to lead to an entirely plasmonic PIC, as outlined in the introduction, by overcoming the loss limitation for not one but multiple components.</u>

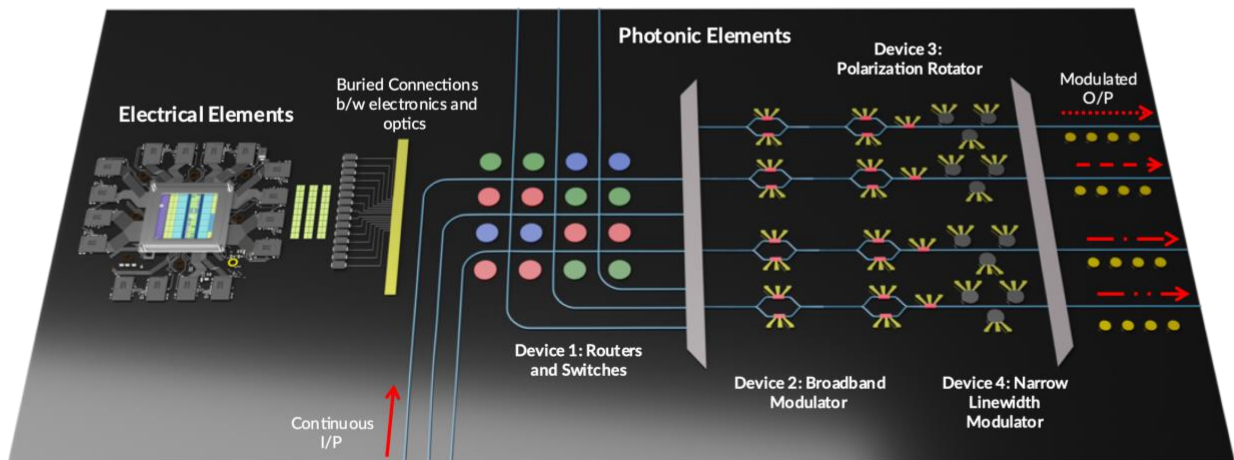

Figure 52: A rendering of a plasmonic PIC. The size disparity between the electrical and optical components have been reduced. Furthermore, by using plasmon-assisted design principles, these devices have overcome the loss limitation, traditionally associated with plasmonic devices. Circuits such as these have important implications for the aerospace and telecommunication, industry as discussed in the introduction.

Finally, miniaturization and enhanced speed and energy efficiencies could lead to the widespread adoption of PICs and the realization of all-plasmonic PIC designs as originally envisioned in

Section 1 (see Figure 52). This could open many new possibilities for technology and communication. For example, PICs could enable the development of high-speed, high-capacity communication networks that could support advanced applications such as remote surgery, autonomous vehicles, and high-definition virtual reality. In addition, PICs could be used to create ultra-fast computers that could handle complex tasks such as large-scale data analysis, weather modeling, and drug discovery. PICs could also be used in medical imaging, allowing for faster and more detailed scans. Overall, the widespread adoption of PICs could lead to major advances in many different fields. However, the path to widespread adoption is fraught with challenges, and the materials and devices proposed/ developed in this thesis hopes to make an incremental advance towards achieving this goal.

5.1. Future Work

While the work within this thesis outlined a pathway to realize low-loss, compact, and high speed plasmonic devices, it is important to consider the fact that the performance metrics are the best estimates obtained from a combination of FEM simulations and realistic assumptions. As a result, significant work remains in refining these assumptions, and subsequently tailoring various metrics (i.e., geometry, material properties), as one works towards realizing each device. For example, a key parameter of the all-oxide modulator is the mobility of ITO (see Table 1 for key parameters of all devices). The electrical mobility dictates the resistance, which in turn affects the operating speed, while the optical mobility dictates the loss experienced in the device. While existing measurements support the assumptions taken within this thesis, it is possible that during final device integration the mobility could be lower than expected due to fabrication limitations or material compatibility. However, we note that even in the event that the mobility is lower than our

estimates (for example, 80 cm^2/Vs as opposed to the measured 160 cm^2/Vs), the all-oxide modulator would still outperform the competing devices in literature, but not by as wide of a margin as currently predicted (i.e., IL ~ 0.4 would increase to ~0.8 dB). Similar nonidealities in the key parameters of the remaining devices (see Table 1) would impact the performance. Quantifying and mitigating these constraints are key for future work and in realizing these devices experimentally.

Beyond the challenges to realize the proposed devices, the concept of plasmon-assisted devices is not limited to the devices simulated in the thesis. It can be applied to various other components of a PIC chip such as phase shifters, multiplexers and demultiplexers. There is immense potential to explore these devices. Furthermore, looking beyond PICs, active metasurfaces have gained a lot of attention over the last few years [103–107]. The performance of these metasurfaces can be improved as well, using the concept of plasmon-assisted design. For example, plasmonic based reflection or transmission modulators suffer from broad resonances. Moving to a hybrid approach coupled with ENZ materials can enable sharper resonances, as a result of reduced losses. However, the high capacitances of large area metasurfaces could limit the speed and result in a large energy consumption. These trade-offs would need to be carefully balanced.

REFERENCES

1. Cisco Inc., *Cisco Annual Internet Report (2018-2023)* (2020).
2. R. Pimpinella, *Light Into Money* (2019).
3. R. Umbrasas, *Monitoring Petabyte-Scale AI Data Lakes in Azure* (2017).
4. K. Hazelwood, S. Bird, D. Brooks, S. Chintala, U. Diril, D. Dzhulgakov, M. Fawzy, B. Jia, Y. Jia, A. Karlo, J. Law, K. Lee, J. Lu, P. Noordhuis, M. Smelyanskiy, L. Xiong, and X. Wang, *Applied Machine Learning at Facebook: A Datacenter Infrastructure Perspective* (2020).
5. "Unlocking the True Potential of AI with In-Package Optical I/O - Ayar Labs," https://ayarlabs.com/unlocking-the-true-potential-of-ai-with-in-package-optical-i-o/.
6. *Unleashing Opportunities with Optical I/O for the Aerospace Industry - Ayar Labs* (n.d.).
7. "Six Reasons the Aerospace Sector Needs Optical I/O Solutions - Ayar Labs," https://ayarlabs.com/six-reasons-the-aerospace-sector-needs-optical-i-o/.
8. M. Intelligence, *OPTICAL MODULATORS MARKET - GROWTH, TRENDS, COVID-19 IMPACT, AND FORECASTS (2021 - 2026)* (2020).
9. "AIM Photonics," .
10. H. Zhou, J. Dong, J. Cheng, W. Dong, C. Huang, Y. Shen, Q. Zhang, M. Gu, C. Qian, H. Chen, Z. Ruan, and X. Zhang, "Photonic matrix multiplication lights up photonic accelerator and beyond," Light: Science & Applications 2022 11:1 **11**, 1–21 (2022).

11. S. Saha, C. Hong, D. Fomra, U. Ozgur, V. Avrutin, J. C. Ndukaife, J. C. Ndukaife, and N. Kinsey, "On-chip integrated quantum emitter with 'trap-enhance-guide': a simulation approach," Optics Express, Vol. 30, Issue 26, pp. 48051-48060 **30**, 48051–48060 (2022).

12. J. C. Ndukaife, V. M. Shalaev, and A. Boltasseva, "Plasmonics-turning loss into gain: The optical losses usually associated with plasmonic materials could be used in applications," Science (1979) **351**, 334–335 (2016).

13. S. A. Maier, *Plasmonics: Fundamentals and Applications* (Springer US, 2007).

14. M. Fox, *Optical Properties of Solid* (Oxford University Press, 2001).

15. R. Secondo, D. Fomra, N. Izyumskaya, V. Avrutin, J. N. Hilfiker, A. Martin, Ü. Özgür, and N. Kinsey, "Reliable modeling of ultrathin alternative plasmonic materials using spectroscopic ellipsometry [Invited]," Opt Mater Express **9**, 760 (2019).

16. E. Langereis, S. B. S. Heil, H. C. M. Knoops, W. Keuning, M. C. M. van de Sanden, and W. M. M. Kessels, "In situ spectroscopic ellipsometry as a versatile tool for studying atomic layer deposition," J Phys D Appl Phys **42**, 073001 (2009).

17. R. P. Sugavaneshwar, S. Ishii, T. D. Dao, A. Ohi, T. Nabatame, and T. Nagao, "Fabrication of Highly Metallic TiN Films by Pulsed Laser Deposition Method for Plasmonic Applications," ACS Photonics **5**, 814–819 (2018).

18. H. G. Tompkins and J. N. Hilfiker, *Spectroscopic Ellipsometry: Practical Application to Thin Film Characterization*, First (Momentum Press, 2015).

19. B. Johs and J. S. Hale, "Dielectric function representation by B-splines," physica status solidi (a) **205**, 715–719 (2008).

20. J. N. Hilfiker, R. a Synowicki, and H. G. Tompkins, "Spectroscopic Ellipsometry Methods for Thin Absorbing Coatings," https://www.google.com/search?client=safari&rls=en&q="Spectroscopic+ellipsometry+methods+for+thin+absorbing+coatings&ie=UTF-8&oe=UTF-8.

21. J. N. Hilfiker, N. Singh, T. Tiwald, D. Convey, S. M. Smith, J. H. Baker, and H. G. Tompkins, "Survey of methods to characterize thin absorbing films with Spectroscopic Ellipsometry," Thin Solid Films **516**, 7979–7989 (2008).

22. D. K. Gramotnev and S. I. Bozhevolnyi, "Plasmonics beyond the diffraction limit," Nat Photonics **4**, 83–91 (2010).

23. D. Fomra, M. Mamun, K. Ding, V. Avrutin, Ü. Özgür, and N. Kinsey, "Plasmonic colors in titanium nitride for robust and covert security features," Opt Express **29**, 19586 (2021).

24. N. Izyumskaya, D. Fomra, K. Ding, H. Morkoç, N. Kinsey, Ü. Özgür, and V. Avrutin, "High-Quality Plasmonic Materials TiN and ZnO:Al by Atomic Layer Deposition," Physica Status Solidi - Rapid Research Letters 2100227 (2021).

25. K. Ding, D. Fomra, A. v. Kvit, H. Morkoç, N. Kinsey, Ü. Özgür, and V. Avrutin, "A Platform for Complementary Metal-Oxide-Semiconductor Compatible Plasmonics: High Plasmonic Quality Titanium Nitride Thin Films on Si (001) with a MgO Interlayer," Adv Photonics Res **2**, 2000210 (2021).

26. M. Mesch, B. Metzger, M. Hentschel, and H. Giessen, "Nonlinear Plasmonic Sensing," Nano Lett **16**, 3155–3159 (2016).

27. M. Kauranen and A. V. Zayats, "Nonlinear plasmonics," Nat Photonics **6**, 737–748 (2012).

28. N. I. Zheludev and Y. S. Kivshar, "From metamaterials to metadevices," Nat Mater **11**, 917–924 (2012).

29. J. B. Pendry, A. Aubry, D. R. Smith, and S. A. Maier, "Transformation optics and subwavelength control of light," Science (1979) **337**, 549–552 (2012).

30. D. R. Smith, J. B. Pendry, and M. C. K. Wiltshire, "Metamaterials and negative refractive index," Science **305**, 788–92 (2004).

31. E. E. Narimanov and A. V. Kildishev, "Optical black hole: Broadband omnidirectional light absorber," Appl Phys Lett **95**, 041106 (2009).

32. J. B. Pendry, "Negative refraction makes a perfect lens," Phys Rev Lett **85**, 3966–3969 (2000).

33. A. She, S. Zhang, S. Shian, D. R. Clarke, and F. Capasso, "Adaptive metalenses with simultaneous electrical control of focal length, astigmatism, and shift," Sci Adv **4**, eaap9957 (2018).

34. Y. W. Huang, H. W. H. Lee, R. Sokhoyan, R. A. Pala, K. Thyagarajan, S. Han, D. P. Tsai, and H. A. Atwater, "Gate-Tunable Conducting Oxide Metasurfaces," Nano Lett **16**, 5319–5325 (2016).

35. C. Haffner, D. Chelladurai, Y. Fedoryshyn, A. Josten, B. Baeuerle, W. Heni, T. Watanabe, T. Cui, B. Cheng, S. Saha, D. L. Elder, Larry. R. Dalton, A. Boltasseva, V. M. Shalaev, N. Kinsey, and J. Leuthold, "Low-loss plasmon-assisted electro-optic modulator," Nature **556**, 483–486 (2018).

36. M. Ayata, Y. Fedoryshyn, W. Heni, B. Baeuerle, A. Josten, M. Zahner, U. Koch, Y. Salamin, C. Hoessbacher, C. Haffner, D. L. Elder, L. R. Dalton, and J. Leuthold, "High-speed plasmonic modulator in a single metal layer," Science (1979) **358**, 630–632 (2017).

37. Y. Kim, P. C. Wu, R. Sokhoyan, K. Mauser, R. Glaudell, G. Kafaie Shirmanesh, and H. A. Atwater, "Phase Modulation with Electrically Tunable Vanadium Dioxide Phase-Change Metasurfaces," Nano Lett **19**, 3961–3968 (2019).

38. C. Haffner, A. Joerg, M. Doderer, F. Mayor, D. Chelladurai, Y. Fedoryshyn, C. I. Roman, M. Mazur, M. Burla, H. J. Lezec, V. A. Aksyuk, and J. Leuthold, "Nano-opto-electro-mechanical switches operated at CMOS-level voltages.," Science **366**, 860–864 (2019).

39. M. G. Wood, S. Campione, S. Parameswaran, T. S. Luk, J. R. Wendt, D. K. Serkland, and G. A. Keeler, "Gigahertz speed operation of epsilon-near-zero silicon photonic modulators," Optica **5**, 233 (2018).

40. A. Anopchenko, L. Tao, C. Arndt, and H. W. H. Lee, "Field-Effect Tunable and Broadband Epsilon-Near-Zero Perfect Absorbers with Deep Subwavelength Thickness," ACS Photonics **5**, 2631–2637 (2018).

41. N. Kinsey, C. DeVault, A. Boltasseva, and V. M. Shalaev, "Near-zero-index materials for photonics," Nat Rev Mater (2019).

42. Q. Gao, E. Li, and A. X. Wang, "Comparative analysis of transparent conductive oxide electro-absorption modulators [Invited]," Opt Mater Express **8**, 2850 (2018).

43. N. Kinsey, C. DeVault, J. Kim, M. Ferrera, V. M. Shalaev, and A. Boltasseva, "Epsilon-near-zero Al-doped ZnO for ultrafast switching at telecom wavelengths," Optica **2**, 616 (2015).

44. E. Feigenbaum, K. Diest, and H. A. Atwater, "Unity-order index change in transparent conducting oxides at visible frequencies," Nano Lett **10**, 2111–2116 (2010).

45. N. Engheta, "Pursuing Near-Zero Response," **340**, 286–288 (2013).

46. I. Liberal and N. Engheta, "Near-zero refractive index photonics," Nat Photonics **11**, 149–158 (2017).

47. M. Clerici, N. Kinsey, C. DeVault, J. Kim, E. G. Carnemolla, L. Caspani, A. Shaltout, D. Faccio, V. Shalaev, A. Boltasseva, and M. Ferrera, "Controlling hybrid nonlinearities in transparent conducting oxides via two-colour excitation," Nat Commun **8**, 16139 (2017).

48. N. Kinsey, R. Secondo, and D. Fomra, "Optical nonlinearities in transparent conducting oxides-the role of loss," in *2019 IEEE Research and Applications of Photonics in Defense Conference, RAPID 2019 - Proceedings* (Institute of Electrical and Electronics Engineers Inc., 2019).

49. R. Secondo, A. Ball, B. Diroll, D. Fomra, K. Ding, V. Avrutin, Özgür, D. O. Demchenko, J. B. Khurgin, and N. Kinsey, "Deterministic modeling of hybrid nonlinear effects in epsilon-near-zero thin films," Appl Phys Lett **120**, 031103 (2022).

50. D. Thomson, A. Zilkie, J. E. Bowers, T. Komljenovic, G. T. Reed, L. Vivien, D. Marris-Morini, E. Cassan, L. Virot, J. M. Fédéli, J. M. Hartmann, J. H. Schmid, D. X. Xu, F. Boeuf, P. O'Brien, G. Z. Mashanovich, and M. Nedeljkovic, "Roadmap on silicon photonics," Journal of Optics **18**, 073003 (2016).

51. A. Olivieri, C. Chen, S. Hassan, E. Lisicka-Skrzek, R. N. Tait, and P. Berini, "Plasmonic Nanostructured Metal-Oxide-Semiconductor Reflection Modulators," Nano Lett **15**, 2304–2311 (2015).

52. S. A. Maier, M. L. Brongersma, P. G. Kik, S. Meltzer, A. A. G. Requicha, and H. A. Atwater, "Plasmonics - A route to nanoscale optical devices," Advanced Materials **13**, 1501–1505 (2001).

53. E. Ozbay, "Plasmonics: Merging photonics and electronics at nanoscale dimensions," Science (1979) **311**, 189–193 (2006).

54. G. T. Reed, G. Mashanovich, F. Y. Gardes, and D. J. Thomson, "Silicon optical modulators," Nat Photonics **4**, 518–526 (2010).

55. G. Sinatkas, A. Pitilakis, D. C. Zografopoulos, R. Beccherelli, and E. E. Kriezis, "Transparent conducting oxide electro-optic modulators on silicon platforms: A comprehensive study based on the drift-diffusion semiconductor model," J Appl Phys **121**, 023109 (2017).

56. R. Amin, J. B. Khurgin, and V. J. Sorger, "Waveguide-based electro-absorption modulator performance: comparative analysis," Opt Express **26**, 203–204 (2018).

57. C. Wang, M. Zhang, B. Stern, M. Lipson, and M. Loncar, "Nanophotonic Lithium Niobate Electro-optic Modulators," Opt Express **26**, 1547 (2017).

58. M. Zhang, C. Wang, R. Cheng, A. Shams-Ansari, and M. Loncar, "Monolithic Ultrahigh-Q Lithium Niobate Microring Resonator," **4**, 1536–1537 (2017).

59. C. Haffner, W. Heni, Y. Fedoryshyn, J. Niegemann, A. Melikyan, D. L. Elder, B. Baeuerle, Y. Salamin, A. Josten, U. Koch, C. Hoessbacher, F. Ducry, L. Juchli, A. Emboras, D. Hillerkuss, M. Kohl, L. R. Dalton, C. Hafner, and J. Leuthold, "All-plasmonic Mach–Zehnder modulator enabling optical high-speed communication at the microscale," Nat Photonics **9**, 525–528 (2015).

60. V. J. Sorger, N. D. Lanzillotti-Kimura, R. M. Ma, and X. Zhang, "Ultra-compact silicon nanophotonic modulator with broadband response," Nanophotonics **1**, 17–22 (2012).

61. S. Md, "LOW INSERTION-LOSS NANOPHOTONIC MODULATORS THROUGH EPSILON-NEAR-ZERO MATERIAL-BASED PLASMON- ASSISTED APPROACH FOR INTEGRATED PHOTONICS," Virginia Commonwealth University (2022).

62. H. W. Lee, G. Papadakis, S. P. Burgos, K. Chander, A. Kriesch, R. Pala, U. Peschel, and H. A. Atwater, "Nanoscale conducting oxide PlasMOStor," Nano Lett **14**, 6463–6468 (2014).

63. Y. Tu, Q. Zhang, and H. Ågren, "Electric Field Poled Polymeric Nonlinear Optical Systems: Molecular Dynamics Simulations of Poly(methyl methacrylate) Doped with Disperse Red Chromophores," J Phys Chem B **111**, 3591–3598 (2007).

64. W. M. Zhang, H. Yan, Z. K. Peng, and G. Meng, "Electrostatic pull-in instability in MEMS/NEMS: A review," Sens Actuators A Phys **214**, 187–218 (2014).

65. A. Peschot, C. Qian, and T.-J. Liu, "Nanoelectromechanical Switches for Low-Power Digital Computing," Micromachines (Basel) **6**, 1046–1065 (2015).

66. T. J. Seok, N. Quack, S. Han, R. S. Muller, and M. C. Wu, "Large-scale broadband digital silicon photonic switches with vertical adiabatic couplers," Optica **3**, 64 (2016).

67. A. J. Wallash and L. Levit, "Electrical breakdown and ESD phenomena for devices with nanometer-to-micron gaps," in *Reliability, Testing, and Characterization of MEMS/MOEMS II*, R. Ramesham and D. M. Tanner, eds. (SPIE, 2003), Vol. 4980, p. 87.

68. Q. Cheng, S. Rumley, M. Bahadori, and K. Bergman, "Photonic switching in high performance datacenters [Invited]," Opt Express **26**, 16022 (2018).

69. D. Pérez, I. Gasulla, J. Capmany, and R. A. Soref, "Reconfigurable lattice mesh designs for programmable photonic processors," Opt Express **24**, 12093 (2016).

70. L. Zhuang, C. G. H. Roeloffzen, M. Hoekman, K.-J. Boller, and A. J. Lowery, "Programmable photonic signal processor chip for radiofrequency applications," Optica **2**, 854 (2015).

71. J. Luo, S. Huang, Z. Shi, B. M. Polishak, X.-H. Zhou, and A. K. Y. Jen, "Tailored Organic Electro-optic Materials and Their Hybrid Systems for Device Applications," Chemistry of Materials **23**, 544–553 (2011).

72. T. Gray, T. D. Kim, D. B. Knorr, J. Luo, A. K. Y. Jen, and R. M. Overney, "Mesoscale dynamics and cooperativity of networking dendronized nonlinear optical molecular glasses," Nano Lett **8**, 754–759 (2008).

73. L. R. Dalton, P. A. Sullivan, and D. H. Bale, "Electric field poled organic electro-optic materials: State of the art and future prospects," Chem Rev **110**, 25–55 (2010).

74. E. Timurdogan, C. M. Sorace-Agaskar, J. Sun, E. Shah Hosseini, A. Biberman, and M. R. Watts, "An ultralow power athermal silicon modulator," Nat Commun **5**, 4008 (2014).

75. Q. Xu, B. Schmidt, S. Pradhan, and M. Lipson, "Micrometre-scale silicon electro-optic modulator," Nature **435**, 325–327 (2005).

76. D. Fomra, K. Ding, V. Avrutin, Ü. Özgür, and N. Kinsey, "Al:ZnO as a platform for near-zero-index photonics: enhancing the doping efficiency of atomic layer deposition," Opt Mater Express **10**, 3060–3072 (2020).

77. E. Li, Q. Gao, R. T. Chen, and A. X. Wang, "Ultra-Compact Silicon-Conductive Oxide Nano-Cavity Modulator with 0.02 Lambda-Cubic Active Volume," Nano Lett acs.nanolett.7b04588 (2018).

78. Ü. Özgür, Y. I. Alivov, C. Liu, A. Teke, M. A. Reshchikov, S. Doğan, V. Avrutin, S. J. Cho, and H. Morkọ, "A comprehensive review of ZnO materials and devices," J Appl Phys **98**, 1–103 (2005).

79. J. Kim, G. V. Naik, A. V. Gavrilenko, K. Dondapati, V. I. Gavrilenko, S. M. Prokes, O. J. Glembocki, V. M. Shalaev, and A. Boltasseva, "Optical properties of gallium-doped zinc oxide-a low-loss plasmonic material: First-principles theory and experiment," Phys Rev X **3**, 041037 (2014).

80. F. Ruske, A. Pflug, V. Sittinger, B. Szyszka, D. Greiner, and B. Rech, "Optical modeling of free electron behavior in highly doped ZnO films," Thin Solid Films **518**, 1289–1293 (2009).

81. Y. Wang, A. Capretti, and L. Dal Negro, "Wide tuning of the optical and structural properties of alternative plasmonic materials," Opt Mater Express **5**, 2415 (2015).

82. A. V. Kvit, A. B. Yankovich, V. Avrutin, H. Liu, N. Izyumskaya, Ü. Özgür, H. Morkoç, and P. M. Voyles, "Impurity distribution and microstructure of Ga-doped ZnO films grown by molecular beam epitaxy," J Appl Phys **112**, 123527 (2012).

83. V. Bhosle, J. T. Prater, F. Yang, D. Burk, S. R. Forrest, and J. Narayan, "Gallium-doped zinc oxide films as transparent electrodes for organic solar cell applications," J Appl Phys **102**, 023501 (2007).

84. A. Anopchenko, S. Gurung, L. Tao, C. Arndt, and H. W. H. Lee, "Atomic layer deposition of ultra-thin and smooth Al-doped ZnO for zero-index photonics," Mater Res Express **5**, (2018).

85. E. Shkondin, O. Takayama, M. E. A. Panah, P. Liu, P. V Larsen, M. D. Mar, F. Jensen, and A. V Lavrinenko, "Large-scale high aspect ratio Al-doped ZnO nanopillars arrays as anisotropic metamaterials," Opt Mater Express **7**, 1606 (2017).

86. C. T. Riley, J. S. T. Smalley, K. W. Post, D. N. Basov, Y. Fainman, D. Wang, Z. Liu, and D. J. Sirbuly, "High-Quality, Ultraconformal Aluminum-Doped Zinc Oxide Nanoplasmonic and Hyperbolic Metamaterials," Small **12**, 892–901 (2016).

87. Y. Li, R. Yao, H. Wang, X. Wu, J. Wu, X. Wu, and W. Qin, "Enhanced Performance in Al-Doped ZnO Based Transparent Flexible Transparent Thin-Film Transistors Due to Oxygen Vacancy in ZnO Film with Zn-Al-O Interfaces Fabricated by Atomic Layer Deposition," ACS Appl Mater Interfaces **9**, 11711–11720 (2017).

88. A. K. Pradhan, R. M. Mundle, K. Santiago, J. R. Skuza, B. Xiao, K. D. Song, M. Bahoura, R. Cheaito, and P. E. Hopkins, "Extreme tunability in aluminum doped Zinc Oxide plasmonic materials for near-infrared applications," Sci Rep **4**, 6415 (2014).

89. Y.-L. Lee, T.-H. Huang, C.-L. Ho, and M.-C. Wu, "The Sandwich Structure of Ga-Doped ZnO Thin Films Grown via H 2 O-, O 2 -, and O 3 -Based Atomic Layer Deposition," ECS Journal of Solid State Science and Technology **2**, Q182–Q186 (2013).

90. T. Weckman and K. Laasonen, "Atomic layer deposition of zinc oxide: Diethyl zinc reactions and surface saturation from first-principles," Journal of Physical Chemistry C **120**, 21460–21471 (2016).

91. D. H. Kim, S. Bin Baek, and Y. C. Kim, "Energy barriers for trimethylaluminum reaction with varying surface hydroxyl density," Appl Surf Sci **258**, 225–229 (2011).

92. J. Hu and R. G. Gordon, "Textured aluminum-doped zinc oxide thin films from atmospheric pressure chemical-vapor deposition," J Appl Phys **71**, 880–890 (1992).

93. J. S. Na, Q. Peng, G. Scarel, and G. N. Parsons, "Role of gas doping sequence in surface reactions and dopant incorporation during atomic layer deposition of Al-Doped ZnO," Chemistry of Materials **21**, 5585–5593 (2009).

94. D.-J. Lee, J.-Y. Kwon, S.-H. Kim, H.-M. Kim, and K.-B. Kim, "Effect of Al Distribution on Carrier Generation of Atomic Layer Deposited Al-Doped ZnO Films," J Electrochem Soc **158**, D277 (2011).

95. D. J. Lee, H. M. Kim, J. Y. Kwon, H. Choi, S. H. Kim, and K. B. Kim, "Structural and electrical properties of atomic layer deposited Al-doped ZnO films," Adv Funct Mater **21**, 448–455 (2011).

96. C. Thiandoume, V. Sallet, R. Triboulet, and O. Gorochov, "Decomposition kinetics of tertiarybutanol and diethylzinc used as precursor sources for the growth of ZnO," J Cryst Growth **311**, 1411–1415 (2009).

97. D. Fomra, R. Secondo, K. Ding, V. Avrutin, N. Izyumskaya, Ü. Özgür, and N. Kinsey, "Plasmonic Titanium Nitride via Atomic Layer Deposition : A Low-Temperature Route," J Appl Phys **127**, 1–16 (2020).

98. J. Hüpkes, B. Rech, S. Calnan, O. Kluth, U. Zastrow, H. Siekmann, and M. Wuttig, "Material study on reactively sputtered zinc oxide for thin film silicon solar cells," in *Thin Solid Films* (Elsevier, 2006), Vol. 502, pp. 286–291.

99. R. Secondo, J. Khurgin, and N. Kinsey, "Absorptive loss and band non-parabolicity as a physical origin of large nonlinearity in epsilon-near-zero materials," Opt Mater Express **10**, 1545 (2020).

100. J. A. Hillier, S. Camelio, W. Cranton, A. V Nabok, C. J. Mellor, D. C. Koutsogeorgis, and N. Kalfagiannis, "When Ellipsometry Works Best: A Case Study With Transparent Conductive Oxides," ACS Photonics **7**, (2020).

101. P. Uprety, M. M. Junda, K. Ghimire, D. Adhikari, C. R. Grice, and N. J. Podraza, "Spectroscopic ellipsometry determination of optical and electrical properties of aluminum doped zinc oxide," Appl Surf Sci **421**, 852–858 (2017).

102. P. Uprety, M. M. Junda, H. Salmon, and N. J. Podraza, "Understanding near infrared absorption in tin doped indium oxide thin films," J Phys D Appl Phys **51**, 295302 (2018).

103. S. C. Malek, A. C. Overvig, S. Shrestha, and N. Yu, "Active nonlocal metasurfaces," Nanophotonics **10**, 655–665 (2021).

104. L. Kang, R. P. Jenkins, and D. H. Werner, "Recent Progress in Active Optical Metasurfaces," Adv Opt Mater **7**, 1801813 (2019).

105. A. M. Shaltout, V. M. Shalaev, and M. L. Brongersma, "Spatiotemporal light control with active metasurfaces," Science (1979) **364**, (2019).

106. G. Kafaie Shirmanesh, R. Sokhoyan, R. A. Pala, and H. A. Atwater, "Dual-Gated Active Metasurface at 1550 nm with Wide (>300°) Phase Tunability," Nano Lett **18**, 2957–2963 (2018).

107. S. Jafar-Zanjani, M. M. Salary, D. Huynh, E. Elhamifar, and H. Mosallaei, "TCO-Based Active Dielectric Metasurfaces Design by Conditional Generative Adversarial Networks," Adv Theory Simul **4**, 2000196 (2021).

6. PUBLICATIONS

6.1. Journal

1. R. Secondo, **D. Fomra**, N. Izyumskaya, V. Avrutin, J. Hilfiker, A. Martin, U. Ozgur, and N. Kinsey, "Reliable Modeling of Ultrathin Alternative Plasmonic Materials Using Spectroscopic Ellipsometry," Optical Materials Express – Beyond Thin Films: Photonics with Ultra-thin and Atomically-thin Materials Feature Issue, vol. 9, no. 2, 2019 [Invited]
2. **D. Fomra**, R. Secondo, N. Izyumskaya, V. Avrutin, U. Ozgur, and N. Kinsey "Plasmonic Titanium Nitride via Atomic Layer Deposition: A Low Temperature Route," Journal of Applied Physics, vol. 127, no. 103101, 2020
3. **D. Fomra**, K. Ding, V. Avrutin, Ü. Özgür and N. Kinsey "Al:ZnO as a platform for near-zero-index photonics: enhancing the doping efficiency of atomic layer deposition", Opt. Mater. Express 10, 3060–3072, 2020
4. K. Ding, **D. Fomra**, A.V. Kvit, H. Morkoç, N. Kinsey, Ü. Özgür and V. Avrutin "A Platform for CMOS Compatible Plasmonics: High Plasmonic Quality Titanium Nitride Thin Films on Si (001) with an MgO Interlayer", Adv. Phot. Res., 2000210, 2021
5. **D. Fomra**, A. Mamun, K. Ding, V. Avrutin, Ü. Özgür and N. Kinsey "Plasmonic Colors in Titanium Nitride for Robust and Covert Security Features", Opt. Exp. 29, 13, 19586-19592, 2021
6. N. Izyumskaya, **D. Fomra**, K. Ding, H. Morkoç, N. Kinsey, Ü. Özgür and V. Avrutin, "High-Quality Plasmonic Materials TiN and ZnO:Al by Atomic Layer Deposition", Rap. Res. Letter, 2100227 - 15(10), 2021 [Invited]
7. R. Secondo, A. Ball, B. Diroll, **D. Fomra**, K. Ding, V. Avrutin, Ü. Özgür, H. Morkoç, D. O. Demchenko, J. B. Khurgin, and N. Kinsey, "Deterministic Modeling of Hybrid Nonlinear Effects in Epsilon-Near-Zero Thin Films," Applied Physics Letters, 031103, 2022.
8. Md. Sojib, **D. Fomra**, V. Avrutin, N. Kinsey, "Optimizing epsilon-near-zero based Plasmon Assisted Modulators Through Surface to Volume Ratio", vol. 30, issue 11, pp. 19781-19794, Optics Express, 2022
9. A. Ball, R. Secondo, B. Diroll, **D. Fomra**, V. Avrutin, Ü. Özgür, N. Kinsey, "Gallium-doped Zinc Oxide: Nonlinear Reflection and Transmission Measurements and Modeling in the ENZ Region", Journal of Physics: Photonics, submitted, 2022
10. S. Saha, C. Hong, **D. Fomra**, V. Avrutin, Ü. Özgür, J.C. Ndukaife, N. Kinsey, "Modelling an on-chip integrated emitter with trap-enhance-guide approach", Optics Express, accepted, 2022
11. **D. Fomra**, A. Ball, H. Lezec, N. Kinsey, "Ultra-fast modulation of high-Q plasmonic lattice resonances", in preparation, 2022

12. A. Ball, R. Secondo, **D. Fomra**, V. Avrutin, Ü. Özgür, N. Kinsey, "Spatio-temporal refractive index phenomenon in beam deflection", in preparation, 2022
13. A. Ball, R. Secondo, **D. Fomra**, V. Avrutin, Ü. Özgür, N. Kinsey, "Beam Deflection: Maximizing the nonlinear figure of merit in epsilon-near-zero materials through dual excitation", in preparation, 2022

6.2. Patents and Book Chapters

1. N. Kinsey, **D. Fomra**, Md. Sojib, V. Avrutin, Ü. Özgür, "Plasmon Assisted Design Philosophy for Electro-Optic Modulators", US 63/311 - 194, 2022
2. A. Ball, **D. Fomra**, J. Khurgin, and N. Kinsey, "Ch 11: Nonlinearities in Epsilon-Near-Zero Media," Advances in Nonlinear Photonics, Ed. G. C. Righini and L. Sirleto, Elsevier, in preparation, 2022

6.3. Major Conference Submissions

1. **D. Fomra**, A. Ball, H. Lezec, N. Kinsey, "All optical modulation of high-Q plasmon resonances", SPIE Optics and Photonics, 2022
2. N. Kinsey, **D. Fomra**, A. Ball, Md. Sojib, S.Saha, V.Avrutin, Ü.Özgür, "Nonlinearities when the index vanishes", SPIE Optics and Photonics, 2022
3. A. Ball, R. Secondo, **D. Fomra**, V. Avrutin, Ü. Özgür, N. Kinsey, "Dual excitation beam deflection in nonlinear epsilon-near-zero materials", SPIE Optics and Photonics, 2022
4. A. Ball, R. Secondo, **D. Fomra**, V. Avrutin, Ü Özgür, N Kinsey, "Beam Deflection characterization of nonlinear transparent conducting oxides at epsilon-near-zero", SPIE Photonics West, 2022
5. C. Hong, S. Saha, **D. Fomra**, J.C. Ndukaife, N. Kinsey, "On-chip Nano-object Trapping with Conjugate Optical and Thermophoretic Force" OSA FiO+LS, 2021
6. Md. Sojib, **D. Fomra**, V. Avrutin, N. Kinsey "Surface to Volume Ratio as a Design Principle for ENZ-based Plasmon Assisted Electro-Optic Modulators" OSA FiO+LS, 2021
7. S. Saha, C. Hong, **D. Fomra**, J.C. Ndukaife, N. Kinsey "Large Purcell Enhancement and On-Chip Emission Coupling with Hybrid Plasmonic Device" OSA FiO+LS, 2021
8. S. Saha, **D. Fomra**, J.C. Ndukaife, V. Avrutin, N. Kinsey, "Modeling an On-Chip Opto-Thermo-Mechanical Nano- Switch for Integrated Photonics Application" OSA FiO+LS, 2021
9. **D. Fomra**, K Ding, V Avrutin, Ü Özgür, N Kinsey, "Comparative study of MBE-and ALD-deposited doped zinc oxide" SPIE Photonics West, San Francisco, CA, 2021
10. N. Kinsey, R. Secondo, **D. Fomra**, A. Ball, M. A. H. Sojib, S. Saha, K. Ding, V. Avrutin, Ü. Özgür, and J. Khurgin, "Epsilon-Near-Zero Materials in Nonlinear Optics – From Theory to Applications," SPIE Optics & Photonics, San Diego CA, 2021

11. N. Kinsey, **D. Fomra**, K. Ding, M. A. H. Sojib, S. Saha, R. Secondo, A. Ball, V. Avrutin, and Ü. Özgür, "Advancing Functional Materials for Robust and Dynamic Nanophotonics" MRS Spring Meeting, Virtual Conference, 2021
12. S. Saha, **D. Fomra**, N. Kinsey, "Modeling On-Chip Nanoscale Waveguide based Trapping Device for Quantum Photonics using COMSOL Multiphysics", COMSOL Conference, 2020
13. **D. Fomra**, K. Ding, V. Avrutin, Ü. Özgür, N. Kinsey, "Al:ZnO with enhanced doping efficiency by atomic layer deposition as a platform for near-zero-index photonics" MRS Fall Meeting, Boston MA, 2020
14. K. Ding, **D. Fomra**, V. Avrutin, N. Kinsey, U. Ozgur, and H. Morkoc, "Effect of MgO buffer on the plasmonic quality of TiN films on Si (100)," MRS Fall Meeting, Boston MA, 2020
15. **D. Fomra**, V Avrutin, Ü Özgür, N Kinsey, "All oxide plasmon-assisted optical modulator", SPIE Optics and Photonics, SPIE Optics and Photonics, San Diego, CA, 2020
16. N. Kinsey, R. Secondo, **D. Fomra**, and J. Khurgin, "Illuminating Nonlinearities in Epsilon-Near-Zero Materials," SPIE Optics and Photonics, San Diego CA, 2020. [Invited]
17. **D. Fomra**, MD. Mamun, K Ding, V Avrutin, Ü Özgür, N Kinsey, "Plasmonic color using titanium nitride for robust security devices", SPIE Optics and Photonics, San Diego, CA, 2020
18. **D. Fomra**, K. Ding, V. Avrutin, Ü. Özgür, and N. Kinsey, "Atomic layer deposition of aluminum doped zinc oxide: Platform for integrated near zero index photonics," SPIE Optics & Photonics, San Diego CA, 2020.
19. N. Kinsey, R. Secondo, **D. Fomra**, "Modelling Nonlinear Optics in Epsilon-Near-Zero Oxides Through Carrier Kinetics", IEEE, International ACES, 2020
20. **D. Fomra**, K. Ding, V. Avrutin, N. Izyumskaya, N. Kinsey, Ü. Özgür, and H. Morkoç, "Low-temperature growth of ZnO-based TCOs by MBE and ALD for Plasmonics" SPIE Photonics West, San Francisco, 2020.
21. **D. Fomra**, K. Ding, V. Avrutin, Ü. Özgür, and N. Kinsey "Atomic Layer Deposition of Titanium Nitride for Robust Plasmonic Color Security Devices" Frontiers in Optics and Laser Science, Washington DC, 2019.
22. K. Ding, **D. Fomra**, V. Avrutin, N. Kinsey, U. Ozgur, and H. Morkoc, "High Plasmonic Quality Titanium Nitride Thin Films on Si (001) with MgO Buffer," Frontiers in Optics and Laser Science, Washington DC, 2019
23. **D. Fomra**, R. Secondo, K. Ding, N. Izyumskaya, V. Avrutin, Ü. Özgür, and N. Kinsey "Engineering losses in gallium-doped zinc oxide (GZO) by molecular beam epitaxy" SPIE Optics & Photonics, San Diego, 2019.
24. C. Campbell, A. Casey, **D. Fomra**, J. Drobitch, G. Triplett, "The influence of the fabrication developing time on plasmonic bowtie nanoantenna metastructures", SPIE Photonics West, 2019
25. **D. Fomra**, R Secondo, V. Avrutin, Ü. Özgür, and N. Kinsey, "Optimized Growth of Titanium Nitride Films using Plasma Enhanced Atomic Layer Deposition" Frontiers in Optics and Laser Science, Washington DC, 2018

26. **D. Fomra**, V. Avrutin, Ü. Özgür, and N. Kinsey, “Photonic to plasmonic energy transfer for low-loss hybrid plasmonic modulators”, SPIE Optics & Photonics, San Diego, 2018
27. R. Secondo, **D. Fomra**, V. Avrutin, Ü. Özgür, and N. Kinsey, “Characterization of Plasma Enhanced Atomic Layer Deposited Titanium Nitride,” SPIE Optics & Photonics, San Diego, 2018.

6.4. Vita

Dhruv Fomra was born on December 5, 1994, in Rajasthan, India. In 2017, he completed his bachelor's degree in Nanotechnology from SRM University, Chennai, India. He then went on to pursue his PhD in Electrical and Computer Engineering at Virginia Commonwealth University (VCU), with an emphasis on Nanophotonics.

During his time at VCU, Fomra interned at the National Institute of Standards and Technology for one year, from 2021 to 2022. He was highly accomplished as a graduate researcher, receiving the Best Graduate Researcher award from the ECE department three times. He was also a finalist for the College of Engineering Research Awards and received VCU's Dissertation Award.

Fomra completed his PhD in 2022 and has since become recognized as an expert in the field of Nanophotonics. His research has contributed to the development of photonic integrated circuits, which have the potential to positively impact many aspects of technology and communication.